ZnO and ZnCdO metal organic vapor phase epitaxy: epitaxy, defects and band gap engineering

By

Vishnukanthan Venkatachalapathy

Submitted

in partial fulfillment of the requirements

for the degree of

Philosophiae Doctor

Department of Physics/Centre for Materials science and Nanotechnology

Faculty of Mathematics and Natural Sciences

University of Oslo

Dedicated to my father

Abstract

Zinc oxide (ZnO) and its ternary alloys have high potential to compete with III-V nitrides for optoelectronic applications. Furthermore, oxide semiconductors receive considerable attention due to their low cost of fabrication, chemical robustness and high thermal conductance. The goal of this work was (i) to explore manufacturing route of ZnO and ZnCdO films using metal organic vapor phase epitaxy (MOVPE) in vector flow epitaxy mode and (ii) to master structural/optical properties of these films for preparing such as components in electronics, optoelectronics and solar energy conversion.

Our starting point was to study the influence of basic synthesis parameters on the structural and luminescence properties of pure ZnO films on c-axis oriented sapphire substrates. The samples were synthesized using previously unexplored for ZnO vector flow epitaxy mode of MOVPE employing systematic variations of fundamental synthesis parameters such as temperature, pressure, II/VI molar ratio, total carrier gas flow ratio, susceptor rotation rate, etc. It was concluded that the growth temperature affects the precursor pyrolysis and in these terms pre-determines the actual II/VI molar ratio available at the reaction zone. Concurrently, direct II/VI molar ratio variations by supplying different amount of precursors influences the properties too, for example, changing intrinsic defect balance in the films. Variations of other parameters like chamber pressure, total gas flow rate and susceptor rotation rate resulted in minor deviations in the growth, uniformity and properties.

Further, exploring cheaper substrates, ZnO films have also been successfully fabricated on Si(111) substrates by using AlN buffer layers. The process resulted in ZnO/AlN/Si heterostructures, where ZnO films were grown epitaxially on AlN buffers having different thicknesses and matching Si(111) with so called domain-matching epitaxy. An optimal thickness of the AlN buffer was determined, resulting in nearly in-plane strain free ZnO films. Such films exhibited excellent crystalline quality and extremely bright excitonic emissions.

Accounting that for any device realization, it is essential to control point defects in the crystal, we have specifically characterized the changes in the defect balance as a function of synthesis parameters in our films. Manipulating with the growth temperature we could achieve either Zn-lean or O-lean conditions. Positron annihilation spectroscopy and photoluminescence were employed to study point defects in such films. A range of vacancy complexes was identified from signal variations going consistently with variations in the synthesis conditions. Specifically, a synthesis window resulted in availability of zinc vacancies (V_{Zn}) was determined.

Finally, manufacturing routes of wurtzite ZnCdO alloys were explored utilizing the knowledge obtained when mastering V_{Zn}-enriched material. The alloys exhibited mixed wurtzite, zincblende and rocksalt phases for Cd contents > 7 % in parallel with decreasing excitonic luminescence. The phase separation is interpreted in terms of corresponding changes in charge distribution and reduced stacking fault energy. A narrow Cd content region ($\leq$ 2%) was attributed to the wurtzite single phase equilibrium. The band gap of ZnCdO thin was found – consistently with literature – to decrease with increasing Cd concentration. In our experiments, by changing Cd content, the band gap of ZnCdO was tuned from 3.4 eV to 2.3 eV, providing an excellent opportunity for band gap engineering in future optoelectronic applications.

Acknowledgements

"Known is a drop,

Unknown is an ocean."

- Avvaiyar

As the quote, "*Teamwork is the fuel that allows common people to produce uncommon results*", this work of mine is the outcome of such an wonderful teamwork. In particular, my supervisor, Prof. Andrej Yu. Kuznetsov, deserves my deepest thanks, without his supervision and experience, I would not be able to accomplish this task. He also had great confidence in me and supported me throughout the work. Very kind of him, in helping me to improve my skills and worked harder than me in proofreading all my research reports and thanks for all his efforts and useful discussions. I would also take immense pleasure for the great help and guidance from Dr. Augustinas Galeckas, who answered patiently to all my questions and helped a lot in measuring Photoluminescence for all my samples in huge quantity and also proofreading my reports. I also enjoyed all the discussions with Augustinas especially about the culture in India and new fancy gadgets. I am also grateful to Prof. Bengt G. Sevensson, Prof. Terje Finstad and Dr. Eduoard Monakhov for enlightening me in understanding semiconductors. Thanks to Victor and Mikael for their timely help and support in fixing the needs for the MOVPE equipment. Asst. Prof. Ola Nilsen, from chemistry department deserves big thanks for his support and introducing me to X-ray Diffraction.

Some part of the work described in this thesis is performed at Aalto University, Espoo, Finland formerly known as Helsinki University of Technology. I am grateful to Dr. F. Tuomisto, who gave me access to their equipment and for spending time in discussing my

results. In particular, I would to thank Dr. A. Zubiaga for introducing me to positron analysis and to the positron group and helped me in mounting the samples and also during the measurements. I would also like to thank other people from the positron group from Helsinki for making very pleasant and wonderful stay. Dr A. Azarov, deserves my thanks for helping me in performing RBS analysis of my samples.

Then, I'd like to thank my colleagues in MiNalab. Special thanks to Dr.Ramon, Dr. Agnieszka, Pekka, Mareike, Knut Erik, Michael for sharing office and very interesting useful discussions. The two Chinese guys, Dr. Tianchong and Dr. Junjie (now at IFE) helped me to understand MOVPE in a different perspective. Thanks to Dr. Lasse and Klaus Magnus for introducing SIMS and AFM to me and Lars Løvlie for his crazy ideas and discussions. Though I never joined for the lunch, I enjoyed the company of all the people at MiNaLab during the Christmas parties and social get together. Special thanks to Mona Moengen for making my life comfortable during the first days in Norway. Thanks to Vincent and his girlfriend Maelenn and Mareike for their wonderful company during my trip to Iceland and China.

I would like also to thank Jeyanthinath, Jan, Camilla, Dani Mickael, Vanessa, Murugan, CP Suresh and Jayakumar for their wonderful company and making my life comfortable during my stay in Oslo. It is worth to mention, two of my friends Naveneethan (now at Trondheim) and Vijayshankar (now at Bergen) from India, sharing everything with my personal life right from my bachelors till now. I would also like to thank my friends - Blossom family, Boobalan, Sivamala, and Rani from India and also my family and relatives, especially my father and younger sister for constantly supporting me during my PhD.

Last but not least, I would like to thank everyone in MiNalab, SMN and at University of Oslo for their help and contribution. I would also like to thank Norwegian Research Council for providing research funding for my work.

Contents

List of included paper

1. **ZnO growth by vector flow epitaxy**
   V. Venkatachalapathy, A. Galeckas and A. Yu. Kuznetsov
   To be submitted

2. **Engineering of nearly strain-free ZnO films on Si(111) by tuning AlN buffer thickness**
   V. Venkatachalapathy, A. Galeckas, I-H Lee and A. Yu. Kuznetsov
   Submitted to Physica B

3. **Changing vacancy balance in ZnO by tuning synthesis between zinc/oxygen lean conditions**
   V. Venkatachalapathy, A. Galeckas, A. Zubiaga, F. Tuomisto and A.Yu.Kuznetsov
   Journal of Applied Physics, **108**, 046101 (2010).

4. **Tuning light absorption by band gap engineering in ZnCdO as a function of MOVPE-synthesis conditions and annealing**
   V. Venkatachalapathy, A. Galeckas, R. Sellapan, D. Chakarov and A.Yu.Kuznetsov
   Journal of Crystal Growth, **315**, 301 (2011)

5. **Understanding phase separation in ZnCdO by a combination of structural and optical analysis**
   V. Venkatachalapathy, A. Galeckas, M. Trunk, T. Zhang, A. Azarov and A. Yu. Kuznetsov
   Accepted in Physical Review B (2011).

Related publications not included in the thesis

1. **Structural and optical properties of polar and non-polar ZnO films grown by MOVPE**

   J. J. Zhu, T. Aaltonen, V. Venkatachalapathy, A. Galeckas and A. Yu. Kuznetsov

   Journal of Crystal Growth, **310**, 5020 (2008).

2. **Deep level related photoluminescence in ZnMgO**

   M. Trunk, V. Venkatachalapathy, A. Galeckas and A. Yu. Kuznetsov

   Applied Physics Letters, **97**, 211901 (2010).

3. **MgZnO synthesis employing weak oxidants for accurate Mg incorporation control**

   T. C. Zhang, V. Venkatachalapathy, A. Azarov, M. Trunk, A. Galeckas, and A. Yu. Kuznetsov

   Submitted to Journal of Crystal Growth

Chapter 1

Introduction and motivation

1.1 Significance of epitaxial film fabrication

The last few decades have brought a true electronic revolution of enormous significance to our everyday lives. A question on the minds of those concerned with the semiconductor revolution has been at what level, and when, the progress will taper off and finally cease. Using Si in conventional structures, the ultimate limits for the processing and storage of data appear to be on the horizon [1,2]. Beyond those limits, progress seems likely only using unconventional approaches including the use of photonic devices that are fabricated mainly in compound semiconductor materials. Thus there is a demand for discovering new materials and structures often involving heteroepitaxial synthesis. Concurrently, a precise control of materials on atomic scale has been improved during the last decade, resulting in remarkable advances in the fundamental understanding of the physics and chemistry of thin films, their microstructural evolution and properties. This progress has contributed to interesting discoveries in novel wide band gap semiconductors highlighted by, for example, progress in zinc oxide (ZnO) synthesis [3] and the present thesis contributes to the topic.

In the past decades, research in optoelectronics focused on the crystal growth and conductivity control of semiconductors such as silicon carbide [4], III-V compound semiconductors [5] and II-VI metal oxides [6]. Furthermore, the external quantum efficiency of III-nitride based devices, emitting in the blue regime, was found to surpass

that of SiC emitters (41% for non-polar InGaN/GaN LEDs vs. 0.03% for SiC LEDs) [4,7]. Equally critical to the success of III-V nitrides was the achievement of stable p-type behaviour and low resistivity (2 Ω-cm) in GaN layers doped with Mg [8]. These breakthroughs made possible the fabrication of small size, high-brightness blue light-emitting devices and laser diodes [9]

In parallel with nitrides, oxide semiconductors continue to receive considerable attention due to their low cost of fabrication, chemical robustness and high thermal conductance [6]. Transparent conducting oxides such as Sn-doped In_2O_3 (ITO), Sb-doped SnO_2, F-doped SnO_2 and Al-doped ZnO are usually fabricated on transparent substrates such as glass or sapphire [10,11]. These materials are always n-type with a resistivity of 10^{-4}-10^{-5} Ω-cm and are widely used as transparent electrodes in thin film transistors, organic light-emitting diodes and solar cells. The lack of transparent p-type oxide material has always been a major obstacle to the fabrication of oxide-based p-n junctions. Similar to GaN, ZnO has a direct band gap of 3.37 eV at 300 K that can be engineered via dilute alloying with BeO [12], MgO [13] and CdO [14], while retaining the ZnO crystallographic structure. Interestingly, the more tightly bound exciton in ZnO (59 meV) compared with other compound semiconductors (30 meV for GaN) opens the possibility for ZnO-based optical devices to operate well above 300 K (26 meV). Lasing in optically pumped ZnO has already been demonstrated at 300 K in high-quality epilayers [15-17], polycrystalline films (so-called "random lasers) [18], quantum well superlattices [19] and nanowire arrays [20]. Besides its suitable properties for optical applications, the attractiveness of ZnO also lies in its breakdown strength (on the order of 10-600 kV/cm depending on the varistor geometry) [21], high saturation velocity (3 x 10^7 cm/s for a 250 kV/cm field strength) [22] and bulk electron mobility (~200 cm^2/V-s at 300 K) [23]. Furthermore, ZnO shows electron and proton radiation hardness capabilities, of potential use in high-irradiation conditions such as space-based environments [24].

1.2 Thesis motivation, objectives, and structure

ZnO and its ternary alloys have the potential to compete with III-V nitrides for optoelectronic applications. However, the fabrication of optical devices still suffers from the lack of *p*-type ZnO. The quest for stable, *p*-type ZnO is a challenging one because the electronic and optical properties of ZnO are very sensitive to low concentrations of

dopants, impurities, and to microscopic perturbations of the lattice [25]. Though epitaxial growth is known to induce point and extended defects in ZnO, there are few studies of the formation mechanisms and characterization of these defects, and of their effects on the epilayer macroscopic properties. Yet, the role of crystal defects in ZnO is a subject of considerable interest because the realization of devices will require understanding of the interactions between acceptors and crystal defects, either native or doping-induced.

A number of methods to fabricate ZnO thin films have been studied so far, among which metal organic vapor phase epitaxy (MOVPE) has extensively studied as a function of reactor type, growth conditions, substrate variations, for the attainment of high quality material. Furthermore, from a technological point of view, MOVPE has many advantages in terms of high growth rates, interface abruptness, and manufacturability of alloys consisting of combinations of three or more elements. Importantly, the growth of III-nitrides by MOVPE is well established, which also allows us to integrate GaN or AlN as buffer layers for ZnO heteroepitaxial growth.

The objectives of this thesis are: (1) to learn how to master the MOVPE-ZnO growth by providing optimal conditions for the chemical reaction to occur at the growth front of the film and not anywhere else in the reactor, or in other words avoiding pre-reactions; (2) to systematically vary the vacancy balance in ZnO by tuning synthesis between zinc/oxygen lean conditions and characterize the nature of crystal defects in order to understand the microstructural properties of the films; and (3) to engineer band gap, E_g, in wurtzite-ZnO (~ 3.34 eV) by alloying with rock salt-CdO (~ 2.3 eV).

The thesis is organized in the following manner. Chapter 2 introduces crystalline structures, native defects, and corresponding electronic levels in ZnO as well as a brief review of tuning band gap in ZnO based alloys. Chapter 3 includes an overview of basic MOVPE principles, a summary of current status of MOVPE-ZnO synthesis, and an overview of MOVPE facilities at the MiNaLab. Chapter 4 documents characterization methods employed to study properties of MOVPE-ZnO films in the present thesis. Exploration of ZnO MOVPE synthesis and mastering of nearly strain free ZnO films on Si(111) are summarized in Chapter 5. Chapter 6 highlights discoveries of changing intrinsic defect balance by tuning synthesis between zinc/oxygen lean conditions. Finally, in Chapter 7, the results obtained on band gap engineering and phase separation in ZnCdO are presented.

Chapter 2

Properties and challenges in ZnO

2.1 Crystalline structure and heteroepitaxy

2.1.1 Crystalline structure

Crystal structure of ZnO is usually the hexagonal wurtzite (w-) type, which has nearly the same tetrahedral nearest-neighbor atomic coordination as cubic zincblende (zb-) type structure. As shown in Figs.2.1 (a) and (b), the w-structure has AaBbAaBbAaBb… stacking sequence along the [0001] axis, while the zb-structure has AaBbCcAaBbCc… stacking sequence along the [111] axis, where A(a), B(b), and C(c) denote three kinds of cation (anion) position in the triangular lattice on the (0001) and (111) planes. The difference between the w- and zb-structures is only the stacking sequence, w-structure has a hexagonal unit cell with two lattice parameters *a* and c in the ratio of c/a = 8/3 = 1.633 and belongs to the space group of C^4_{6v} or $P6_3mc$. The structure is composed of two interpenetrating hexagonal close-packed (hcp) sub lattices, each of which consists of one type of atom displaced with respect to each other along the three-fold c-axis by the amount of *uc* = 3/8 = 0.375 (in an ideal w-structure) in fractional coordinates (the *u*-parameter is defined as the length of the bond parallel to the c-axis in units of *c*). In reality, the w-structure deviates from the ideal arrangement, by changing the *c/a* ratio or the *u*-value. Since the *c/a* ratio also correlates with the difference of the electro negativities of the two constituents, components with the greatest differences show largest departure from the ideal *c/a* ratio [26]. For the w-ZnO, the lattice constants mostly range

from 3.2475 to 3.2501 Å for the *a*-parameter and from 5.2042 to 5.2075 Å for the *c*-parameter. The *c/a* ratio and *u*-parameter vary in a slightly wider range, from 1.593 to 1.6035 and 0.3817 to 0.3856, respectively [27]. For the zb-polytype of ZnO, the calculated lattice constants based on modern ab-initio technique are predicted to be 4.60 [28] and 4.619 Å [29]

In the w-structure, however, there are pairs of cation and anion atoms (connected by dashed lines along the [0001] direction in Fig.2.1(b)) are attracted to each other by electrostatic force. It is believed that these electrostatic interactions make w-structure in ZnO, AlN, GaN, and InN more stable as compared to zb-structure because of high ionicity of these compounds. In the w-structure, the length of the bonds, illustrated by

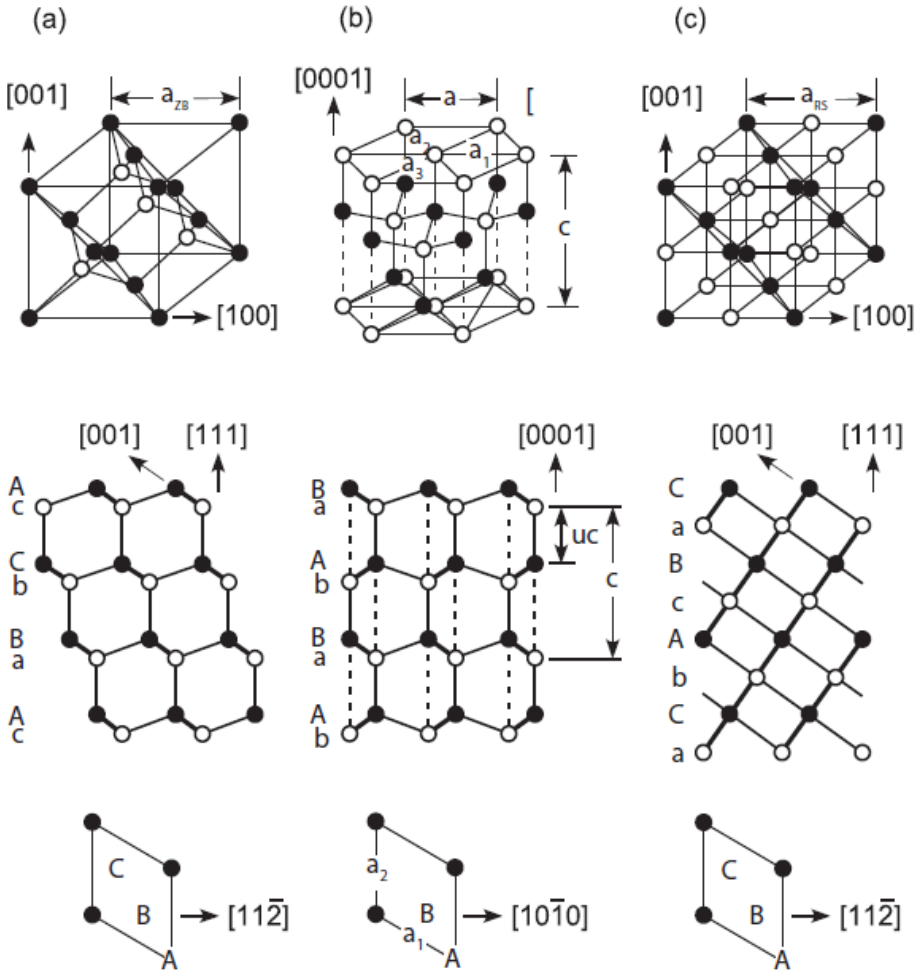

Fig. 2.1 Atomic arrangements in (a) zincblende, (b) wurtzite, and (c) rock salt structures. *Closed/open circles* and *thick solid lines* represent cation/anion and bond projections, respectively. After Ref. 26

dashed lines in Fig.2.1(b) tends to be shorter than that in the ideal w-structure. In fact, *c/a* is smaller than ideal 1.633 in most of the w-type materials [30]. Furthermore, it is easier to shorten the interlayer distances between A–b and B–a than to shorten those between A–a and B–b because the former can be done mostly with angle deformation of the bond pairs. As a result, *u* is usually larger than ideal value of 0.375. These structural deformations induce spontaneous polarizations; relative displacement of cation to [000-1] and anion to [0001] from the ideal structure.

2.1.2 Heteroepitaxy of ZnO

The interface formed between a layer and a substrate is either coherent, semi-coherent or incoherent [31]. When the layer matches the substrate perfectly, the interface is coherent and the lattices pattern continues across the interface. This requires the same atomic configuration and readily happens in homoepitaxy. A semi-coherent interface is characterized by a network of misfit dislocations which form periodically along the interface to accommodate the lattice misfit strain. Finally, when the lattice mismatch is significant (> 5%), the interface becomes incoherent usually resulting in low quality of the films. In order to minimize interfacial/in-plane strain, the interface may be modified by buffers enhancing the match between the substrate and the film.

Due to chemical robustness, optical transparency and the fact that large area Al_2O_3 wafers can be fabricated at relatively low cost, the most widely used substrate for ZnO epitaxy is (0001) Al_2O_3. Nevertheless, Al_2O_3 exhibits rhombohedral structure while ZnO as discussed in Sec.2.1.1 adopts hexagonal symmetry. As a result, a lattice mismatch of ~18.4% (in addition to the thermal mismatch of ~ -13%) exists for atomic arrangements in (0001) Al_2O_3 and (0001) ZnO planes. As an alternative, nearly lattice-matched substrates may be used for improving ZnO heteroepitaxy, e.g., InGaN containing 22% of indium [32] or $ScAlMgO_4$. $ScAlMgO_4$ is an hexagonal oxide compound that can be viewed as a superlattice formed by alternating stacks along the c-direction of (111) $(ScO)_y$ rocksalt layers and (0001) $(Mg,Al)O_x$ wurtzite layers. It has the following lattice parameters: a =3.246 Å, c =25.195 Å matching ZnO in its basal plane. ZnO grown on $ScAlMgO_4$ shows superior optical and electronic transport properties [33]. While the drawback with choosing this substrate may be its cost when up-scaling the technology. As an alternative, it is worth noting that ZnO lattice mismatch with GaN and AlN are as low as ~1.8% and 4.3%, respectively. Thus, these nitrides can be used in the form of buffers

when depositing ZnO on conventional substrates (e.g. Al_2O_3, Si(111), etc). Exploration of the ZnO synthesis was in the scope of this thesis (see Chapter 5).

2.2 Native defects and corresponding electronic levels

2.2.1 Native defects and defect related luminescence in ZnO

Controlling the conductivity in ZnO has remained a major issue. Even relatively small concentrations of native point defects and impurities (down to 10^{-14} cm^{-3} or 0.01 ppm) can significantly affect the electrical and optical properties of semiconductors [34]. Therefore, understanding the role of native point defects (i.e. vacancies, interstitials, and antisites) and the incorporation of impurities are issues when mastering the conductivity in ZnO. Regardless of growth technique, bulk or thin film growth, ZnO exhibits in most cases n-type conductivity having carrier concentrations in the 10^{15} – 10^{17} cm^{-3} range. For a long time, it has been accepted that the unintentional n-type conductivity in ZnO is caused by the presence of oxygen vacancies (V_O) and/or zinc interstitials (Zn_i) [35-38]. However, recent density functional calculations correlated with optically detected electron paramagnetic resonance measurements on high quality ZnO crystals have demonstrated that this hypothesis may not be correct [39-41]. For example, it has been shown that V_O's are actually deep donors and can not contribute to n-type conductivity alone [41]. Similarly, it was found that Zn_i's and Zn antisites (Zn_O) may neither be the prime causes of the observed n-type conductivity in as-grown ZnO crystals [40]. The present consensus on the reasons of n-type ZnO behavior is in combination of all possible intrinsic donors with operation of extrinsic contaminations such as H [42], Li [27], etc. unintentionally introduced during synthesis.

For example, by means of density-functional calculations it has been shown that interstitial H (H_i) forms a strong bond with O in ZnO and acts as a shallow donor [42]. Importantly, H_i has been identified and characterized in ZnO [43,44]. However, H_i is highly mobile [45] and can readily diffuse out of the samples, making it difficult to explain the stability of the n-type conductivity at relatively high temperatures. Furthermore, notably defect formation energies depends on the growth conditions, so that a certain type of defects, e.g., zinc vacancies (V_{Zn}) in oxygen-rich conditions may be predominantly generated. Assuming defects are introduced in high concentrations they

may form complexes introducing new shallow/deep levels in the band gap influencing electrical and optical properties of ZnO.

Thus monitoring optical emissions using, e.g. a method of photoluminescence (PL) may be a powerful tool to study point defects in semiconductors in general and ZnO in particular. Indeed, a number of point defects identification scenarios have been suggested in ZnO analyzing PL data. Often, however, contradicting to each other. Following a convention to divide PL spectrum into near band edge (NBE) and deep level band (DLB) emission, typical DLB signatures are depicted in Fig.2.2 [46] and microscopic identification of DLB signatures was in the scope of the thesis too (see Chapter 6).

To start with there may be multiple reasons to explain the peaks in Fig.2.2 because different transitions can lead to similar emissions. Transitions involving V_{Zn}'s - one of the most probable native defects in ZnO - have been suggested by several authors to be the only course for all emissions [47,48]. In parallel, transitions mediated by V_O's have also been suggested to occur in ZnO [49,50]. In addition, Zn_i, oxygen interstitials (O_i), and other extrinsic deep levels including Cu have all been proposed as sources of the green luminescence emission in ZnO [51]. More recently, the green emission band has been explained as originating from more than one deep level defect. For example, V_O and V_{Zn}, which have different optical characteristics, were both found to contribute to the broad green luminescence band [52,53]. Yellow and orange emissions has also been attributed

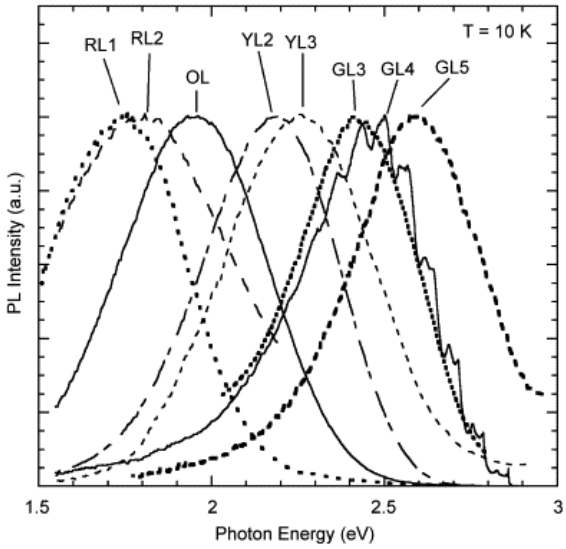

Fig.2.2 Selected PL bands observed at 10 K in commercially available bulk ZnO grown by different techniques. Intensity is normalized at band maxima. After Ref.46

to native deep level defects in ZnO, namely to O_i's [48,54,55]. The orange-red emission was recently attributed to transitions associated with V_{Zn} complexes [56], and the red emission was proposed to be due to transitions associated with Zn_i [57]. Figure 2.3 is schematics diagram illustrating microscopic identification of native defect energy levels (in respect to the conduction band edge E_C) in ZnO reported by different groups. As a reference, the position of the extrinsic hydrogen energy level is also depicted, accounting for its role in the n-type conductivity of ZnO.

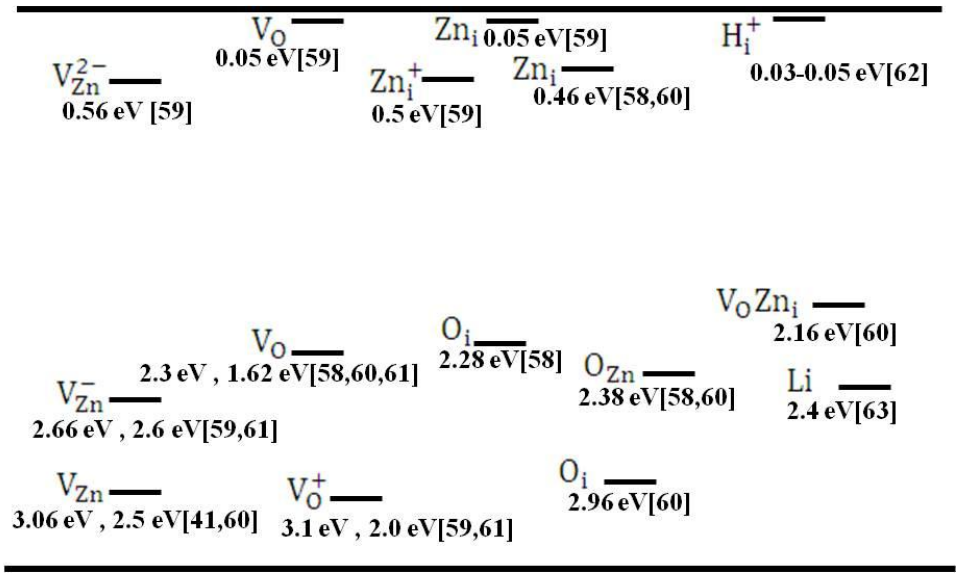

Fig.2.3 Microscopic identification of native defect energy levels in ZnO reported in the literature. The + and – symbols represent charged states of the levels. After Ref. 53

2.2.2 Crystal defects in epitaxial w-ZnO

As introduced in Chapter 1, ZnO epitaxial films grown on (0001) sapphire substrates are expected to contain a high density of threading dislocations due to the lattice mismatch. The Burgers vectors of the dislocations in hexagonal close-packed semiconductors can be deduced using an approach similar to the Thompson tetrahedron used in face-centered cubic semiconductors, as shown in Fig. 2.4 [64]. When the Burgers vector is not a translation of the lattice, the dislocation is referred to as partial. Assuming the line of the dislocation is parallel to the growth direction (threading dislocation), the examination of the bi-pyramid leads to the following dislocation types in ZnO films grown on sapphire [65]:

- edge dislocations with a Burgers vector equal in magnitude to any edge of the Thompson tetrahedron's basal plane: $\overrightarrow{b_e}$ = 1/3 <11-20> (6 possibilities, e.g. $\overrightarrow{AC}$ in Fig.2.4).

- screw-type dislocations with a Burgers vector equal in magnitude to the *c*-axis: $\overrightarrow{b_s}$ = <0001> (2 possibilities, e.g. $\overrightarrow{TS}$ in Fig.2.4).

- mixed-type dislocations with a Burgers vector that is a combination of the above two: $\overrightarrow{b_m}$ = $\overrightarrow{b_e}$ + $\overrightarrow{b_s}$ (12 possibilities, e.g. $\overrightarrow{AD}$ in Fig.2.4).

- partial basal dislocations with a Burgers vector $\overrightarrow{b_{sp}}$ = 1/3 <01-10> (6 possibilities, e.g. $\overrightarrow{A\sigma}$ in Fig.2.4). These dislocations are known as Shockley partial dislocations.

- partial dislocations with a Burgers vector equal in magnitude to one-half of the *c*-axis: $\overrightarrow{b_{fp}}$ = 1/2 <0001> (4 possibilities, e.g. $\overrightarrow{\sigma S}$ in Fig.2.4). These dislocations are known as Frank partial dislocations.

- partial dislocations with a Burgers vector that is a combination of the above two: $\overrightarrow{b_{fsp}}$ = 1/6 <02-23> (24 possibilities, e.g. $\overrightarrow{AS}$ in Fig.2.4).

In addition to dislocations, at least four types of stacking faults have been predicted in w-

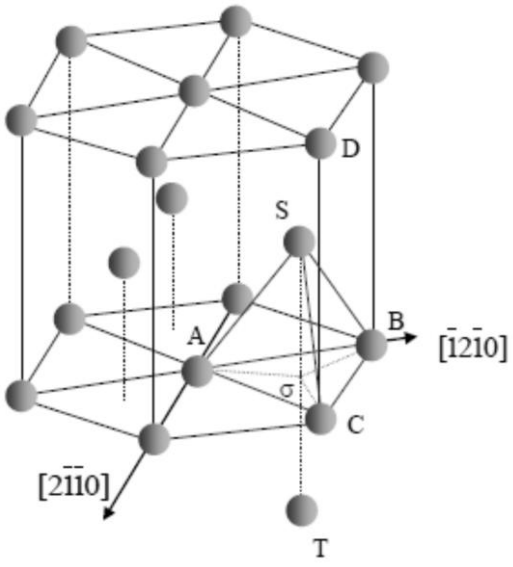

Fig.2.4 Wurtzite structure and application of the Thompson tetrahedron to the hexagonal close-packed lattice of ZnO (note, only Zn toms are depicted). After Ref. 64

GaN and ZnO [66]. Some faults are formed by the removal of a basal layer followed by slip along 1/3 <10-10>, resulting in the aAbB*aAbBcC*bBcCbB sequence. Another type of fault produces a slip of 1/3 <10-10>, resulting in the aAbB*aAbBcCaA*cCaA sequence. The third type of faults corresponds to an aA or bB layer occupying the wrong position and has been proposed by Stampl *et al*.[67] The fourth type of fault proceeds by the insertion of a basal layer, which results in the aAbB*aAbBcC*aAbBaAbB sequence. For details on the atomic arrangements of the faults, the reader is invited to consult Ref. 66. Note that these faults differ by the amount of cubic bonds (*aAbBcC* stacking as in the zincblende structure) they introduce. The first three faults are referred to as intrinsic while the latter type of fault is referred to as extrinsic.

2.3 Alloying with other oxides for tuning band gap

In order to realize modern devices, modulation of the band gap is required which has been demonstrated by the development of $Mg_xZn_{1-x}O$ [14,19,67] and $Be_zZn_{1-z}O$ [12] alloys for the larger band gap material and $Cd_yZn_{1-y}O$ alloy for the smaller band gap material [19,68-70], allowing band gap tuning in a wide range. The energy gap $E_g(x)$ of a ternary semiconductor $A_xZn_{1-x}O$ (where A = Mg, Be or Cd) is determined by the following empirical equation [71]:

$$E_g(x) = (1-x)E_{ZnO} + xE_{AO} - bx(1-x) \qquad (2.1)$$

where b is the bowing parameter and E_{AO} and E_{ZnO} are the band gap energies of compounds AO (MgO, CdO, BeO) and ZnO, respectively. The bowing parameter depends on the difference in electronegativities of the end binaries - ZnO and AO. One should exercise caution in using Eq. (2.1) for large mole fractions of Mg, Cd, and Be, because Mg-containing ZnO changes to cubic beyond 40%, and the bowing parameters are not well established for the ternaries. Figure 2.5 plots the band gap as a function of the in-plane lattice constant for all the three ternaries mentioned above, namely $Mg_xZn_{1-x}O$, $Cd_yZn_{1-y}O$ and $Be_zZn_{1-z}O$.

$Mg_xZn_{1-x}O$ alloy has been considered as a suitable material for the barrier layers in ZnO/(Mg,Zn)O superlattice structures [19] because alloying ZnO with MgO (E_g ~ 7.7 eV) enables widening of band gap of ZnO with very little change in the lattice constant. According to the phase diagram of the ZnO–MgO binary system, the thermodynamic solid solubility of MgO in ZnO is less than 4 mol% [72]. In addition, ZnO has a wurtzite structure (a = 3.24 Å and c = 5.20 Å), while MgO has a cubic structure (a = 4.24 Å). $Mg_xZn_{1-x}O$ with $X \leq 0.4$ remains wurtzite, while that with $X \geq 0.6$ becomes cubic. In the intermediate region, the quality of the films is not as good due to phase separation and availability of both phases.

Substitution of Zn by Be increases the band gap keeping $Be_zZn_{1-z}O$ in wurtzite form throughout the entire compositional range as the equilibrium state of BeO is wurtzite too as suggested by Ryu et al. [12,73] investigated the case for $Z \leq 0.6$.

For narrowing the band gaps, which are desirable for wavelength tunability and attaining the range corresponding to the visible spectrum, $Cd_yZn_{1-y}O$ alloy would be a good candidate because of a smaller direct band gap of CdO (2.3 eV) [68]. A decrease in the

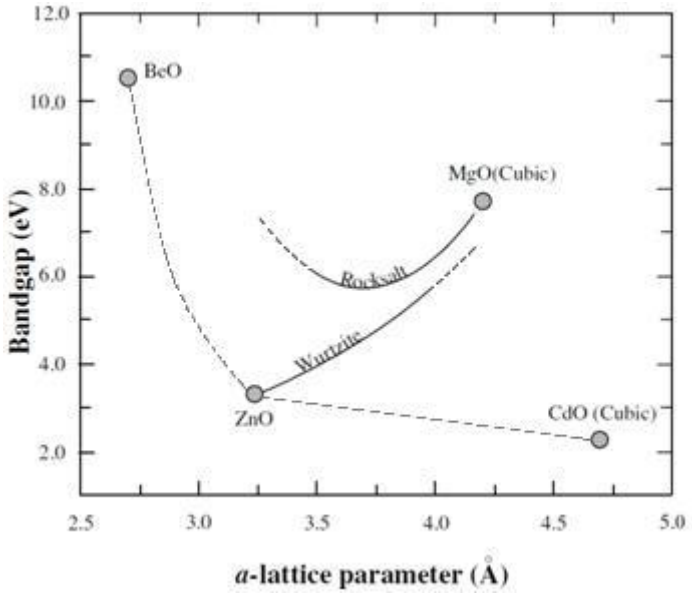

Fig.2.5 Band gap as a function of in-plane lattice constant for, $Mg_xZn_{1-x}O$, $Cd_yZn_{1-y}O$ and $Be_zZn_{1-z}O$. Note that the end binaries MgO and CdO are cubic in their equilibrium state. The band gaps variation for cubic and wurtzite modifications of $Mg_xZn_{1-x}O$ are represented by continuous lines. Understanding of band gap variations in $Be_zZn_{1-z}O$ and $Cd_yZn_{1-y}O$ is immature (illustrated by dashed lines). After Ref. 26

band gap down to 2.99 eV could be achieved by incorporating Cd^{2+} with y = 0.07 [27]. There has not been as much progress with Cd doped ZnO. We should mention that CdO is also cubic and large concentrations of Cd in ZnO lattice would cause a behavior similar to that with phase separation in MgZnO creating a dilemma of how much Cd may be introduced into ZnO before its wurtzite structure is affected. Note, only limited range of solubility may be expected from a substitution of smaller Zn atoms (0.74 Å) by larger Cd atoms (0.97 Å) [74] on equivalent crystallographic positions in the wurtzite lattice.

As compared to ZnO, there is significantly less information on ZnCdO available in literature still reporting optimistic values of Cd solubility in wurtzite structure ZnO [75-77]. For example, Ishihara et.al. reported the growth of ZnCdO films having Cd content as high as 69 % [78] . These films were deposited epitaxially on sapphire substrates and claimed to be of high crystalline quality having the band gap as low as 1.8 eV. In this case, the band gap offset of 1.5 eV can be provided for the ZnO-based heterostructure devices. Besides being used as a material for ZnO-based heterojunctions, ZnCdO thin films themselves are also considered to be the promising candidates for the short wavelength light emitting devices (LED) with adjustable band gaps that enable the devices to be operated at different wavelengths. The PL peak position was found to be red-shifted as the band gap of the film decreases [78]. The $ZnO/Zn_{0.95}Cd_{0.05}O$ superlattice structures had been reported with the band-gap offset of 0.47 $\pm$ 0.03 eV. The information on the hetero-junction band offsets of ZnO/ZnCdO can be found in Ref. 79. In this case, X-ray photoelectron spectroscopy was used and the offsets were ΔE_V = 0.17 $\pm$ 0.03 eV and ΔE_C = 0.30 eV for a band gap of ~ 2.9 eV. The heterostructures were grown epitaxially by applying molecular beam epitaxy (MBE) process on sapphire (0001) substrates with 2 μm thick GaN buffer layer in between. The thickness of the well (ZnCdO layer) varied from 1 nm to 100 nm with the constant barrier (ZnO layer) thickness of 100 nm. It is in the scope of the present work to reach better understanding of the phase equilibrium in ZnCdO (see Chapter 7).

Chapter 3

Metal organic vapor phase epitaxy

Metal-Organic vapor phase epitaxy (MOVPE) is probably the most versatile and powerful technique for thin film growth. Its potentials have been proven by producing high quality epitaxial layers with excellent surface morphology and a precise control over layer thickness and uniformity. MOVPE has been applied to the epitaxial crystal growth technology for an impressive array of commercial devices: lasers, light emitting diodes, photocathodes, heterostructure bipolar transistors, thin film transistors, transparent conducting oxides, photodetectors, and solar cells [80-82]

3.1 Basic principles and chemistry of relevant precursors

Basic chemical reaction types in MOVPE technology include pyrolysis (thermal decomposition), oxidation, reduction, hydrolysis and carbide formation, synthesis reactions, disproportionation, and chemical transport. A sequence of several reaction types may be involved in more complex situations to create particular products. Major parameters are temperature, pressure, mole fractions, gas flow rates, and reactor geometry which all together determine the deposition rate and the properties of the film deposited. A schematic of fundamental MOVPE steps is shown in Fig.3.1 [83-85] including:

[a] Gas phase diffusion - convective and diffusive transport of reactant gases into the reaction chamber;

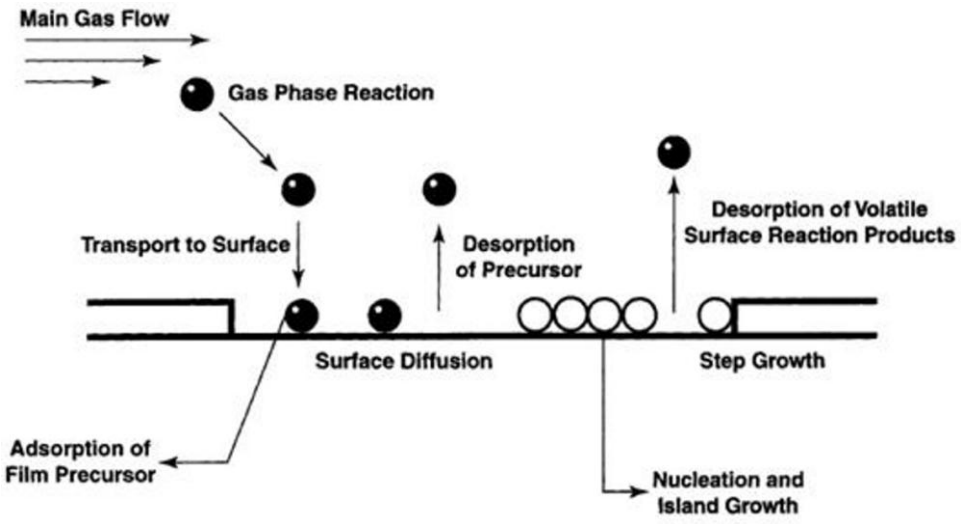

Fig.3.1 Schematic to show the transport and reaction processes underlying MOVPE. After Refs.83-85

[b] Gas phase reaction - typical chemical gas-phase reactions which generate the constituent species for deposition and by-products;

[c] Transport and absorption on surface - transport of these reactants to the surface and (chemical or physical) absorption on the surface;

[d] Surface diffusion - diffusion of these species on the surface;

[e] Incorporation at kink - incorporation of these species at kinks;

[f] Desorption - desorption or evaporation of volatile species from the surface;

[g] Nucleation and step growth for film formation - the phase change including vapor-phase condensation, solidification, or solid-state phase transformation from gases, melts, or solid matrices leading to film formation;

[h] Gas exhaustion - transport of the rest by-products during reactions to gas exhaust outlet.

Sub-sections below introduce pyrolysis, thermodynamics, precursor transport, and growth regimes considering these to be fundamentals of MOVPE.

3.1.1. Pyrolysis

In MOVPE processes, it is important to consider basic chemical reactions in the reaction chamber. The most common chemical reaction is pyrolysis which is related to thermal decomposition of gaseous species such as volatile metal-organic radicals and alcohols/oxygen source for semiconductor oxide material growth. General pyrolysis equations for binary and ternary oxide synthesis are

$$R_nA + R\text{-}OH_n \rightarrow AO + nRH \quad (3.1)$$

$$xR_nA + (1\text{-}x)R_nAB + R\text{-}OH_n \rightarrow A_xB_{1\text{-}x}D + nRH \quad (3.2)$$

where OH is hydroxyl and R is an organic radical such as a methyl $[(CH_3)_n]$ or ethyl $[(C_2H_5)_n]$-radical. A, B, and D are the constituent species for the deposited solid, and they come (in the case of present thesis) from diethylzinc (DEZn), dimethyl cadmium (DMCd), bis-cyclopentadienylmagnesium (Cp_2Mg) and trimethylaluminium (TMAl) - all commonly used in MOVPE. These metal organic species are transported to the reaction chamber with carrier gases, e.g., hydrogen or nitrogen [86]. For instance, the pyrolysis of ZnO is given by [87]

$$(C_2H_5)_2Zn + 2H_2O \rightarrow ZnO + H_2O + 2C_2H_6 \quad (3.3)$$

3.1.2 Thermodynamics

Thermodynamics is a main driving force to contribute desired deposition materials from the precursor pyrolysis process for epitaxial growth, where precursors are unstable at growth temperatures. The basic consideration of thermodynamics is to define the relationship between the compositions of the various phases in an equilibrium state where Gibbs free energy (G) per mole is a minimum at constant temperature and pressure. In thermodynamics, the Gibbs free energy is the energy portion of a thermodynamic system [88]. Although the MOVPE process is a non-equilibrium process, still thermodynamic calculations give a preliminary idea of the solid composition of a multi-component system and its growth rate. The Gibbs free energy, G, is defined as

$$G = H - TS \quad (3.4)$$

where S is the entropy of the system and H is the enthalpy, as H = E + PV where E is the internal energy, P is the pressure, and V is the volume.

The reaction of the synthesis of one mole of metal oxide MeO is $Me + ½O_2 \rightarrow MeO$.

Free energy change, ΔG, for this reaction:

$$\Delta G = G_{MeO} - (G_{Me} + ½G_{O_2})$$

$$= H_{MeO} - (H_{Me} + ½H_{O_2}) - T\,[S_{MeO} - (S_{Me} + ½S_{O_2})\,]$$

$$= \Delta H - T\Delta S \qquad (3.5)$$

In equilibrium ΔG = 0. If ΔG < 0, oxide is stable. In addition, these equations give the general basis for the phase diagram [89]. When the system is not at equilibrium, the thermodynamic driving force will try to restore the equilibrium and it specifies the maximum growth rate. Too large a driving force will cause rough growth surfaces and smaller driving force will lead to slow growth.

3.1.3 Precursor Transport

Ordinarily, in the MOVPE system, the growth rate is considerably slower than that calculated from thermodynamics. Kinetics, both surface reactions and precursor transport through the gas phase, are not fast enough to allow equilibrium to be established throughout the system at all times. Growth rate also depends on precursor transport which affects the thickness uniformity of deposited film. This precursor transport is mainly divided into two terms, diffusion and hydrodynamics. Diffusion is the motion of individual atomic or molecular species, while hydrodynamic flow is the motion of a group of gases as a whole, such as viscous flow and convection [90].

The growth rate is proportional to the flux of atoms being transported, usually by diffusion, through the gas phase to the interface, which is identical to the flux of atoms crossing the interface into the solid. Diffusion is mass transport from a higher chemical potential to a lower chemical potential happening in all matters. In gases, the process is usually quantified by diffusivity (D) which is affected by pressure and temperature as given by

$$D = D_0 \times P_0 / P \times (T / T_0)^{1.8} \qquad (3.6)$$

where D_0 is the value of D at T_0 = 273 K and P_0 = 1 atm.. Therefore, diffusion can be enhanced by decreasing pressure or increasing temperature in the reaction chamber [91].

Further, typical movement of reactant gases is acquainted with streamline-like flow. But this flow could be disturbed, referred as turbulent flow, when the flow moves against the boundary of deposition area. Thus, controlling of the turbulent flow is important to achieve a good thickness uniformity of deposited film. The viscous flow is described by the coefficient of viscosity η which varies with temperature, $T^{0.5}$, but is independent of pressure. Furthermore, convection is heat transfer in liquids and gases. This is a term used to characterize the combined effects of conduction and fluid flow. In convection, enthalpy transfer occurs by the movement of hot or cold portions of the fluid as well as heat transfer by conduction. The activity of the precursors depends on many other parameters related to the reactant movement to/on the surface. Such processes include adsorption of reactants, surface diffusion, and desorption of gas products [92].

3.1.4 Growth regimes

The practical process conditions in MOVPE growth are mostly preformed under excess partial pressures for group VI species (e.g. oxygen in ZnO), which improves the pyrolysis efficiencies and compensates for the much greater volatility of the group VI atoms in the desired solid films. Thus, in this case, the MOVPE ZnO growth rate mainly depends on the group II alkyl constituents. However, Fig.3.2 shows three discrete growth regimes which are composed of surface kinetics, mass transport, and thermodynamics considering DEZn and t-BuOH as precursors for ZnO growth as a function of growth temperature maintaining the VI/II ratio constant (VI/II = 5) [93]. The first regime (A), at relatively low temperatures (292 – 366 ^{o}C), is a region of surface kinetics limited growth and is controlled by the kinetics of surface reaction of DEZn and *t*-BuOH. The alkyl pyrolysis efficiency usually is a steep function of temperature (see Chapter.5) so that the "kinetic" regime operates in a narrow temperature range.

Once a full pyrolysis efficiency is reached, generally for all temperatures greater than ~ 360 ^{o}C in Fig.3.2, the mass transport limits the growth - region (B) at 366 ^{o}C $\leq$ T $\leq$ 416 ^{o}C. Notably, in region B, the growth rate does not depend on the growth temperature but is controlled by the amounts of DEZn and *t*-BuOH, called "diffusion" regime.. The gas phase diffusion coefficient of the alkyls is only weakly dependent on temperature but is

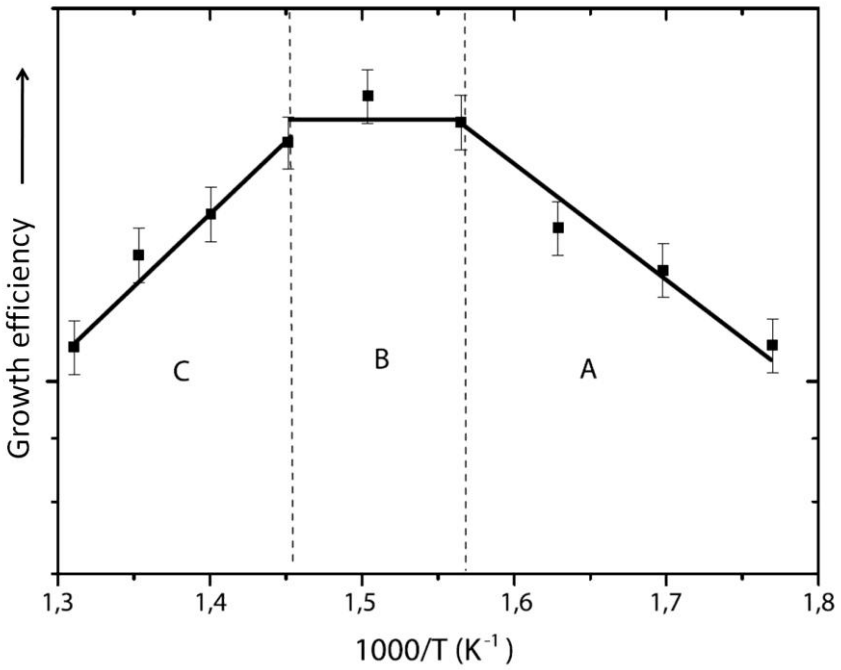

Fig.3.2 Typical growth regimes for ZnO synthesis using DEZn and t-BuOH precursors. After Ref. 93.

moderated by the boundary layers which are generated by the hydrodynamics through the reactor chamber [85].

The third region (C) occurring at T > 416 ^{o}C is characterized with a decreasing growth rate due to non-adsorption and/or desorption effects of precursors. At this end, the gas temperature away from the substrates becomes high enough for pyrolysis to occur resulting in material deposition in form of particles. Therefore, spontaneous gas phase nucleation, deposition on the reactor wall, and higher rate desorption of the reactant species disturb the desired deposition and reduce growth rate, as shown in Fig. 3.2 [85,93].

3.2 State of the art in ZnO MOVPE

Two distinct periods can be clearly distinguished in MOVPE of ZnO depending on the applications aimed at. During the initial period, lasted until late 90's, the films were mainly dedicated to such applications as solar cell transparent electrodes, piezoelectric devices or SAW filters [31]. Starting from late 90's, active photonic components were

flagged as the main application. During the first period, the 'epitaxial' quality of the films was not as essential as in the second period lasting until now. In its turn, so called pre-reaction between the Zn metal organic compounds and the oxidants, leading to unwanted deposits upstream from the susceptor, has been the main problem needing to be solved to achieve successful MOVPE growth of ZnO. To solve this key issue, less-reactive Zn metal organic compounds have been used, mainly during the first period, in combination with various oxidants, but also some adducts. Thus, different growth modes such as low pressure MOVPE and photo-enhanced or laser-induced MOVPE were investigated to increase the growth rate often severely lowered when using less-reactive precursors. As an alternative, separate inlets to inject the metal organic compound and the oxidant have then been suggested to minimize the problem of pre-reaction [94]. Overall, various carrier gases, different geometries, horizontal or vertical reactors, high speed rotation reactors have been tested for ZnO MOVPE.

ZnO MOVPE typically involves the use of metal alkyls, usually dimethyl zinc [$(CH_3)_2Zn$] (DMZn) or diethyl zinc [$(C_2H_5)_2Zn$] (DEZn) in combination with a separate source of oxygen. In earlier investigations, O_2 or H_2O were used as oxygen precursors [95-97]. However, DEZn and DMZn are highly reactive with oxygen and water vapor so that significant amount of pre-reaction in the gas phase occurs, resulting in the formation of "white powder", which degrades the film quality. Nevertheless, great progress has been made in ZnO growth by MOVPE recently. The improvement of the material quality was backed-up by improved reactor design [98] and/or the use of less-reactive precursors, allowing to minimize parasitic pre-reactions in the gas phase. Stable metal organic source of zinc acetylacetonate in combination with oxygen was successfully used for the growth of high-quality ZnO films on *r*-plane [99] as well as on *c*- and *a*-plane [100] sapphire substrates by atmospheric pressure MOVPE.

For the group-VI precursor, a variety of oxygen compounds were employed: isopropanol (*i*-PrOH) [101,102], tertiary-butanol (*t*-BuOH) [103,104], acetone [95], N_2O [95,105] and NO_2 [100]. High-quality ZnO layers have been prepared on GaN/sapphire [101] and *c*-plane sapphire [102] substrates by using DEZn and *i*-PrOH. FWHMs values of the ω-scans were 100 and 270 arcsec, respectively, depending on the substrate, and the 5K PL spectra showed strong NBE emission with line widths of 5–12 meV with phonon replicas [101]. For the films grown on *c*-plane sapphire under optimized conditions, PL was dominated by strong NBE lines with FWHM below 4 meV, and the excitonic signals

were clearly visible in reflectivity measurements [102]. Hall effect measurements indicated an n-type background doping in the 10^{17} cm^{-3} range with carrier mobilities of more than 100 $cm^2V^{-1}s^{-1}$.

Kirchner *et al* [104] have reported direct comparison of MOVPE growth of ZnO layers on *c*-plane sapphire using *i*-PrOH and *t*-BuOH as oxygen precursors and DEZn as a zinc source. It has been demonstrated that the two oxygen precursors show similar pressure dependence of the ZnO growth rate (see Fig.3.3) but large differences in temperature dependent growth rates (see Fig.3.4). The growth rate was found to be almost constant over a wide temperature range from 380 to 510 ^oC in the case of *t*-BuOH, whereas for *i*-PrOH the maximum growth rate was achieved at 380 ^oC. The optical quality of the ZnO layers grown with *t*-BuOH was superior to those grown with *i*-PrOH. For ZnO grown under optimized conditions using *t*-BuOH, strong NBE emission lines with half-widths of 1.1 meV dominated the PL spectra. High-quality homoepitaxial ZnO layers were grown on bulk ZnO substrates by using N_2O and DEZn [105]. Two conditions, proper thermal treatment of the substrate prior to the growth to obtain a flat surface and high flow rate ratios of source materials, were found to be important to obtain high-quality layers. Surface roughness below 1 nm as well as strong free exciton emission at 15Kwas reported for the films grown under optimal conditions.

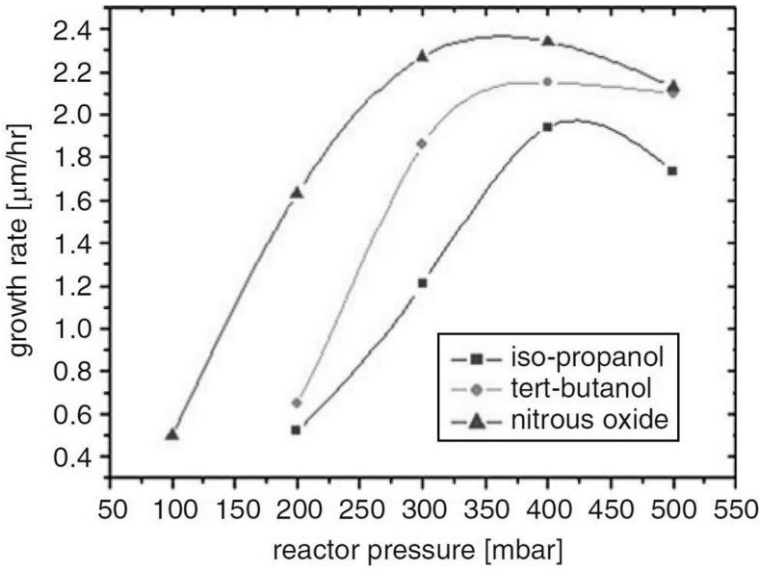

Fig.3.3 Growth rate during the ZnO MOVPE as a function of reactor pressure. After Refs.104 and 105

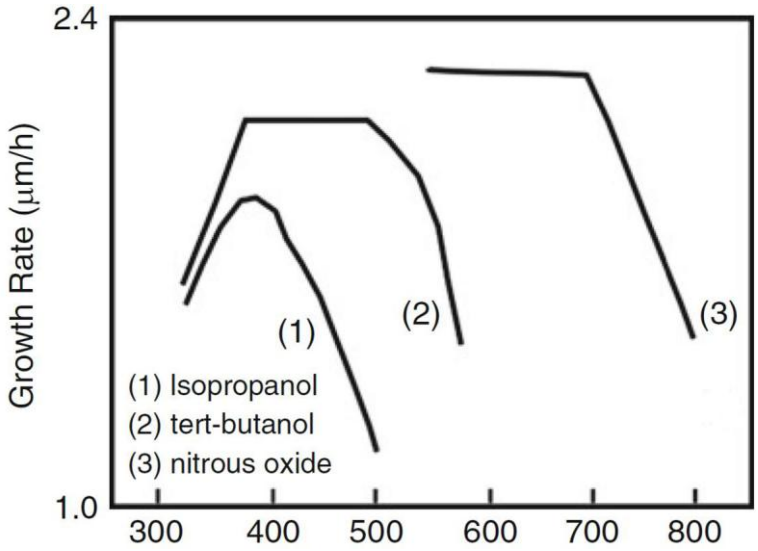

Fig.3.4 Growth rate during ZnO MOVPE as a function of growth temperature. Characteristic growth regimes as introduced in Fig.3.2 can be readily distinguished. After Refs.104 and 105

A strong effect of the surface polarity was revealed for homoepitaxial growth of ZnO films on O- and Zn-terminated ZnO (0001) substrates [106]. The films, grown on O-terminated ZnO surfaces, were initially dense. However, they changed to a textured polycrystalline microstructure after approximately 100 nm and exhibited a surface roughness of 7.3 nm. By contrast, the films grown on the Zn-terminated surface under the same conditions were fully dense, without texture, and appeared to be monocrystalline with a significantly improved surface roughness of 3.4 nm.

3.3 MOVPE system at the MiNaLab in the context of other tools

In the present thesis, ZnO MOVPE was made by introducing group II precursors and t-BuOH with carrier gases into the reaction zone at appropriate temperatures/pressures (see Figs.3.3 and 3.4) using the delivery system in Fig.3.5. In general, a typical MOVPE system consists of four major parts; gas delivery system, reactor chamber, heating/cooling system, and exhaust system. The tool used in the present thesis was operating in so called "vector flow epitaxy" mode.

3.3.1 Source pick-up and gas mixing system

The gas delivery system includes all of the valves, MFCs, regulators, and equipment for transporting sources to the reactor chamber. Thus, it is important to control the gas flows, mixtures, and distribution into the chamber as well as to be clean and leak tight.

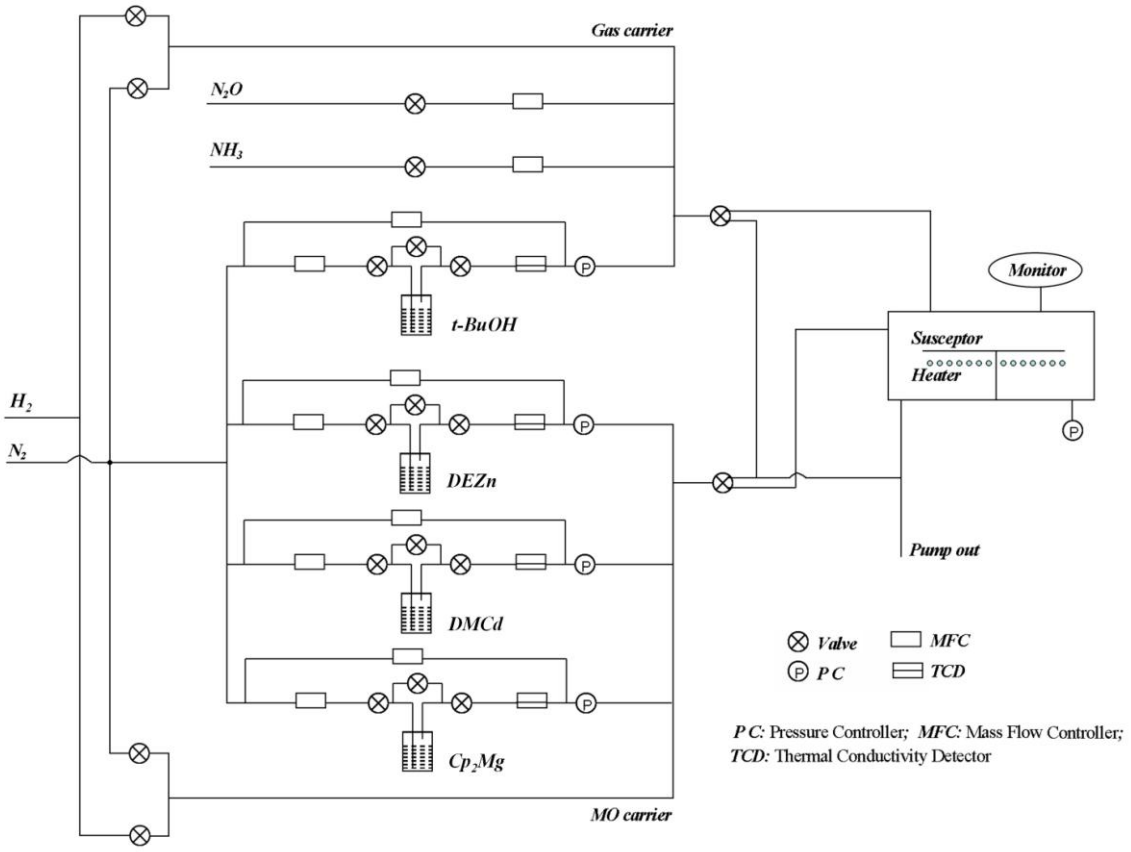

Fig.3.5 Gas flow schematics of vector flow modulated MOVPE tool at the MiNaLab/UiO used in the present thesis.

Table 3.1 List of vapor pressures of different metal organic (MO) sources along with gases available at MiNaLab for fabrication of II-oxides and III-nitrides, including dopants sources

Metal organic precursors		**P at 298 K (Torr) Log P = B – A/T**	**A**	**B**	**Melting point (^{o}C)**
$(C_2H_5)_2Zn$	**Zn**	8.53	2190	8.280	-28
$Mg(C_5H_5)_2$	**Mg**	0.048	3372	10.00	176
$Mg(CH_3C_5H_4)_2$	**Mg**	0.18	2358	7.3	29
$(CH_3)_2Cd$	**Cd**	35.64	1850	7.760	-4.5
$C_4H_{10}O$	**O**	56	-	-	24
$(CH_3)_3Al$	**Al**	14.2	2780	10.48	15
$(CH_3)_3Ga$	**Ga**	238	1825	8.50	-15.8
$C_4H_{11}P$	**P**	353.64	1539	7.713	4
$(CH_3C_5H_4)CuCN$ $[C(CH_3)_3]$	**Cu**	0.015	3669.8	13.478	76
NH_3	**N**	-	-	-	-
N_2O	**N+O**	-	-	-	-

Moreover, Figure 3.6 shows a schematic of source bubbling and metal organic (MO) sources in Table 3.1, which are commonly utilized to grow II-oxide materials using MOVPE.

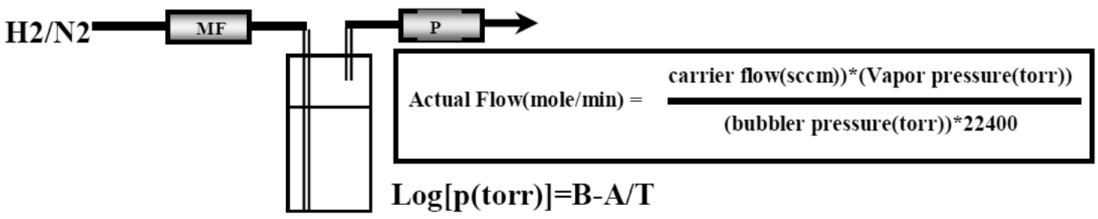

Fig.3.6 Schematic of source bubbling.

3.3.2 Reactor chambers

MOVPE reactor systems (comprising the reaction chamber and all associated equipment) must provide several basic functions in common to all types of systems. It must allow reactants and diluent gases to move to the reaction zone and provide activation energy to the reactants (heat, radiation, plasma) while maintaining a specific system pressure and temperature. Moreover, the reactor might allow the chemical processes for film deposition to proceed optimally and to remove the by-product gases and vapors. These functions are to be implemented with adequate control, maximal effectiveness, and safety when operating.

The reaction chamber is typically a vessel in which the precursors are mixed and approach a heated zone where an appropriate substrate is located, so that the pyrolysis reactions, e.g., Eq.3.3, take place exactly in this area.

Importantly, the flow modulation approach to multiple wafer deposition used at the

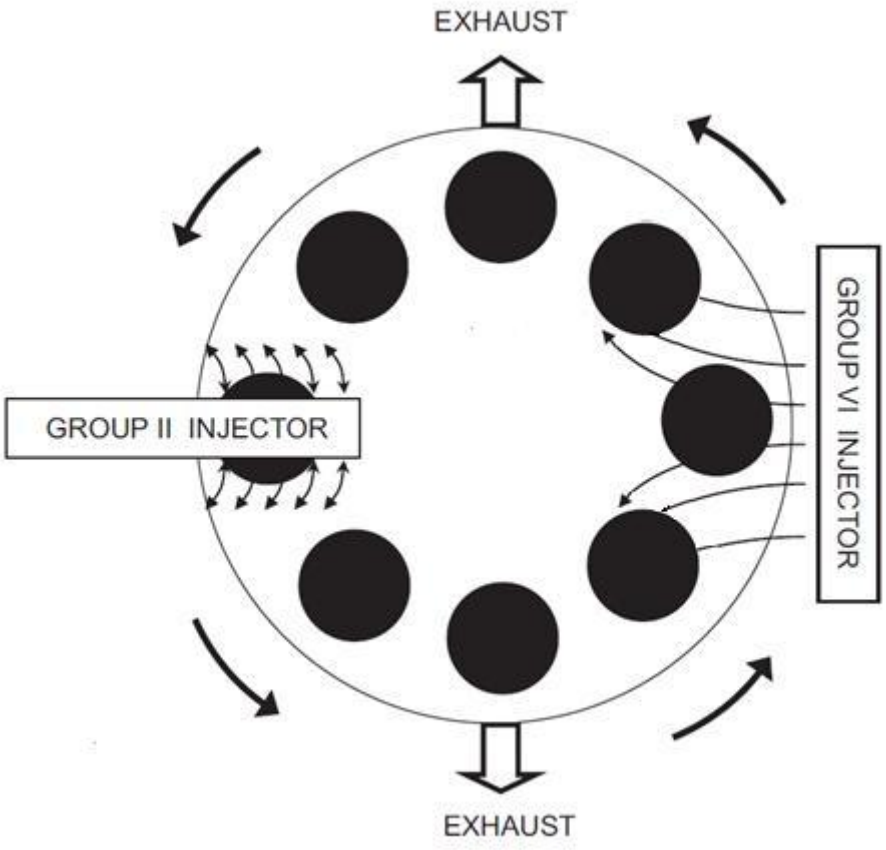

Fig.3.7 Schematics of the MiNaLab MOVPE reactor chamber. Note the mixing between group II and VI precursors is blocked by the presence of the tangential exhausts.

MiNaLab (see Fig.3.7) was developed by EMF Ltd. This method is called vector flow epitaxy, when Group II and VI precursors are introduced separately over a rotating susceptor platen, as shown in Fig.3.7. The chamber is equipped with a radial injector for the group II species, a tangential injector for the group VI species and two tangential exhausts orthogonal to the group VI injector. The rotation of the platen directs the gases across the substrates and out through separate exhausts, thus keeping the gases ideally separate in the reactor chamber [83]. As a result, an advantage of alternative dosing of the substrates with group II and group VI precursors and their full consumption in the reaction zone prevents pre-reactions in the chamber. In addition to keeping the reactants separate, the reactor runs at nearly atmospheric pressure to encourage the efficient use of precursors by maximising the reactant partial pressure, which simplifies the operation of the system.

3.3.3 Exhaust treatment

Safety is an important issue in MOVPE because of various toxic gases used as sources. Process gases should be piped in leak-free coaxial tubing with an inert purge gas or vacuum in the outer tube. Adequate exhaust hoods and cabinets should be used to contain the growth apparatus itself. Waste gases should be processed with filters, combustion discharge, oxidation, wet chemical scrubbing, or a combination of these methods. Automatic shutdown of source gases and a switch to inert purge gases should take place in the event of power failure when inadequate backup power is available. In addition, adequate toxic- and flammable-gas monitoring is provided at along the process chain, including cabinets and hoods, purge lines, and effluent gas treatment lines. Specifically for treating the exhaust at the MiNaLab reactor, we use CLEANSORB - specialized metal organic dry bed absorber system and Centrotherm - waste gas abatement system FLAWAMAT P300K4, which can operate in burn/wet scrub mode and wet scrub mode alone for treating NH_3 gas (see Fig.3.8).

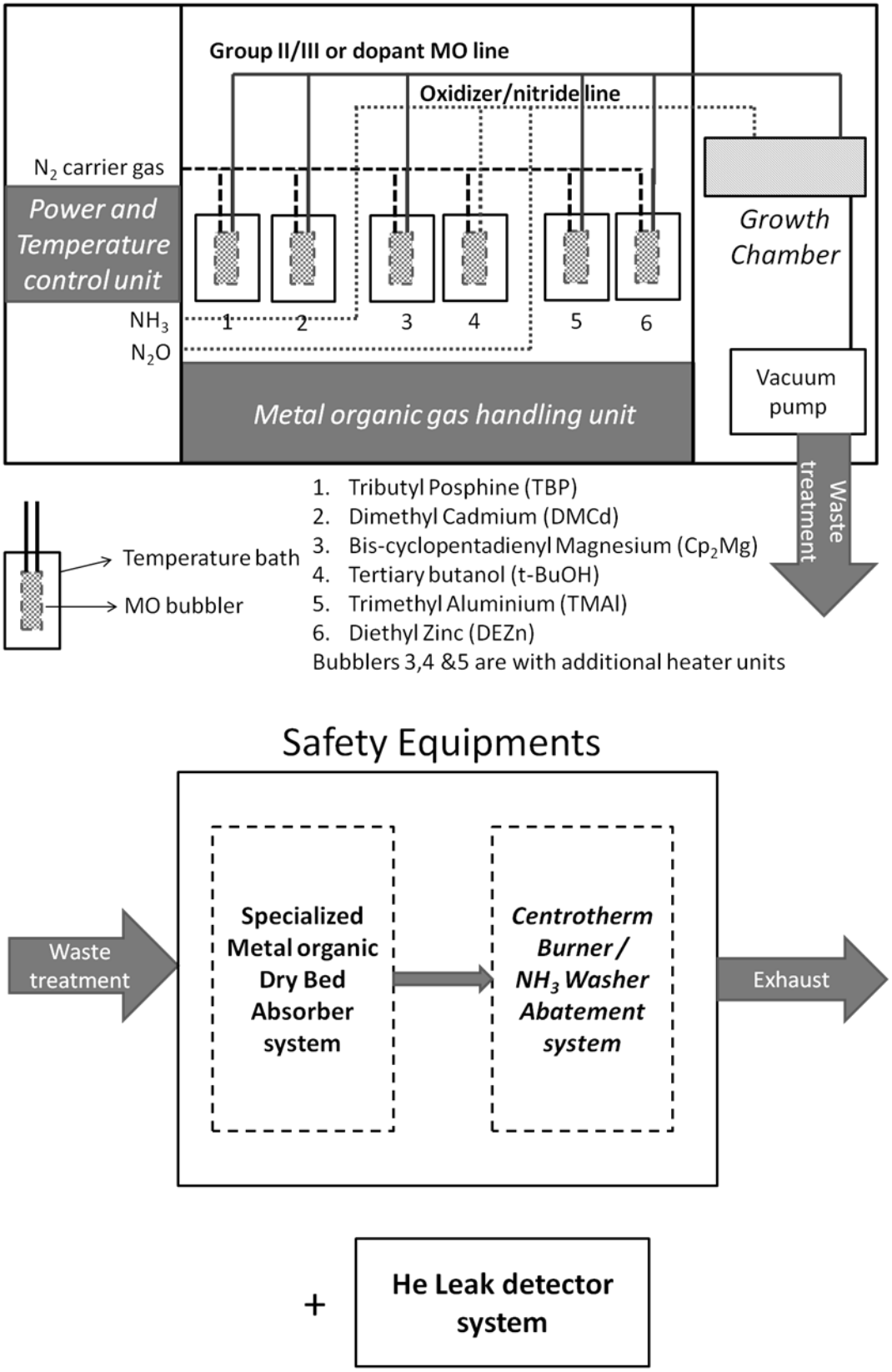

Fig.3.8 Schematics of gas handling system layout of MOVPE tool and exhaust waste treatment facility available at MiNaLab/UiO.

Chapter 4

Characterization methods

This chapter is organized as follows: Section 4.1 describes x-ray diffraction (XRD) technique used to characterize the structural properties of the MOVPE-ZnO films grown. The next two sections (Sec.4.2 & 4.3) describe techniques used to characterize optical properties (PL – defect levels and UV-Vis spectroscopy – band gap). Both XRD and PL are extensively employed to characterize all the samples in the present work, while UV-Vis spectroscopy is employed to study the band gap tuning in ZnO-CdO system. Sections 4.4 and 4.5 are devoted to the tools to characterize vacancy-type defects and chemical composition analysis. Finally, section 4.6 describe techniques used to characterize surface morphology.

4.1 X-ray diffraction

X-rays are electromagnetic radiation with typical photon energies in the range of 100 eV - 100 keV. For diffraction applications, only short wavelength x-rays (hard x-rays) in the range of a few angstroms to 0.1 angstrom (1 keV - 120 keV) are used. Because the wavelength of x-rays is comparable to the size of atoms, they are ideally suited for probing the structural arrangement of atoms and molecules in a wide range of materials. Thin film diffraction methods are used as important process development and control tools, as hard x-rays can penetrate through the epitaxial layers and measure the properties of both the film and the substrate.

There are several special considerations for using XRD to characterize thin film samples. First, reflection geometry is used for these measurements as the substrates are generally too thick for transmission. Second, high angular resolution is required because the peaks from semiconductor materials are sharp due to very low defect densities in the material. Basic XRD measurements made on thin film samples include:

Precise lattice constants measurements derived from 2θ - θ scans, which provide information about lattice mismatch between the film and the substrate and therefore is indicative of strain & stress

Rocking curve measurements made by doing a θ scan at a fixed 2θ angle, the width of which is inversely proportionally to the dislocation density in the film and is therefore used as a gauge of the quality of the film.

Glancing incidence x-ray reflectivity measurements, which can determine the thickness, roughness, and density of the film. This technique does not require crystalline film and works even with amorphous materials.

4.1.1 θ/2θ Diffractometer

Mostly used basic measurement geometry of x-ray diffraction instrument is depicted in Fig.4.1. The sample should preferably exhibit a plane or flattened surface. The angle of both the incoming and the exiting beam is θ with respect to the specimen surface. This measurement geometry may be applied to the investigation of thin films, especially if the layer is polycrystalline/ highly textured and has been deposited on a flat substrate, as is often the case.

The diffraction pattern is collected by varying the incidence angle of the incoming x-ray beam by θ and the scattering angle by 2θ while measuring the scattered intensity I(2θ) as a function of the latter. Two angles have thus to be varied during a θ/2θ scan and in the present study the sample is fixed while both the x-ray source and the detector rotate by θ simultaneously. The rotations are performed by a so-called goniometer, which is the central part of a diffractometer. Typically the sample is mounted on the rotational axis, while the detector and/or x-ray source move along the periphery, but both axes of rotation coincide. The collected diffraction pattern I(2θ) consists of two sets of data: a vector of 2θi positions and a second vector with the appropriate intensities I_i. The step size $\Delta 2\theta_i$

between two adjacent $2\theta_i$ should be chosen in accordance with the intended purpose of the data. For chemical phase analysis the full width at half maximum (FWHM) of the tallest Bragg peak in the pattern should be covered by at least 5 to 7 measurement points. However, for a microstructural analysis in excess of 10 points should be measured on the same scale. The appropriate value of $\Delta 2\theta_i$ will also depend on the slit configuration of the diffractometer. The preset integration time of the detector per step in $2\theta_i$ should allow the integral intensity of the smallest peak of interest to exceed the noise fluctuations $\sigma(I)$ by a factor of 3 or 5, etc., according to the required level of statistical significance.

Most systems operate in the so-called Bragg–Brentano or parafocusing mode. In this configuration a focusing circle is defined as positioned tangentially to the sample surface (see Fig.4.1). The focusing condition in the Bragg–Brentano geometry is obeyed when the x-ray source and detector are positioned on the goniometer circle where it intersects the focusing circle. True focusing would indeed occur only for a sample that is bent to the radius of the focusing circle R_{FC}. Since R_{FC} differs for various scattering angles 2θ, true focusing cannot be obtained in a $\theta/2\theta$ scan and the arrangement is thus termed parafocusing geometry.

In a $\theta/2\theta$ scan the scattering vector Q is always parallel to the substrate normal. It is, however, evident from the above considerations and from Fig.4.1 that this is strictly valid only for the central beam, while slight deviations from the parallel orientation occur for

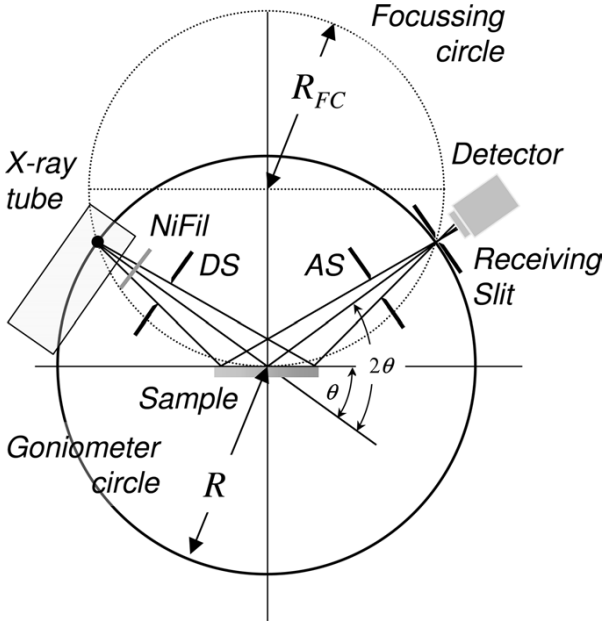

Fig 4.1 Schematic representation of $\theta/2\theta$ diffraction in Bragg–Brentano geometry.

the divergent parts of the beam. If the most divergent rays deviate by $\pm\delta$ from the central beam their scattering vector is tilted by δ from the sample normal – at least for those scattering events that are received by the detector. In many configurations of diffractometer optics it suffices to consider only the central beam. (Refer "*Thin Film Analysis by X-Ray Scattering*" by Mario Birkholz for more details)

4.1.2 Glancing incident X-ray diffraction

The conventional Bragg-Brentano (also called θ- 2θ) XRD geometry is not useful for the study of ultra thin, graded composition and multilayered thin films, partly because of poor sensitivity and partly because of the presence of the interfering effect of the substrate. A useful geometry must be based on a low angle of incidence of X-ray, so as to be able to probe the material up to a specific depth. One of the glancing incidence diffraction (GID) geometries is similar to configuration shown in Fig.4.1, which is slight modification of conventional Bragg-Brentano geometry. As shown in figure, X-rays pass through a suitable slit system and are made to fall on the sample at a glancing angle (α) while the detector on the 2θ axis scans the XRD pattern. The diffracted beam optics is modified to a parallel beam optics and a flat plate monochromator is incorporated in the diffracted beam. The conventional powder methods are applicable in analyzing the GID patterns.

4.2 Photoluminescence

Photoluminescence (PL) is the emission of an optical radiation by a solid following photonic excitation [64, 107]. PL is a three-step process including the photo-generation of electron-hole pairs by absorption of the incident radiation in the near surface region, the radiative recombination of electron-hole pairs, and the escape of the resulting photon. Figure 4.2 illustrates the various recombination processes in semiconductors, as described in the book by Landsberg.[108] In this section, the concepts of free and bound excitons are explained and the radiative transitions illustrated in Fig.4.2 are described. The PL analysis techniques used throughout this study are then presented.

4.2.1 Excitons and the near-band-edge region of the PL spectrum

The concept of exciton in covalent solids was developed by Wannier in 1937 [109]. An exciton is a particle that consists of an electron and a hole, both moving in extended orbits with a correlated motion, hence the concept of electron-hole pair. Put simply, an exciton is a bound state of an electron-hole pair. An exciton falls into two categories: (i) the free exciton, existing as a hydrogenically bound electron-hole pair, and (ii) the bound exciton, composed of a free exciton molecularly bound to a defect. The valence band in wurtzite ZnO is split into three sub-bands by the combined effects of spin-orbit interaction and of the crystal field. The three upper valence bands result in three intrinsic excitonic states (within ~45 meV) [110] commonly denoted A, B and C excitons and labelled as X_A, X_B and X_C respectively. Note that the energy positions of free excitons vary substantially depending on the epilayer strain. Excitons can bind to neutral or ionized point defects and form bound exciton complexes. There exist several types of bound excitons, as illustrated in Fig. 4.3. For example, an exciton bound to a neutral donor (D^oX) consists of a donor ion, two electrons and a hole [111]. Ionized acceptors are unlikely to bind excitons since a

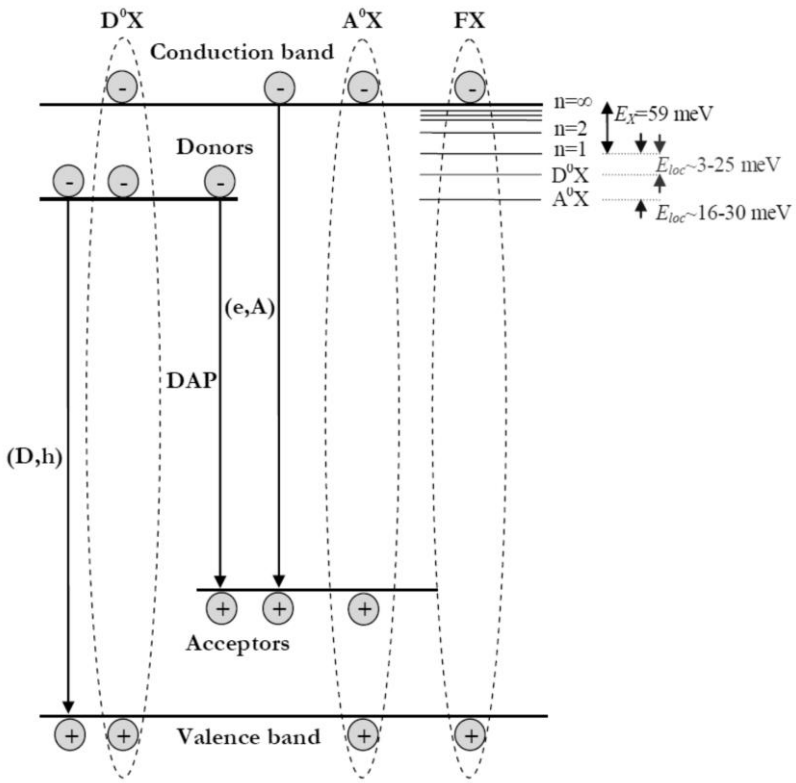

Fig.4.2 Band diagram illustrating the radiative transitions. After Ref. 64

neutral acceptor and a free electron are energetically more favourable [112].

Experimentally, the NBE portion of the PL spectrum of undoped ZnO crystals features several sharp and structured transitions, labelled I_0 to I_{11}, within a 3 nm-wide wavelength region. These are due to the recombination of excitons bound to ionized and neutral defects. Much research has focused on the identification of the donors and acceptors associated with these transitions [110]. Recent findings show that I_0, I_1 and I_2 are ionized donor states associated with I_{6a}, I_8 and I_9 respectively, increasing to seven out of twelve the number of unambiguously identified excitons in ZnO.

4.2.2 Electron-phonon coupling

Every optical transition involves the creation of one or more phonons. For an optical transition accompanied with phonon creation, the photon energy $h\nu_{m,n}$ is given by:

$$h\nu_{m,n} = E_{ZPL} - mE_{LO} - nE_{TO} \qquad (4.1)$$

Where E_{ZPL} is the transition energy of the zero-phonon line (ZPL), m is the number of created longitudinal optical (LO) phonons, E_{LO} is the energy of the LO phonon, n is the number of created transverse optical (TO) phonons and E_{TO} is the energy of the TO phonon. In ZnO, the coupling to TO-phonons is generally so weak that TO-phonon replicas do not appear in the PL spectrum. LO-phonons in ZnO have a frequency of 591cm^{-1}, corresponding to a 71.5 meV energy

4.2.3 Temperature dependence of PL transitions

The temperature dependence of the band gap energy can be fitted by several equations.

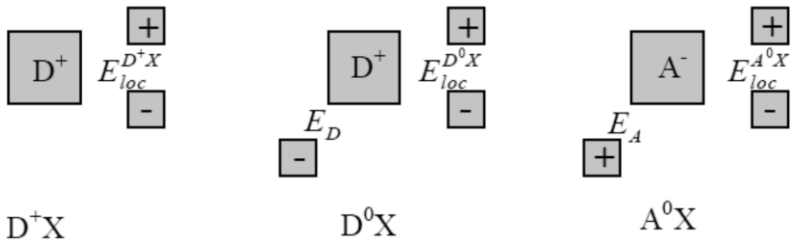

Fig.4.3 Illustrations of excitons bound to (a) an ionized donor D^+, (b) a neutral donor D and (c) a neutral acceptor A. After Ref. 64

The semi-empirical Varshni equation gives [113]:

$$E_G(T) = E_G(0) - \alpha \frac{T^2}{T+\beta} \quad (4.2)$$

where $E_G(0)$, α and β are fitting parameters.

4.2.4 Excitation intensity dependence of PL transitions

The lifetime and concentration of defects in ZnO are finite therefore it is possible to saturate defect-related luminescence when using high excitation intensities. The luminescence intensity I of a near-band-edge PL transition is proportional to F_β, where F is the laser excitation intensity and β is a dimensionless exponent. For bound excitons, 1< β <2, while for DA or free-to-bound transitions, β <1 [114].

A characteristic of DA transitions is to blueshift under increasing excitation intensity. Indeed, the number of occupied donor and acceptor centers increases; their average distance necessarily decreases, which shifts the band peak energy toward the blue because of the Coulomb energy term [112]

4.3 Revealing band gap variations by optical absorption

UV-Vis Absorption spectroscopy measures the percentage of radiation that is absorbed at each wavelength. Typically for characterizing thin films, this is done by scanning the wavelength range and recording the absorbance. When the energy of the incoming photon matches ΔE, the photon is absorbed, and an electron from an occupied level "jumps" from its ground state to an empty level (also called an excited state). Here, ΔE is defined as the energy difference between an occupied orbital (ground state) and an empty (excited state) orbital. Some of these films are transparent to UV-Vis radiation while others are not. For non-transparent highly scattering thin films, an integrating sphere accessory is needed to capture and then detect all the reflected light. This is known as a diffuse reflectance measurement.

4.3.1 Measurement of the electronic band gap of semiconductor films

A classical semiconductor exhibits minimal optical absorption for photons with energies smaller than the band gap and high absorption for photons with energies greater than the band gap. As a result, there is a sharp increase in absorption at energies close to the band gap that manifests itself as an absorption edge (or "reflection threshold") in the UV-Vis absorbance spectrum. While the absorption edge is indicative of the location of the band gap, accurate estimation of the band gap requires use of the following formula:

- For direct band gap semiconductors :

$$\alpha(\hbar\omega) \propto \frac{\sqrt{\hbar\omega - E_{gap}}}{\hbar\omega} \quad (4.3)$$

  where **α** is the absorption coefficient, $\hbar\omega$ is the energy of incident photons and E_{gap} is the electronic bandgap of the semiconductor. E_{gap} is the intercept of the straight line obtained by plotting $(\alpha(\hbar\omega))^2$ vs $\hbar\omega$

- For indirect bandgap semiconductors :

$$\alpha(\hbar\omega) \propto \frac{(\hbar\omega - E_{gap})^2}{\hbar\omega} \quad (4.4)$$

  Eg is the intercept of the straight line obtained by plotting the square root of $(\alpha(\hbar\omega))$ vs $\hbar\omega$.

4.4 Sensing vacancy-type defects with positron annihilation spectroscopy

Positron Annihilation Spectroscopy (PAS) is emerging as a unique probe for low levels of open-volume-type defects. The salient features of the technique are: Non-destructiveness, depth-sensitivity, and ease of use. In PAS, positrons from a radioactive source are introduced in a sample and outgoing gamma rays which follow positron annihilation with electrons in the sample are detected and analyzed. There are three main techniques of positron annihilation spectroscopy and which can be used both with the positrons from sources and slow positron beams: 1) positron annihilation lifetime spectroscopy (PALS), 2) Doppler broadening spectroscopy and 3) angular correlations measurements. The

principles of these techniques are illustrated in Fig.4.4. In the positron annihilation lifetime spectroscopy, when used with radioactive sources, ^{22}Na is usually used as positron source.

PALS is based on the measurements of the time difference between 1.28 MeV γ - ray, emitted from the daughter ^{22}Ne nucleus almost immediately after positron emission from the ^{22}Na, and one of the annihilated 511 keV γ -rays emitted in positron annihilation. The collected time spectra contain various lifetime contributions and decomposition in individual time components and corresponding intensities can yield information about holes in the sample and their concentrations. This technique, when used with slow positron beam, should include some gating from the incoming positrons in beam, but with the definite positron energy, the exact penetration depth can be determined.

In Doppler broadening spectroscopy the precision measurement of energy shift of the annihilated 511 keV γ -ray as a consequence of non-zero momentum of annihilated positron and electron pairs is used to extract information about electron distributions in the investigate sample. This non-zero momentum of annihilated positron-electron pairs causes also deviation from co-linearity of the two outgoing γ -rays, and these angular deviations can be registered in γ - γ coincidence measurements in one or two dimensions, and form basis of angular correlation measurements. But to achieve required angular resolution in these measurements gamma ray detectors should be several meters apart and require special laboratory arrangements.

4.4.1 Depth resolved Doppler broadening spectroscopy

The depth-resolved PAS method is based on the availability of beams [115,116] of positrons that can be used to probe various controlled depths (in the few μm range) [117] of a material. When positrons are implanted into a material, they are thermalized rapidly through inelastic collisions. The thermalized positrons diffuse and annihilate with electrons, either from a freely diffusing state or from a trapped state (at a defect site), predominantly producing two gamma rays. Because of the center of mass motion of the annihilating positron-electron system, the gamma rays will be Doppler shifted from the center energy of 511 keV. Because the positrons are thermalized, the Doppler shift will be dominated by the momentum of the electrons participating in the annihilation, and can be used to study the properties of the electron momentum distribution. In an experiment

where energies of the several annihilation photons (both up shifted and down shifted) are recorded, the Doppler shift of the individual γ-ray line will contribute to an overall broadening of the annihilation photo-peak; this is often called Doppler broadening [116]. This broadening contains information about annihilation environment (e.g. if voids are present less annihilation occurs on high-momentum core electrons and resulting peak is less broadened).

The Doppler broadened spectrum can be characterized by using some part of the momentum spectra: One such parameter is an S parameter, defined as the ratio of counts (i.e., area) in a central region of the photo-peak to the total counts (area) in the peak. The S parameter has a simple relationship to the Doppler broadening: For example, if the annihilation peak is narrow, which results when positrons annihilate predominantly with slow-moving electrons, the S parameter is large, and vice versa. Thus, annihilations with the valence electrons are reflected in the S parameter. Similarly the wing region of the spectrum (defined as W parameter) can be used to examine the contributions from core

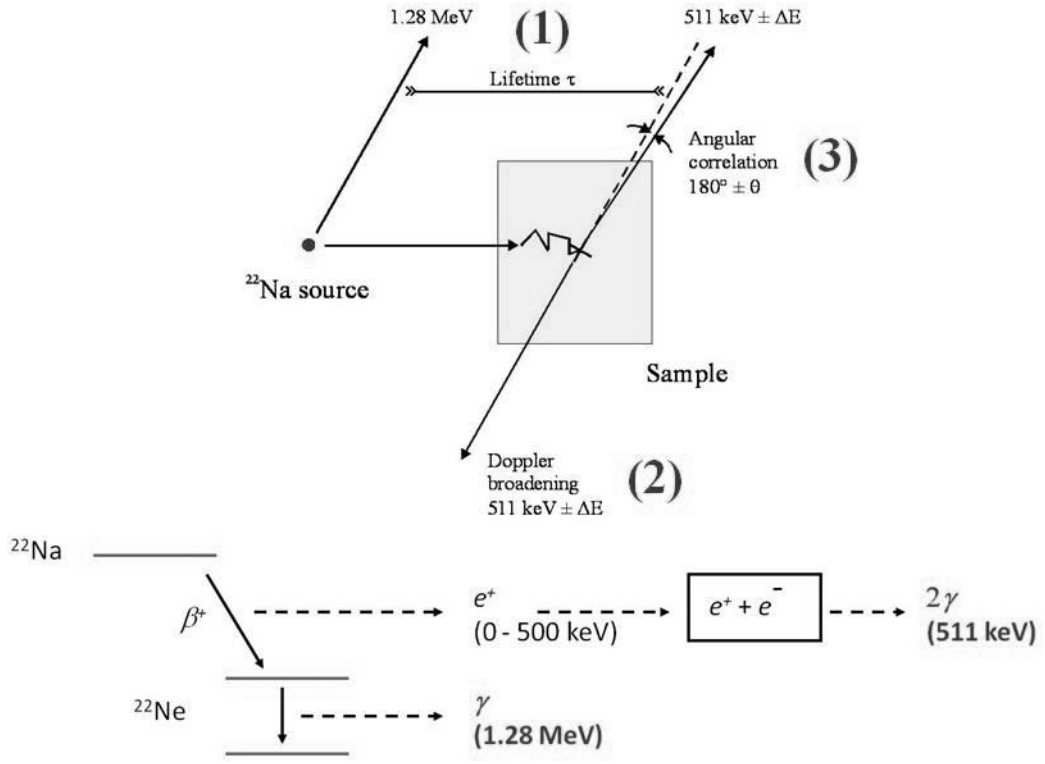

Fig.4.4. Principles of three main techniques in positron annihilation spectroscopy (here presented with ^{22}Na positron source): 1) Positron annihilation lifetime spectroscopy, 2) Doppler broadening spectroscopy and 3) Angular correlations measurements.

electrons in Doppler broadening. The definitions of S and W are shown in Fig.4.5.

The use of simple parameters such as S and W yields extensive information about the low-density region (open-volume-defects) of a solid material. The absolute values of S and W parameters have little physical relevance, since they are essentially decided by the position of the windows chosen in their definition. It is the relative change in these parameters that carries information about the annihilation sites. Therefore S and W parameters are usually normalized to a reference value corresponding to the defect-free (as seen by positrons) value of the material under investigation. The normalized value can then be compared between different samples and experimental arrangements. Because Doppler broadening parameters can be measured and interpreted very rapidly, they are used extensively in defect-related studies.

$$Z[nm] = \frac{AE[keV]^n}{\rho[gm/cm^3]} \qquad (4.5)$$

The S parameter is usually measured as a function of positron beam energy (E), resulting in S-E data. The energy can be converted to an approximate mean depth by using Eq. 4.5, where A and n are material dependent constants and ρ is the density of the test material. The S-E data can be analyzed using a diffusion-annihilation equation [116] using computer codes like VEPFIT [118]. The analysis yields parameters such as: S-parameter of a particular region of the test system, positron diffusion length, internal electric field, and boundary between different regions. The positron diffusion length can easily be

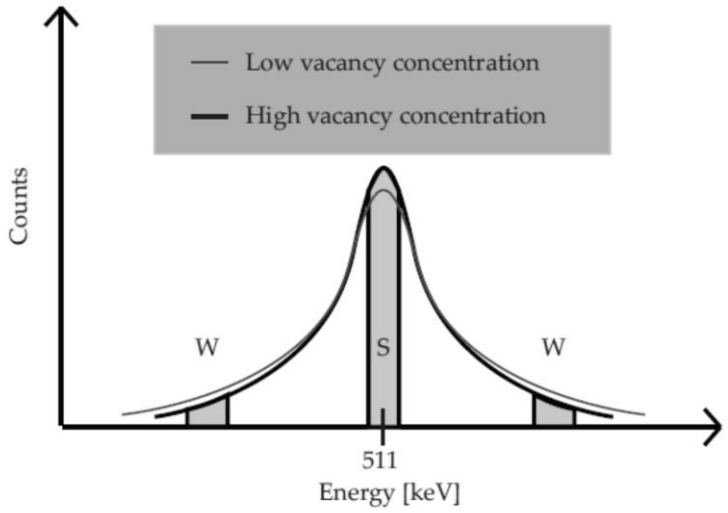

Fig.4.5 Definitions of S and W line shape parameters.

correlated to the defect concentration [116].

4.5 Rutherford backscattering spectroscopy

Rutherford Backscattering Spectrometry (RBS) is a widely used nuclear method for the near surface layer analysis of solids. Basically, the method which is schematically shown in Figure 4.6, consists of placing a target in a monoenergetic $^4He^+$ ion beam coming from an ion accelerator. α-particle beams interact with the sample and some of the ions are elastically scattered by surface atoms while other ions penetrate the target, lose some energy and are backscattered at various depths. Particles coming from the target as a result of these interactions are detected and analyzed, and, using electronic techniques, one obtains a backscattering energy spectrum, i.e. the number of backscattered α-particles as a function of their energy (see Figure 4.6). It is this RBS energy spectrum which contains the information on the nature of the various elements present in the target and their depth distribution. The first important feature of RBS is its ability to distinguish the atomic masses of the elements present in the target

As shown in Fig.4.6, when $^4He^+$ collides with surface atoms, the energy of the ions after such an elastic scattering event is smaller than its initial energy (E_o) and the missing energy has been carried away by the recoiling target nuclei. The ratio of the energy after and before the scattering event is the kinematic factor *K* which depends on projectile (m) and target (M) masses and on scattering angle θ; for instance at θ = 180^o one obtains:

$$K = [(M-m)/(M+m)]^2 \qquad (4.6)$$

Note that the kinematic factor increases with the target mass and tends towards unity for heavy masses, thus the mass separation on the RBS energy spectrum decreases when the mass increases. Once E_o *is* fixed, the energy of backscattered particles (KE_o) depends only on the nature of the surface atoms. Therefore, the energy scale of the RBS spectrum can be transformed into a mass scale. In fact if different species A and B (see Figure 4.6) are present in the surface, due to their mass difference, their elastic kinematic factor will be different and consequently the energy of α- particles after scattering on A or B surface atoms will be also different. The measurement of the energy of backscattered particles permits the direct determination of the nature of the element present in the surface. When $^4He^+$ ions penetrate in the target, two phenomena occur: the a-particles lose part of their energy, and they can be elastically scattered by target nuclei. The energy losses during the

penetration of α in the matter are essentially due, in the MeV energy range, to the interactions with the electrons of the medium [119]. At a depth X (see Figure 4.6) the α-particles have an energy (lower than E_o) which is a function of the stopping power of the medium. Moreover, the ions elastically scattered at a depth X lose energy during the outgoing path before being detected with an energy *E*. As the energy loss is greater for particles backscattered from larger depth than those from shallower depth, a depth scale, i.e. a relationship between X and the energy of the backscattered particles, can be defined. More precisely, it is possible to relate the depth location X (expressed in atoms cm^{-2}) of atoms to the measured energy difference *ΔE* between the theoretical surface position *(KE_o)* and the detected energy E ($\Delta E = KE_o - E$) of α-particles backscattered by the atoms at depth X; the relation being the following:

$$\Delta E = X[K\varepsilon(\bar{E}_{in}) + (1/\cos\theta)\varepsilon(\bar{E}_{out})] \qquad (4.7)$$

where $\varepsilon(\bar{E}_{in})$ and $\varepsilon(\bar{E}_{out})$ are the stopping cross-sections in the incoming and outgoing path with $\bar{E}_{in}$ and $\bar{E}_{out}$ the respective average incoming and outgoing energy for the α-particles. Thus, in establishing such a depth scale, the stopping cross-section for $^4He^+$ of a given target must be known. Moreover, the statistical fluctuation of the energy loss leads to the energy straggling which gives a broadening towards the lower energies of the spectra corresponding to the various elements. Thus, both energy loss and energy straggling are essential for the interpretation of RBS spectra, and compilations have been done [119].

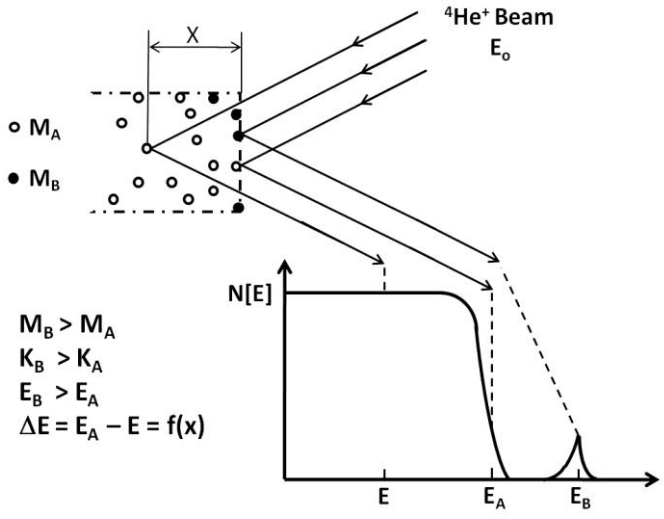

Fig.4.6 Basic principles of Rutherford backscattering analysis.

One must note that the maximum depth analysis in RBS is defined by the depth from which the scattered particles emerge with zero energy, and typical depths of analysis with 2 MeV He ions are in the micron range. The fact that the energy scale in RBS can be converted to a depth scale leads to numerous applications in the field of localization of atoms (impurity, marker or implanted species) in substrates. The main applications are therefore the determination of stoichiometry of compounds and of thickness of thin films, which are important points in the field of compound formation and alloy composition.

In the case of a crystalline substrate aligned with the incoming beam, i.e. in channeling geometry, additional information may be obtained on the structure of the target as shown in Figure 4.7 The possibility of such surface studies using channeling is related to the fact that when a beam of particles is aligned with a major crystallographic axis, the backscattering yield is very much higher for the very first surface layers than in the bulk. This is due to the formation of a shadow cone for the incident $^4He^+$ beam (see Figure 4.7) by the first atomic plane and by atoms which are displaced from crystallographic sites. Thus, information on the surface disorder is obtained from the comparison of aligned and random spectra.

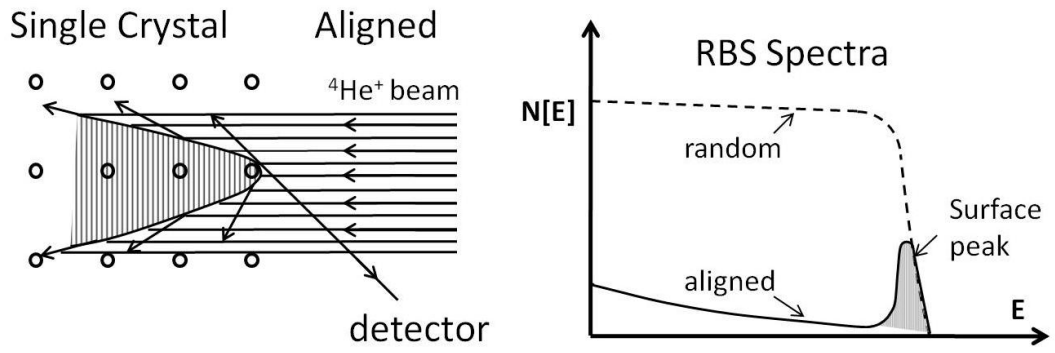

Fig.4.7 Schematic description of RBS in channeling geometry

4.6 Surface roughness / morphology imaging using atomic force and secondary electron microscopies

4.6.1 Atomic force microscopy (AFM)

The AFM makes use of a sharp tip at the end of a flexible cantilever to scan and probe the sample surface. The cantilever, and in particular the cantilever tip, is the most relevant part of the AFM because it interacts with the sample and determines the maximum resolution obtainable (Fig.4.8). The interaction forces between the tip and the sample are usually determined by monitoring the deflection of the cantilever, modeled as a very sensitive spring with known stiffness. The deflection, and thus the force, is usually monitored by focusing a laser beam on the back side of the cantilever and recording changes in the reflected beam angle using a segmented photodiode. Various imaging modes have been developed during the last two decades, the most popular being *contact* mode, *intermittent contact* or *"tapping"* mode, and *force mapping* or *"force volume"* mode. Force mapping mode takes advantage of the capacity of the AFM to obtain mechanical measurements of samples by the acquisition of force–displacement (F–z) curves. These curves are obtained by oscillating the AFM cantilever in the vertical

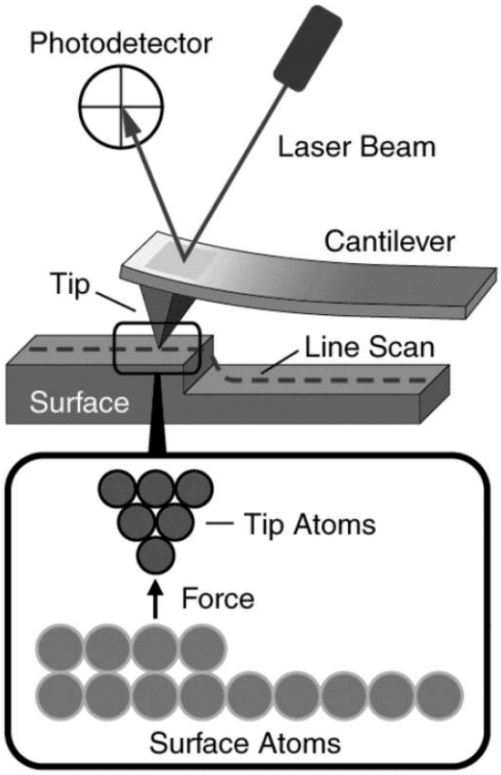

Fig.4.8 Principle of Atomic force microscopy (AFM) (*www.afmuniversity.org*)

direction, perpendicular to the sample surface, and monitoring its deflection as it interacts with the sample surface. Both imaging and force modes have been extensively used to investigate the topography, adhesion, and viscoelastic properties of many biological samples including ophthalmic tissues.

4.6.1.1 Imaging Modes

AFM images are three-dimensional topographical representations of a sample surface. In imaging mode, the cantilever tip is scanned along the sample surface while keeping the interaction between the tip and the sample constant. This is accomplished by using a feedback loop that continuously corrects the relative position of the cantilever and the sample. A gentler imaging mode is the intermittent contact or “tapping” mode, in which the cantilever is oscillated at its resonant frequency. In this mode, the amplitude of oscillation of the free end of the cantilever is the control parameter. As a freely oscillating cantilever tip approaches the sample surface, its amplitude of oscillation decreases before contact is made. This behavior is due to a thin layer of water that permanently covers surfaces under standard conditions as well as to drag forces and electrostatic, steric, or van der Waals interactions between the tip and the sample in liquid. To keep the cantilever amplitude of oscillation constant during scanning of the sample, the position of the cantilever relative to the sample is continuously corrected, which translates into a three-dimensional replica of the sample surface. Although intermittent contact does not produce AFM images with as high resolution as contact mode, lateral drag forces that may damage the sample are considerably reduced [120,121].

4.6.2 Secondary electron microscopy (SEM)

Electrons in scanning electron microscopes are accelerated at voltages in the range of 2 to 40 kV. An electron beam < 0.01μm in diameter is focused on the specimen. These fast primary electrons (PE) interact in various ways with the surface layers of the specimen. The zone, in which such interaction occurs, and in which different signals are produced, is called "interaction volume" or "electron – diffusion cloud". The size of the interaction volume is proportional to the energy of primary electrons, its shape is determined dependent upon scattering processes by the mean atomic number. Secondary electrons (SE), back scattered electrons (BSE), and absorbed electrons are produced, flowing off as

specimen current. In addition, X-rays, Auger electrons, and cathodoluminescence are produced.

4.6.2.1 Secondary electrons (SE)

Although secondary electrons are produced in the entire interaction volume, they can only escape from surface layers (metals: max. 5μm, insulators: max. 50 μm, Fig.4.9: Escape level t). Secondary electrons are very slow, their escape energy is ≤ 50 eV. Approximately half of all SE are produced very near to the point of impact of PE (SE1). Owing to back scattered electrons (BSE) diffusing in the specimen material, SE are also produced at a distance in the range of 0.1 to some μm to the point of impact (SE2). Back scattered electrons reacting with the wall of the specimen chamber are the third source of SE. This reaction process causes background radiation and thus a smaller degree of contrast, which, however, can partly be increased again electronically. The best lateral point resolution can be achieved by means of SE1. The signal can be intensified when the primary beam hits the samples at an angle of < 90°; this is referred to as inclination contrast. If radiation can penetrate specimen structures such as tips, fibres, or edges, the images of these structures will be very bright (edge contrast) owing to a high SE yield. The SE signal, comprising all essential information on topography, produces electron-micrographs of high resolution.

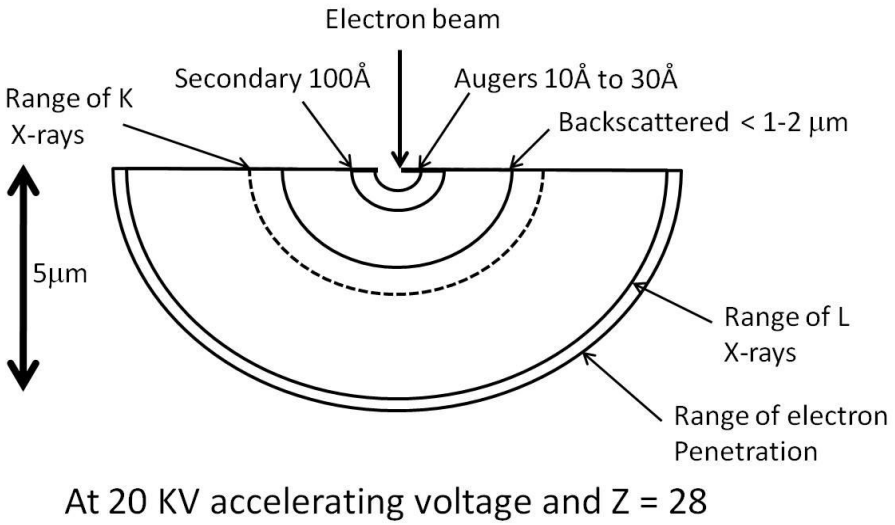

Fig.4.9 The volume inside the specimen in which interactions occur while being struck with an electron beam

4.5.2.2 Back scattered electrons (BSE)

The electrons escaping from the surface of the sample and having an energy of ≥ 50 eV are referred to as back scattered electrons (BSE). BSE are produced in the entire interaction volume at a larger distance to the point of impact of PE (Fig.4.9). When atomic numbers are low, the escape level T is approx. half the range R; at accelerating voltages > 20kV and when atomic numbers are high, the escape level T is lower. The higher the PE energy and the smaller the atomic number of the specimen material, the more extends the area of production of BSE and the lower the achievable resolution. However, the dependence on the atomic number of the sample material is an advantage in that, apart from the topography contrast, a material contrast can be made visible. Moreover, owing to higher energy charging occurs less frequently than in case of SE.

Chapter 5

Exploration of ZnO MOVPE synthesis and mastering of nearly strain free ZnO films on Si(111) by tuning AlN buffer thickness

This chapter highlights results on ZnO thin film synthesis by vector flow epitaxy. The results are presented in two sections. The first section deals with the exploration of ZnO synthesis by vector flow epitaxy by varying different growth parameters; more details can be found in Paper I. The second summarizes mastering of nearly strain free ZnO films on Si(111) by tuning AlN buffer layer thickness, which is basically results extracted from Paper II.

5.1 ZnO growth by vector flow epitaxy

Understanding and control over precursor delivery are of paramount importance in order to make successful MOVPE of ZnO. Most frequently diethylzinc (DEZn) or dimethylzinc (DMZn) are used for supplying zinc while a variety of oxidizing agents - O_2, N_2O, NO_2, CO_2, H_2O, tertiary-butanol (t-BuOH), etc - were tested. Importantly, the key issue in mastering growth is in providing optimal conditions for chemical reactions to occur at the growth front of the film and not anywhere else in the reactor, in other words, avoiding pre-reactions. Concurrently, strong pre-reactions are known to be practically inevitable in

most of conventional reactors at atmospheric pressure and reduced pressure operation is commonly used specifically when oxidizing DEZn. Furthermore, it has been already demonstrated that the minimization of the adduct formation and parasitic reactions can be achieved by employing a novel two-inlet system operating at almost atmospheric pressure, when synthesizing AlN by so called vector flow epitaxy.

Indeed, after choosing a zinc/oxidizing couple, an optimal growth temperature window has to be determined, as it plays an important role on the precursor pyrolysis. For example, in the present study, DEZn and t-BuOH are used as the Zn and O sources, respectively. The pyrolysis of t-BuOH and DEZn has been studied, separately as well as combined, using an isothermal reactor attached to a quadrupole mass spectrometer (see Fig.5.1) [122]. Kinetics of decomposition under hydrogen atmosphere were investigated over the temperature range 200–500 °C, and reaction mechanisms are finally proposed. The decomposition of DEZn was found to be in agreement with previous studies. It starts above 300 °C and leads to the formation of ethylene (C_2H_4) and ethane (C_2H_6). The pyrolysis of t-BuOH begins at higher temperature, 380 °C, and produces water (H_2O) and isobutene (C_4H_8). In case of the co-pyrolysis of tertiary butanol with diethyl zinc, these

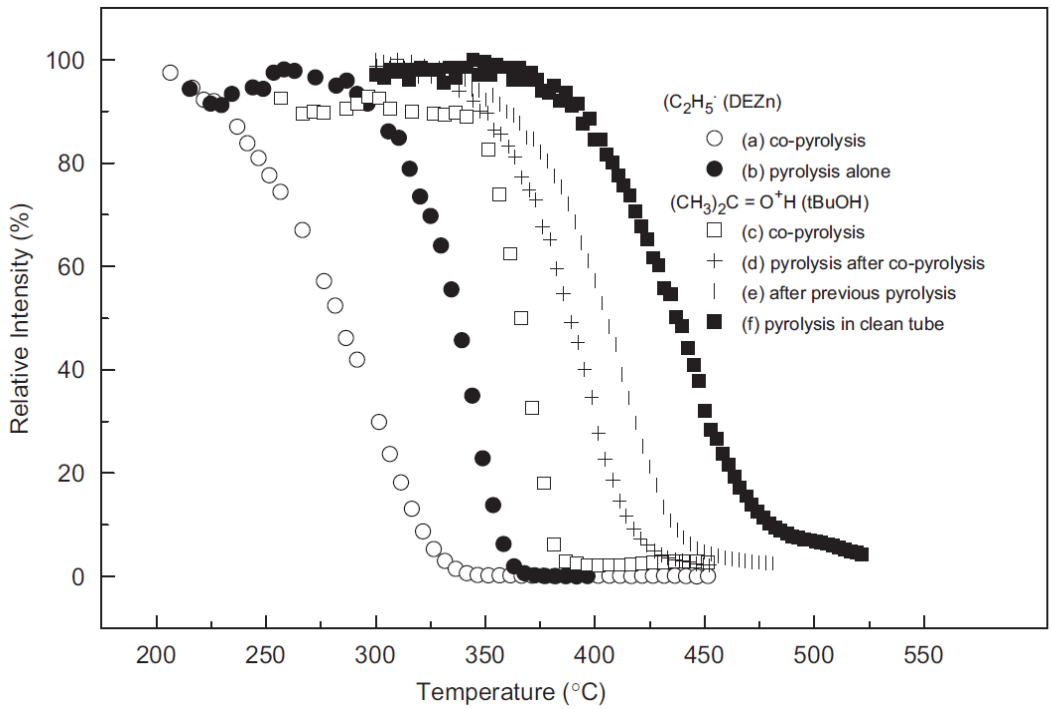

Fig. 5.1 Comparison of decomposition products in co-pyrolysis and separate pyrolysis of DEZn and t-BuOH as the function of temperature. After Ref. 122

same decomposition products appear, indicating a comparable chemical process. It was observed that the onset and the complete decomposition were shifted to lower temperatures. The shift is 30 °C for t-BuOH and 50 °C for DEZn. A ZnO deposit on the reactor walls was also found to influence the pyrolysis.

Secondly, the variation in II/VI molar ratios at the reaction zone, inside the reactor, will also influence the ZnO film growth. Considering 100 % pyrolysis efficiency at the optimum growth temperature, II/VI > 1 would result growth in Zn-rich atmosphere, while II/VI < 1 results in oxygen-rich atmosphere. Moreover, the influence of basic growth parameters – substrate rotation as well as operating pressure/flow – all influencing the precursor delivery to the reaction zone by modulating the residence time of the precursor. The residence time t_r (s) of the precursor is given by

$$t_r = k_t \frac{P \times V}{Q} \qquad (5.1)$$

where P is the gas pressure (Pa), Q the flow rate (sccm), V the volume of the deposition chamber (cm^3), and k_t the constant value. For example, decreasing the chamber pressure by keeping other parameters as constant, will shorten the residence time of the precursor. Importantly, shortening the residence time of the precursors decreases the amount of DEZn/t-BuOH, which actually gets adsorbed on the substrate surface and thereby decreasing the precursor pyrolysis efficiency.

However, the influence of basic growth parameters – all influencing the precursor delivery to the reaction zone have not yet being systematically documented when growing ZnO by employing two-inlet MOVPE system. The purpose of the present work is to recapitulate these missing parts confirming that material properties may be readily tuned as a function of precursor delivery. Crystalline quality (measured by x-ray diffraction - XRD), morphology (assessed by atomic force and secondary electron microscopies – AFM/SEM) and optical properties (monitored by photoluminescence- PL) were investigated as a function of growth parameters in order to quantify the material. Specifically, varying the growth temperature resulted in highly oriented ZnO growth in temperature window of 350 – 385 ^oC, while further increase in growth temperature ($\geq$ 450 ^oC) resulted in nanorod structures as shown in Fig.5.2, possibly due to desorption of Zn from the substrate. Figure 5.3 shows the rocking curve full width at half maximum (FWHM) of high intensity Bragg characteristic peak (ZnO (0002)) from XRD analysis,

which is one of the measures of crystalline quality of the film. Specifically, the deep level emission (DLE) in the visible region of the PL spectra is highly influenced by the growth temperature, due to the precursor pyrolysis leading to Zn/O lean conditions. The DLE of ZnO films fabricated at 700 and 600 Torr are shown in Fig. 5.4. On the other hand, variation in the II/VI molar ratio resulted in nucleation with high grain density with decreasing concentration of t-BuOH, as the free energy ΔG_V increases, while increasing

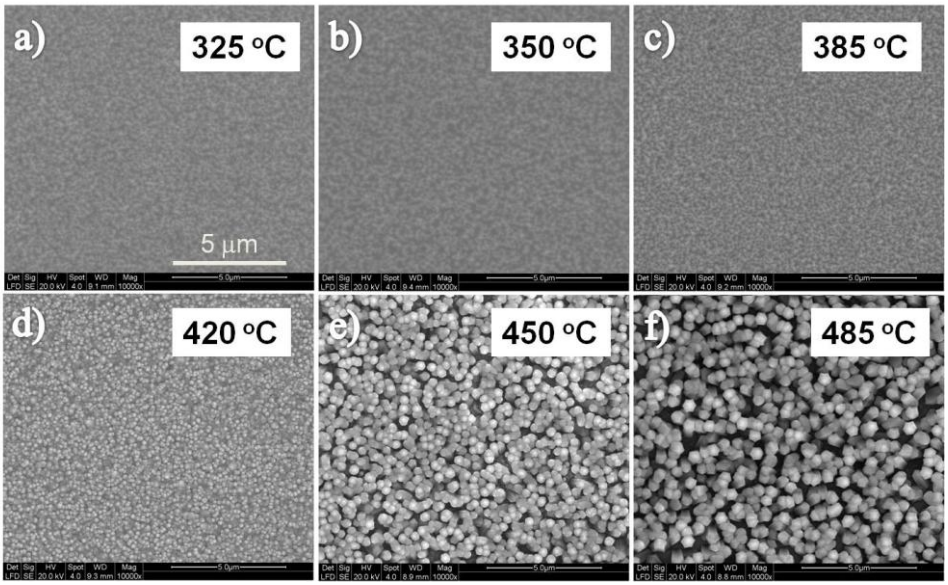

Fig. 5.2 SEM images of ZnO films grown at 700 Torr as a function of temperature keeping DEZn and t-BuOH flow rates at 140 and 60 sccm, respectively.

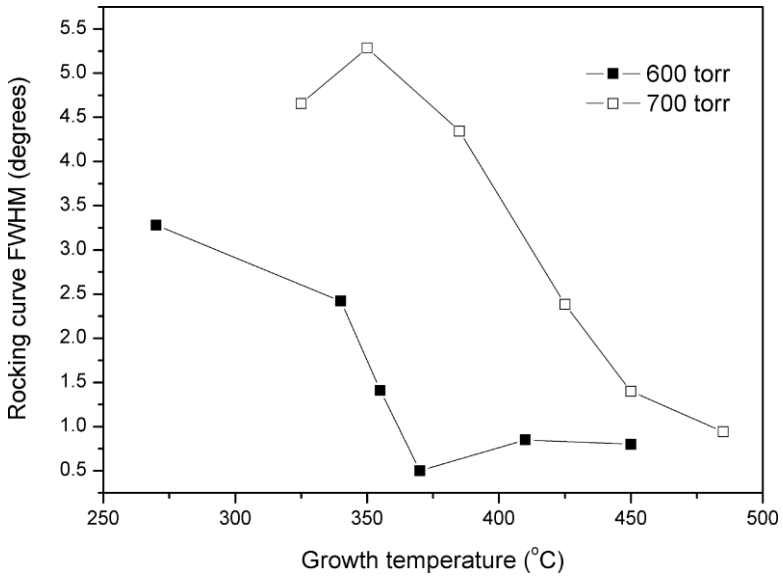

Fig. 5.3. Influence of the growth temperature and chamber pressure on the rocking curve of ZnO films.

the t-BuOH flow, denser nucleation is attained and small grains develop.

In summary, the structural and luminescence characteristics of ZnO films fabricated on c-Al_2O_3 substrates were studied systematically by varying different growth parameters like growth temperature, chamber pressure, II/VI molar ratio, total carrier gas flow rate and rotation rate. In turn, growth temperature evolved to have greater influence on the structural and optical properties, influencing the DEZn and t-BuOH precursor pyrolysis and thereby manipulating the actual II/VI molar ratio available for the ZnO growth. Secondly, the II/VI molar ratio plays a major role on the structural properties and thereby influencing the intrinsic defect nature of the material. The total carrier gas flow rate

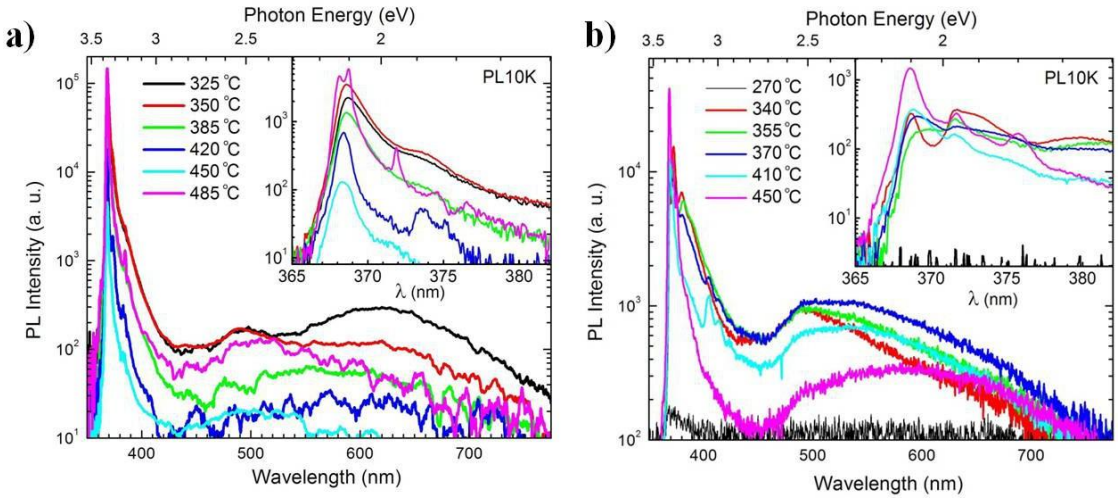

Fig. 5.4. PL spectra of ZnO films grown on c-Al_2O_3 as a function of different growth temperature at (a) 700 and (b) 600 Torr. Inset shows the expanded view of the NBE emissions

influences highly on the growth rate by indirectly altering the residence time of the t-BuOH precursor and increasing/decreasing the pyrolysis efficiency. Rotation rate has little effect on the growth rate and no influence on the intrinsic defect nature. Four different DLE's have been identified, centered at 2.85, 2.53, 2.25 and 2.0 eV. Our results have been interpreted in terms of oxygen interstitial (O_i) -, zinc vacancy (V_{Zn}) - oxygen vacancy (V_O) -, and zinc vacancy cluster ((V_{Zn})$_2$) -related transitions, respectively.

5.2 Mastering of nearly strain free ZnO films on Si(111) by tuning AlN buffer thickness

As discussed in Chapter 2 – Sec. 2.1, heteroepitaxy usually results in interface often characterized by misfit dislocations, when the lattice mismatch is large. Moreover, the c-axis oriented sapphire (c-Al_2O_3) substrates are widely used for developing epitaxial ZnO thin films. Indeed, the mechanism for this epitaxial growth is characterized by domain-matching epitaxy, in which the in-plane epitaxial orientation relationship between the film and the substrate corresponds to 30° or 90° rotation of the film with respect to the substrate in the basal plane. However, for the practical applications, the integration of ZnO thin film with Si substrate is more desirable. In addition, using Si as a substrate for ZnO overgrowth with its good electrical/thermal conductivity, low cost, availability of bigger size substrates, etc. may be a good option in order to decrease ZnO film production/device costs. However, because of an oxidation of the silicon substrate by an oxygen source, as well as significant thermal expansion coefficient (56 %) and lattice (15%) mismatches between ZnO and Si(111), a direct epitaxy of ZnO on Si is challenging and often results in amorphous or polycrystalline films. Fortunately, the use of homo- or hetero- buffer layers was suggested to resolve this issue.

Aluminium nitride (AlN) buffer layers were used to achieve the preferred epitaxial growth. AlN has hexagonal wurtzite structure with lattice constants of a=3.112 Å and c=4.982 Å. The epitaxial growth of AlN thin film on Si(111) substrate occurs by the domain matching epitaxy, where integral multiples of major lattice planes of the film and the substrate match across the interface. Epitaxial ZnO thin film can be grown on AlN layer via lattice-matching epitaxy since the lattice misfit between the lattice constants of the two materials is only 4 %. Indeed, the lattice mismatch between the ZnO films and the AlN buffer can be readily modulated by varying the buffer thickness accounting for different degrees of strain relaxation in the basal plane of the buffer. Specifically for the domain matching epitaxy, the film undergoes complete strain relaxation only after reaching a critical thickness. The structural quality of the ZnO thin films was studied as a function of AlN buffer layer thickness.

Figure 5.5 summarizes the values of accumulated strain in ZnO films extracted from XRD scans as a function of AlN buffer layer thicknesses. Here, $\varepsilon_{\perp}$ denotes strain in direction perpendicular to (002) basal plane and is estimated from the changes in *c* lattice

parameter. Accordingly, $\varepsilon_{\parallel}$ represents strain component parallel to basal plane and is calculated from changes in *a* lattice parameter. One can readily observe that the relative strain along c-axis monotonously increases with increasing AlN buffer thickness and is of tensile character. On the other hand, the compressive in-plane strain $\varepsilon_{\parallel}$ initially decreases with AlN layer thickness, then abruptly peaks for ZnO film with 70 nm buffer layer and decreases again for 100 nm AlN layer thickness. The ZnO film grown on 50 nm thick AlN buffer layer is found to contain nearly $\varepsilon_{\parallel}$ strain-free ZnO film with a residual $\varepsilon_{\perp}$ strain of ~ 0.34 %.

In general, the origin of strain in a thin-film structure can be attributed to (i) lattice

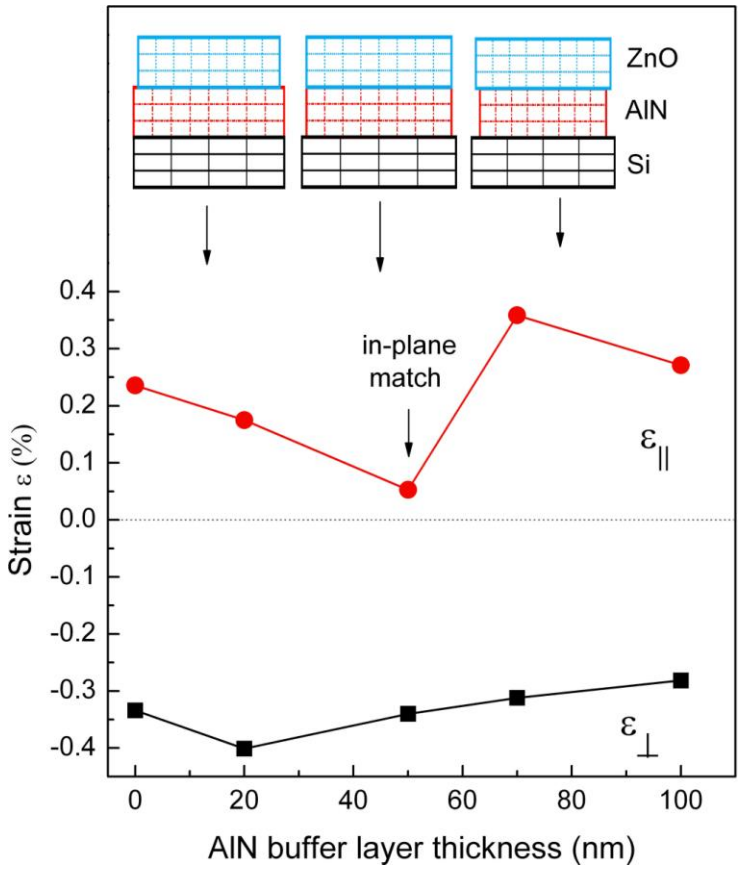

Fig. 5.5. Strain ε (%) accumulated in ZnO films as a function of AlN buffer layer thickness estimated from XRD 2θ scans. Here, $\varepsilon_{\perp}$ denotes strain in the direction perpendicular to (002) basal plane and is estimated from the changes in *c* lattice parameter; $\varepsilon_{\parallel}$ represents strain component parallel to basal plane and is calculated from the changes in *a* lattice parameter. Inset shows a simplified model illustrating the variation of lattice parameters with AlN buffer thickness.

mismatch between the film and substrate (or buffer layer); (ii) difference in the thermal expansion coefficient (TEC) of the film and substrate (or buffer layer); (iii) microstructure/defect related internal stresses. The lattice mismatch arises from the differences in lattice constants between the film and the substrate under epitaxial growth conditions. If lattice constant of a film, d_f , is smaller than that of a substrate, d_s , then a tensile stress builds up in the film; and conversely, a compressive strain occurs in the case of $d_f > d_s$. In view of the fact that the in-plane lattice parameter of ZnO is larger than that of AlN, the lattice-mismatch related strain is expected to be compressive for the ZnO/AlN/Si(111) heterostructure [123]. Furthermore, it is well known that as soon as the critical thickness is reached, the lattice-mismatch strain may be dissipated by generating dislocations. However, thermal strain can develop as the film cools down due to different TEC of the substrate (α_s) and film (α_f), exhibiting a tensile nature in the case $\alpha_f > \alpha_s$ and compressive one, if $\alpha_f < \alpha_s$. Consequently, the larger TEC in ZnO compared to that in AlN and Si implies a tensile character of thermal strain in ZnO films. The last potential cause of the strain, namely, the microstructure/defect related internal stress, originates from the trapped point/line defects, such as vacancies, interstitials, dislocations, etc. In case the vacancies have lower specific volume compared to the host lattice, then a net tensile stress prevails in the film, e.g., oxygen vacancies in ZnO films are considered to cause tensile strain [124]. A simplified model illustrating the abovementioned lattice parameter variations with AlN buffer thickness is presented in the upper part of Fig. 5.5

Chapter 6

Changing vacancy balance in ZnO by tuning synthesis between zinc/oxygen lean conditions

Changing the vacancy balance in ZnO during synthesis may strongly influence the intrinsic defect concentrations and its turn the electrical/extrinsic impurity doping properties. For example, ZnO growth in zinc/oxygen lean conditions would result in formation of V_{Zn} / V_o, a known acceptor/donor, respectively in ZnO [80]. Simultaneously, an increase in V_{Zn} may potentially result in substitution of zinc by other group-II elements, such as Cd or Mg for band gap engineering. Paper III is devoted to studies on how changing vacancy balance in MOVPE-ZnO correlates with positron annihilation spectroscopy (PAS) and deep level emission (DLE) observed in Photoluminescence (PL) spectroscopy

To realize device applications, understanding of the intrinsic defects in ZnO is important because of its potential to resolve the p-type doping problem in ZnO [125]. As discussed in Chap.4, PAS method acts as a direct tool for identifying vacancy-type in ZnO. However, PAS is predominantly employed in studying bulk ZnO, partly because of lack of high-quality material until recently and also more complicated in interpretation of the annihilation data in thin films. On the other hand, PL has been extensively applied to study vacancy-type defects in ZnO thin films, although thhe exact correlation of DLE peaks with specific intrinsic defects still remains a matter of ongoing discussions [80,126]. In this respect, a combination of PAS/PL measurements might be capable to

reveal the nature of the dominating intrinsic defects in MOVPE-ZnO films. To make such identification conclusive, it is essential to provide samples exhibiting systematic variations in the intrinsic defect balance. MOVPE-synthesis allows systematic variation of zinc/oxygen lean conditions – potentially varying the vacancy balance.

Systematic variation of vacancy balance can be achieved directly by varying the II/VI molar flow rates, indirectly by (i) varying the growth temperature (influencing the precursor decomposition percentage and (ii) varying the carrier gas flow rate (influencing the residence time thereby increasing/decreasing pyrolysis efficiency). Summarizing, variation in II/VI flow ratios may seem as a better method in order to vary the relative abundance of II versus VI reaction agents in the chamber. To begin with, PAS measurements were performed on samples grown at 385 ^{o}C for Zn/O mole fraction going into the reactor, in range of 2.42 to 0.12 and an indication of systematic variations in the S/W plot was observed, see Fig.6.1. However, similar flux dependent PAS measurements were performed on samples synthesized at different temperature. Importantly, the results did not follow flow ratio trends any longer, indicating that variation in the growth

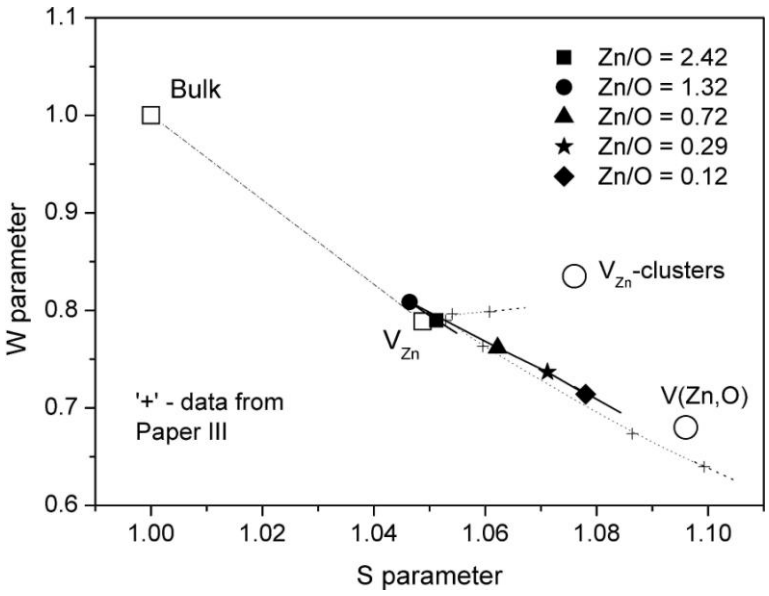

Fig.6.1 W-S plot for MOVPE-ZnO synthesized at different II/VI flux ratios at 385 ^{o}C. The reference annihilation states (bulk and V_{Zn}) are labelled by open squares. Open circles denote the (S,W) trend points revealed in previous ion implantation experiments [127,128]. The dotted line with '+' symbol is only for eye guidance representing the experimental points in Fig. 1 in Paper III.

temperature influences much stronger limitations of the abundance of the reaction agents in the chamber than the variations in flux. Indeed, as shown in Ref.122 and explored in our work, the decomposition conditions for DEZn and t-BuOH are very different at "low" (325 ^{o}C) and "high" (>385 ^{o}C) and simultaneous variation in II/VI flux ratios bring an additional uncertainty in the experiment. For example, at 325 ^{o}C, 385 ^{o}C and 420 ^{o}C the II/VI flow ratio of 2 means in practice completely different amount of actual reaction agents supplied for ZnO synthesis << 2, ~ 2, and >> 2, respectively. Hence, in the present work, providing possibility of a much broader reaction agent variations was achieved by tuning temperature, instead of molar flux ratios.

Please note that the MOVPE-ZnO samples, characterized in Paper I, were grown on c-axis oriented sapphire (c-Al_2O_3) substrates. However, for this study, the ZnO samples were fabricated on r-axis oriented sapphire (r-Al_2O_3) substrates. As a result, the observation of nanorod structures on c-Al_2O_3 substrates at high growth temperatures, is eliminated. Importantly, the growth rate of [0001] is higher than any other direction in ZnO at high growth rates. In turn, since the (0001) is normal to the r-plane, 2D film growth is obtained while employing r-Al_2O_3 substrates. The SEM surface morphologies as a function of growth temperature is presented in Fig.6.2.

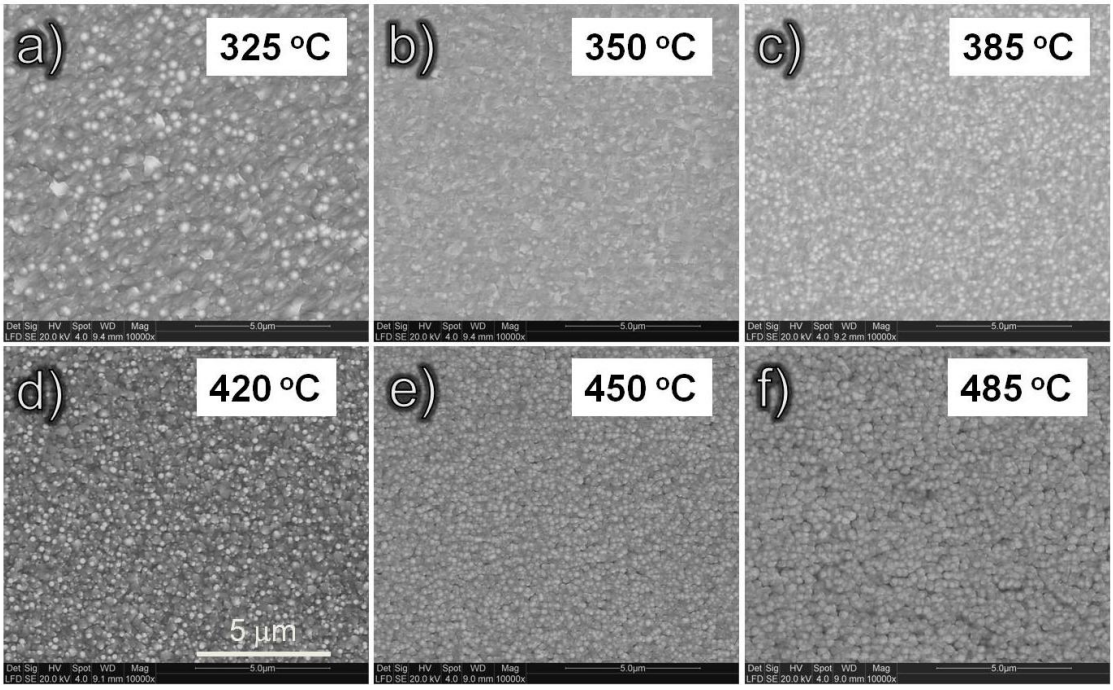

Fig.6.2 SEM images of ZnO films grown on r-Al_2O_3 as a function of temperature.

In summary, an interpretation for the nature of vacancy-type defects in MOVPE-ZnO is suggested based on systematic variation in Zn/O lean conditions during synthesis in spite of generally complicated defect balance in the samples. Specifically, the samples grown at 325 ^{o}C (most Zn-lean condition studied) are found to be enriched with vacancy clusters, similar to those observed after ion implantation and the assignment of the 2 eV emission with V_{Zn}-clusters is confirmed. Samples synthesized at high temperatures corresponding to O-lean conditions are found to contain bigger vacancy clusters responsible for damping of defect related radiative transitions in ZnO. In addition a characteristic 2.5 eV emission band is found to dominate at intermediate synthesis temperatures (350 - 385 ^{o}C) and is tentatively associated with radiative transition involving V_{Zn}.

Chapter 7

Band gap engineering and phase separation in ZnCdO

This chapter summarizes results on the ZnCdO alloy system. The results are presented in two sections. The first describes the tuning light absorption by band gap engineering in ZnCdO realized by varying the Cd content (Ref. Paper IV). The second section summarizes the extensive structural and optical analysis of the ZnCdO films (Ref. Paper V). In addition, three regimes were identified where phase separation occurs between wurtzite (w-), zincblende (zb-) and rock salt (rs-). Moreover, the interpretation of the results is backed up with a physical model.

7.1 Band gap engineering in ZnCdO

ZnO is one of the most promising materials for the fabrication of optoelectronic devices operating in the blue and UV spectral regions. Further, considering that band gap engineering is essential for fabricating heterostructures for light emitting or laser diodes, multi-junction solar cell applications, etc., ZnO can be alloyed with CdO, which has a direct band gap of 2.3 eV, and as a result, the band gap can be readily tuned from UV towards the green spectral region. However, the major concern remains the crystalline quality of ZnCdO alloys, especially with high Cd contents due to the possible coexistence

of several phases as well as crystalline misorientation, since ZnO and CdO have different crystal structures – wurtzite (w-) and rock salt (rs-), respectively.

In literature, using MOVPE, Zn/Cd content variations were predominantly studied as a function of II precursor flow rates. However, as discussed in Chapter 5, temperature plays an important role for ZnCdO fabrication in terms of precursor pyrolysis for the chosen metal organic precursors. Diethyl zinc (DEZn), Dimethyl cadmium (DMCd) and tertiary butanol (t-BuOH) were used as the zinc, cadmium and oxidizing source, respectively. In addition, Rutherford backscattering spectroscopy (RBS) and UV-Visible spectroscopy (UV-Vis) were employed to study the Cd content incorporated and the resulting band gap variations, respectively. Importantly, the results demonstrated that the Cd content decreased with increasing growth temperature from 340 to 520 ^{o}C, for fixed DEZn and DMCd flow rates. Moreover, the band gap E_g obtained from extrapolating the linear portions of the $(\alpha h\upsilon)^2$ vs. $h\upsilon$ plot (see Chapter 4 - Sec.4.3 for more details), blue-shifted from 2.69 to 3.28 eV. At low temperatures, the results are interpreted in terms of generating Zn-lean conditions and thereby more Zn vacancies, by affecting precursor pyrolysis. On the other hand, at high growth temperatures, Cd may desorb from the surface due its volatility and also the electronegativity difference between Zn and Cd may limit/hinder the incorporation efficiency.

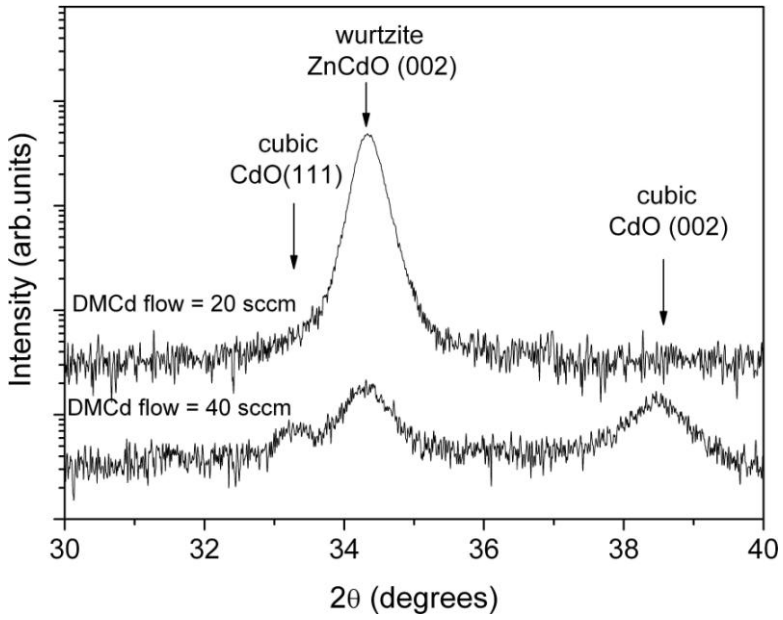

Fig.7.1 Typical examples of XRD intensities in as-grown samples fabricated at 370 ^{o}C by varying DMCd flow.

Interestingly, no phase separation between w-/rs- phase is observed in these samples based on the XRD analysis (See Fig.7.1). Specifically, with flow rates of DEZn, DMCd and t-BuOH fixed at 100, 20 and 60 sccm, respectively, we were able to incorporate 17 % of Cd in w-ZnO matrix at 340 ^{o}C. Incorporation of Cd in terms of variation of DMCd flow rates were explored with optimal growth temperature of 370 ^{o}C, as optimized from a combination between Zn lean conditions and absorption edge. Evidently, the Eg variation as a function of DMCd flow rate was more complex compared with ZnCdO fabrication as a function of growth temperature. Nevertheless, Cd content is found to increase with

Table 7.1. Optical band gaps of ZnCdO films synthesized by varying growth temperature and DMCd flow rate and the corresponding Cd contents.

DMCd flow rate (sccm)	**Growth temperature (^{o}C)**	**Estimated optical band gap (eV)**		**Cd (atomic %) from RBS analysis**
		As-grown	**Annealed**	
20	340	2.70	3.09 (2.3)	17
20	370	2.89	3.17 (2.3)	16
20	400	3.12	3.15 (2.3)	7
20	430	3.24	3.24	1.1
20	460	3.27	3.27	0.4
20	490	3.28	3.28	-
20	520	3.28	3.28	-
30	370	2.78	3.16 (2.3)	32
40	370	2.82	3.15 (2.3)	48
50	370	2.80	3.15 (2.3)	53
60	370	2.79	3.15 (2.3)	54
70	370	2.77	3.15 (2.3)	60

increasing DMCd flow rate as determined by RBS. However, Eg exhibited initial red shifts and consequently blue-shits at higher DMCd flow rates. The results are interpreted in terms of phase separation, which is in good agreement with the simultaneous observation of both w- and rs- reflections by XRD analysis as shown in Fig.7.1.

Moreover, post-fabrication anneals are employed in order to deduce w-ZnCdO compositional stability limits. The $(\alpha h\upsilon)^2$ vs. $h\upsilon$ plot of ZnCdO samples with Cd $\geq$ 7 % demonstrate at least two-step slopes on the absorption edge, implying the presence of different phases in the samples. Annealing of samples (except with Cd content of 17 % grown at 340 ^{o}C) resulted in appearance of a 3.15 eV optical absorption edge in addition to a direct ~ 2.3 eV absorption threshold characteristic of pure CdO, which is in agreement with XRD observations. The results are summarized in Table 7.1. In conclusion, the limits of growth temperature and flow rate for synthesis of a single phase wurtzite ZnCdO by MOVPE have been determined providing tunability of the band gap down to 2.70 eV at 17 % of Cd incorporation. The observed optical absorption edges at ~ 2.3 and ~ 3.15 eV are attributed to direct band gaps of cubic CdO and thermodynamically stable wurtzite ZnCdO, respectively.

7.2 Phase separation in ZnCdO

As already mentioned in Sec.7.1, in spite of similar elemental chemical character of Zn and Cd, their ternary oxide formation is greatly affected by the appearance of different crystalline structures apparently becoming stable in different compositional ranges. Importantly, the solid solubility limit of Cd in w-ZnO is reported to vary between 5 and 69 %. Moreover, Cd when oxidized adopts octahedral coordination in the cubic B1 rs-structure, while ZnO favors tetrahedral coordination in the hexagonal B4 wurtzite structure. Gruber et.al [70], have reported single phase w-ZnCdO containing 5 % Cd and fabricated on c-Al2O3 and have observed domains exhibiting lower/high cathodeluminescence contrasts without deviations in chemical Zn/Cd contents. This could be possibly interpreted in terms of other metastable phases, specifically, co-existence of zb-ZnCdO exhibiting local fourfold coordination similar to that in w-matrix (See Chapter 2 – Sec.2.1 for more details). Moreover, the cohesive energy of zb-ZnO (-7.679 eV) is

very close to that in w-ZnO (-7.692 eV), and exhibiting a band gap difference of ~ 80 meV.

Interestingly, theoretical calculations by Zhu et.al [129], have predicted stabilization of zb-ZnCdO at moderate Cd content as well as a transition to the rs-matrix occurring for Cd content > 62 %. Please note that co-existence of the zb- and w- phases was observed in pure ZnO powder experiments and the phase ratio was found to vary with temperature [130]. In addition, to the characterization techniques employed in Sec.7.2, photoluminescence (PL) was also employed to understand the phase separation in ZnCdO. Importantly, the variations in PL signatures also followed similar trends in correlation with XRD, RBS and UV-Vis transmission analysis. Based on the PL and XRD interpretations, three characteristic compositional regions were identified, as depicted in Fig. 7.2. Firstly, alloying w-ZnO with $\leq$ 2 % of Cd results in a single phase w-ZnCdO. Secondly, for the range of 7 - 17 % of Cd, w- and zb-ZnCdO phases coexist.

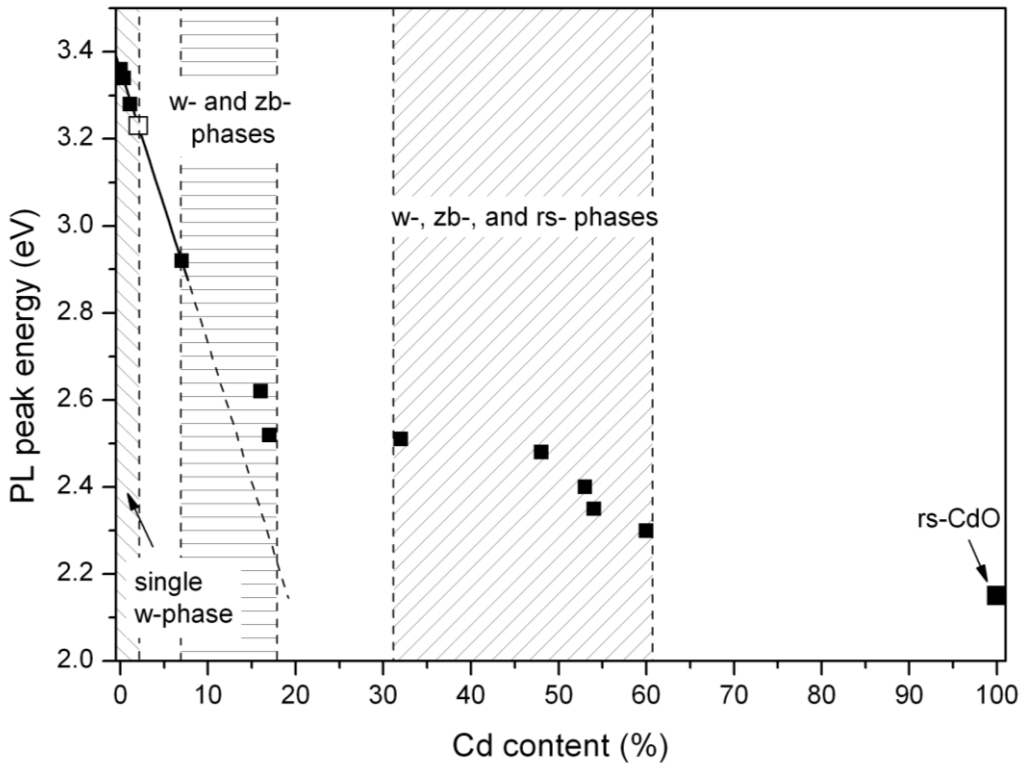

Fig. 7.2 Dominating NBE PL signatures as a function of Cd content (filled squares) in correlation with corresponding phase stability trends illustrated by dashed lines. The continuous line is a linear fit to the w-ZnCdO related emissions. An open square represents a characteristic w-ZnCdO signal found after annealing in samples having $\geq$ 7 % of Cd.

Further, samples having 17 – 60 % of Cd reveal a mixture of w-, zb- and rs-phases in different proportions. Moreover, characteristic PL signatures identified at 2.54 and 2.31 eV were attributed to zb-ZnCdO and rs-CdO, while the band gap variation in w-$Zn_{1-x}Cd_xO$ is given by (3.36 – 0.063x) as determined at 10K.

Firstly, the mechanisms for the structural evolution and PL are explained in terms of the ionicity of the crystals. The relative stability between zb- and w- structures is understood by considering the stacking fault (SF) energy and the charge redistribution. As discussed in Chapter 2 – Sec. 2.1, zb- phase exhibits a repeated stacking sequence of Aa-Bb-Cc-Aa, while w-phase is characterized by Aa-Bb-Aa stacking sequence. Moreover, in w-structure, two-third of the neighbours along the c-axis are much closer than any other similar pairs of neighbours in w- and zb- structures and also, the relative energies of these two crystal structures arises from the difference in the third nearest-neighbour atom spacing, which is shorter for wz- than the zb-structure. In addition, the Madelung constant (α), a parameter describing electrostatic potential of a single ion in a crystal with the ions approximated by point charges, also accounts for the stability between zb-/w- equilibrium considering the charge re-distribution. The changes in r affects α_w in accordance with $\alpha_w = 1.6406 - 0.0207\ (r/1.633-1)$ [131] (note, for w-ZnO, r = (*c*/*a*) = 1.602 results in $\alpha_{ZnO} = 1.6410$).

Indeed, the relative energies of these configurations determine the SF energy. The change in SF energy may be divided into two terms: the bond distortion energy ΔE_b and the Coulomb energy ΔE_c, dominating in low and high ionicity crystals, respectively. Accounting for a high ionicity (meaning that Coulomb energy dominates), the w-structure appears to be favourable comparing to the zb-matrix in ZnO because of a shorter distance to the third nearest unlike neighbour ions [132]. Similarly to the consideration in terms of α, when the lattice is contracted, ΔE_c decrease because of shorter interatomic distances meaning the stabilization of the w- versus zb-structure in ZnO. In contrast, a positive strain applied along all crystallographic direction (following random Cd incorporation in the Zn-sublattice), might result in an increase of ΔE_c enhancing probability of the zb-phase segregation. Moreover, the charge re-distribution is also influenced by strain given by the relation: $e^* = e_o^*(1+\varepsilon)^s$, where e* and e_o* are the effective charges with and without applied strain, respectively and s is a charge redistribution index (s = -3.9 in

ZnO) [133]. Thus, applying a positive strain would decrease the e* values when introducing Cd in w-ZnO contributing to a decrease in α and stabilizing zb-phase.

Considering the ZnCdO fabricated as a function of growth temperature, the lattice parameter *c*, is found to increase with increasing Cd content from XRD structural analysis. The influence of variations in lattice parameter on Madelung constant and effective charge re-distribution with zb-/w- structure stability is summarized in Table 7.2.

Table 7.2 Variations in Madelung constant, SF energy and Charge redistribution stabilizing w-/zb- structures as a function of lattice parameter *c*, with constant *a*. Please note that variations in lattice parameter *a*, also hold good for SF energy and charge redistribution, while α scales with *c*/*a* ratio.

r = (c/a), with constant *a*	**Madelung constant**		**Stacking fault energy**		**Charge redistribution index**	
	α_w = 1.6406 – 0.0207 (r/1.633-1)	**w-/zb-stability**	**f(ΔE_c) for high iconicity crystals**	**w-/zb-stability**	$e^* = e_o^*(1+\varepsilon)^s$, **s = -ve**	**w-/zb-stability**
r = 1.6333	1.6406 (ideal)	w-structure	ideal	w-structure	ideal	w-structure
r_1 (c ↓) < 1.6333	$\alpha_{w1} > \alpha_{w\text{-ideal}}$	w-structure	↓	w-structure	ε = -ve, e*↑, α ↑	w-structure
r_2 (c ↑) > 1.6333	$\alpha_{w2} < \alpha_{w\text{-ideal}}$	zb-structure	↑	zb-structure	ε = +ve, e* ↓, α ↓	zb-structure

Chapter 8

Concluding remarks and suggestions for future work

The research described in this thesis has resulted in several discoveries in the increasingly growing field of ZnO. More specifically, it provides a new understanding of phase separation in ZnCdO alloy system and also explains the changing vacancy balance in ZnO by tuning synthesis between zinc/oxygen lean conditions.

The nature of dominating vacancy type defects during MOVPE-ZnO synthesis is found to vary systematically on the variation in Zn/O lean conditions regardless of the initial defect balance in the samples. Systematic variations in Zn/O lean conditions by employing growth temperature are found to be enriched with Zn vacancy clusters under most Zn-lean conditions. We have identified two optical signatures of intrinsic defects. The emission dominating at ~ 2.0 eV for most Zn-lean conditions was related to V_{Zn}-clusters, while the other dominating in the intermediate temperatures at ~ 2.53 eV is associated with radiative transition involving V_{Zn} by correlating with PAS results. Samples synthesized at higher temperatures corresponding to O-lean conditions are found to contain bigger vacancy clusters responsible for damping of defect related radiative luminescence in ZnO. Alternatively, varying II/VI molar ratio for oxygen-rich conditions, the DLB signature at ~ 2.85 eV becomes more prominent with decreasing II/VI ratio and are associated with generation of O_i.

It has been demonstrated that by alloying w-ZnO with rs-CdO, the band gap can be tuned down to 2.3 eV for maximum Cd content of 60 %. The phenomenon of phase separation in ZnCdO was investigated and the analysis has revealed presence of a new, conventionally not considered phase of zb-ZnCdO, in addition to commonly discussed w- and rs-phases. Interestingly enough, three discrete regimes were identified, where the phase separation occurs between the w-, zb- and rs-phases. More importantly, a detailed analysis of the diffraction and photoluminescence data revealed that w-single phase stability range is likely to be as narrow as 0 - 2 % Cd while samples containing 7- 17 % of Cd exhibit a mixture of w- and zb-phases. Moreover, high Cd content (32 – 60 %) ZnCdO alloys realized by supplying more of Cd precursor utilizing Zn-lean growth conditions, however, resulted in a mixture of w-, zb-, and rs-phases. Characteristic PL signatures at 2.54 and 2.31 eV were attributed to zb-ZnCdO and rs-CdO while the band gap variation in w-$Zn_{1-x}Cd_xO$ was established as 3.36 – 0.063x for 10K. A model was proposed to understand the phase separation in terms of corresponding changes in charge distribution and reduced stacking fault energy.

It should be noted that nearly in-plane strain free ZnO films on Si(111) could be successfully fabricated by tuning AlN buffer layer thickness. Consequently, this kind of high-quality samples with reproducible properties would facilitate realization of potential device applications, however, more research is required to solve some of the issues related to residual out-plane strain which is not taken into consideration.

As shown in this thesis, it is possible to tune the vacancy balance in MOVPE-ZnO and in turn, to increase the incorporation efficiency of the impurity dopants on the desired lattice sites. It has been demonstrated, for instance, that more Cd % can be incorporated in w-ZnO matrix at most Zn-lean conditions. This fact should be pursued further with regard to engineering of p-type material by allowing acceptors to settle in V_{Zn} sites. In addition, electrical measurement may be readily applied to the existing samples, on the actuality that the electrical contact will work. Overall, accounting for the maturity of the sample synthesis it may be timely to launch project on the device realization using components developed in the course of the present thesis.

Furthermore, upon successful demonstration of tuning band gap down to 2.3 eV by alloying ZnO with CdO, it will be interesting to explore heterostructures with variation in band gap along the axial direction by varying the Cd content which may offer many

beneficial effects. First, enhanced light absorption is expected because of the broad range of band gaps within the material. Additionally, the axially-graded band gap produces a spatially-controlled absorption of solar irradiation. Finally, the heterostructure will set up an electric field across the thickness once used as an solar absorber, which will enhance the charge transport. This widens the application range of these heterostructures, for instance, by integrating in solar and photo electrochemical cells, etc.

In present thesis, we demonstrate the fabrication of the nanorod-like structures at high temperatures. Employing high temperature synthesis conditions, it will be interesting to explore catalyst-free nanowiring of ZnO, where new properties may be expected by tuning the intrinsic defect balance in the material. It will be also worth to study nanostructuring of the heterostructures with variation in band gap along the length. Further, the crystalline quality of nanowires might play a decisive role for the carrier transport properties. This may be a significant advantage, especially when the nanowire length exceeds the diffusion length of the charge carriers.

Bibliography

1. M. J. Kelly, *Adv. Mater.*, **9**, 857 (1997).
2. A. Fowler, *Physics Today*, **50**, 50 (1997).
3. R. Triboulet and J. Perriere, *Prog. Cryst. Growth and Charac. Mater.*, **47**, 65 (2003).
4. J. A. Edmond, H. S. Kang and C. H. Carter Jr., *Physica B* **185**, 453 (1993).
5. S. Nakamura, T. Mukai and M. Senoh, *Jpn. J. Appl. Phys.* **30**, L1998 (1991).
6. T. Minami, *Semicond. Sci. Technol.* **20**, S35 (2005).
7. K. C. Kim, M. C. Schmidt, H. Sato, F. Wu, N. Fellows, M. Saito, K. Fujito, J. S. Speck, S. Nakamura and S. P. DenBaars, *Phys. Status Solidi (RRL)* **1**, 125 (2007).
8. S. Nakamura, T. Mukai, M. Senoh and N. Iwasa, *Jpn. J. Appl. Phys.* **31**, L139 (1992).
9. S. Nakamura, M. Senoh and T. Mukai, *Jpn. J. Appl. Phys.* **32**, L8 (1993).
10. C. G. Granqvist, *Thin Solid Films* **193-194**, 730 (1990) and references therein.
11. T. Minami, H. Nanto and S. Takata, *Jpn. J. Appl. Phys.* **23**, L280 (1984).
12. Y. R. Ryu, T. S. Lee, J. A. Lubguban, A. B. Corman, H. W. White, J. H. Leem, M. S. Han, Y. S. Park, C. J. Youn and W. J. Kim, *Appl. Phys. Lett.* **88**, 052103 (2006).
13. A. Ohtomo, M. Kawasaki, T. Koida, K. Masubuchi, H. Koinuma, Y. Sakurai, Y. Yoshida, T. Yasuda and Y. Segawa, *Appl. Phys. Lett.* **72**, 2466 (1998).
14. T. Makino, Y. Segawa, M. Kawasaki, A. Ohtomo, R. Shiroki, K. Tamura, T. Yasuda and H. Koinuma, *Appl. Phys. Lett.* **78**, 1237 (2001).
15. D. M. Bagnall, Y. F. Chen, Z. Zhu, T. Yao, S. Koyama, M. Y. Shen and T. Goto, *Appl. Phys. Lett.* **70**, 2230 (1997).
16. Y. Segawa, A. Ohtomo, M. Kawasaki, H. Koinuma, Z. K. Tang, P. Yu and G. K. L. Wong, *Phys. Status Solidi B* **202**, 669 (1997).
17. H. D. Li, S. F. Yu, A. P. Abiyasa, C. Yuen, S. P. Lau, H. Y. Yang and E. S. P. Leong, *Appl. Phys. Lett.* **86**, 261111 (2005).

18. H. Cao, Y. G. Zhao, H. C. Ong, S. T. Ho, J. Y. Dai, J. Y. Wu and R. P. H. Chang, *Appl. Phys. Lett.* **73**, 3656 (1998).
19. A. Ohtomo, K. Tamura, M. Kawasaki, T. Makino, Y. Segawa, Z. K. Tang, G. Wong, Y. Matsumoto and H. Koinuma, *Appl. Phys. Lett.* **77**, 2204 (2000).
20. M. H. Huang, S. Mao, H. Feick, H. Yan, Y. Wu, H. Kind, E. Weber, R. Russo and P. Yang, *Science* **8**, 1897 (2001).
21. L. M. Levinson and H. R. Philipp, *Am. Ceram. Soc. Bull.* **65**, 639 (1986).
22. J. D. Albrecht, P. P. Ruden, S. Limpijumnong, W. R. L. Lambrecht and K. F. Brennan, *J. Appl. Phys.* **86**, 6864 (1999).
23. D. C. Look, D. C. Reynolds, J. R. Sizelove, R. L. Jones, C. W. Litton, G. Cantwell and W. C. Harsch, *Solid. State. Commun*. **105**, 399 (1998).
24. D. C. Look, D. C. Reynolds, J. W. Hemsky, R. L. Jones and J. R. Sizelove, *Appl. Phys. Lett.* **75**, 811 (1999).
25. H. J. Queisser and E. E. Haller, *Science* **281**, 945 (1998).
26. T. Yao, S. –K. Hong (Eds.), *"Oxide and Nitride Semiconductors: Processing, Properties and Applications"*, (T. Hanada – Chapter 1, Springer, 2009).
27. Ü. Özgür, Ya. I. Alivov, C. Liu, A. Teke, M. Reshchikov, S. Doğan, V. Avrutin, S.-J. Cho, and H. Morkoç, *J. Appl. Phys. Rev.*, **98**, 04130 (2005).
28. J. E. Jaffe and A. C. Hess, *Phys. Rev. B*, **48**, 7903 (1993).
29. M. Catti, Y. Noel, and R. Dovesi, *J. Phys. Chem. Solids*, **64**, 2183 (2003).
30. I.Vurgaftman, and J.R. Meyer, *J. Appl. Phys.*, **94**, 3675 (2003)
31. D. A. Porter and K. E. Easterling, "*Phase Transformation in metals and alloys, second edition"*, (Nelson Thornes, 1992, page 143).
32. T. Matsuoka, N. Yoshimoto, T. Sasaki and A. Katsui, *J. Electron. Mater*. **21**, 157 (1992).
33. A. Tsukazaki, A. Ohtomo, M. Kawasaki, T. Makino, C. H. Chia, Y. Segawa and H. Koinuma, *Appl. Phys. Lett.* **84**, 3858 (2004).
34. Stavola M (ed), "*Identification of Defects in Semiconductors, Semiconductors and Semimetals",* Vol 51B (San Diego: Academic, 1999).
35. S.E. Harrison, *Phys. Rev.* **93** 52 (1954).
36. A.R. Hutson, *Phys. Rev.* **108** 222 (1957).
37. D.G. Thomas, *J. Phys. Chem. Solids*, **3,** 229 (1957).
38. F.A. Kroger F A, *"The Chemistry of Imperfect Crystals",* (Amsterdam: North-Holland, 1974)

39. A.F. Kohan, G. Ceder, D. Morgan and C.G. van de Walle, *Phys. Rev.* B, **61**, 15019 (2000).
40. A. Janotti and C.G. van deWalle, *Phys. Rev.* B, **75**, 165202 (2007).
41. L.S. Vlasenko and G.D.Watkins, *Phys. Rev.* B, **72**, 035203 (2005).
42. C.G. van de Walle, *Phys. Rev. Lett.* **85**, 1012 (2000)
43. D.M.. Hofmann , A. Hofstaetter, F. Leiter, H. Zhou, F. Henecker, B.K. Meyer, S.B. Orlinskii, J. Schmidt and P.G. Baranov, *Phys. Rev. Lett.*, **88**, 045504 (2002)
44. M.D. McCluskey, S.J. Jokela, K.K. Zhuravlev , P.J. Simpson and K.G. Lynn, *Appl. Phys. Lett.*, **81**, 3807 (2002)
45. M.G. Wardle, J.P. Goss and P.R.Briddon, *Phys. Rev. Lett.*, **96**, 205504 (2006)
46. M.A. Reshchikov, H. Morkoc, B. Nemeth, J. Nause, J. Xie, B. Hertog and A. Osinsky, *Physica B: Condensed Matter*, **401-402**, 358 (2007).
47. D.C. Reynolds, D.C. Look, B. Jogai, H. Morkoc, *Sol. Stat. Comm.*, **101**, 643 (1997).
48. M. Liu, A.H. Kiati, P. Mascher, *J. Lumin.*, **54**, 35 (1992).
49. P.H. Kassai, *Phys. Rev.*, **130**, 989 (1963).
50. S. Yamauchi, Y. Goto, T. Hariu, *J. Crystal Growth*, **260**, 1 (2004).
51. R. Dingle, *Phys. Rev. Lett.* **23**, 579 (1969).
52. Q.X. Zhao, P. Klason, M. Willander, H.M. Zhong, W. Lu, J.H. Yang, *Appl. Phys. Lett.*, **87**, 211912 (2005)
53. M. Willander, O. Nur, J. R. Sadaf, M. I. Qadir, S. Zaman, A. Zainelabdin, N. Bano and I. Hussain, *Materials*, **3**, 2643 (2010).
54. X.L. Wu, G.G. Siu, C.L. Fu, and H.C. Ong, *Appl. Phys. Lett.*, **78**, 2285 (2001).
55. L.E. Greene, M. Law, J. Goldberger, F. Kim, J. Johnson, Y. Zhang, R.J. Saykally, P. Yang, *Angew. Chem. Int. Ed.*, **42**, 3031 (2003).
56. M. Gomi, N. Oohira, K. Ozaki, M. Koyano, *Jpn. J. Appl. Phys.*,, **42**, 481 (2003).
57. A.B. Djurisic, Y.H. Leung, K.H. Tam, Y.F. Hsu, L. Ding, W.K. Ge, C. Zhong, K.S. Wong, W.K Chan, H.L. Tam, K.W. Cheah, W.M. Kwok, D.L. Phillips, *Nanotechnology*,, **18**, 095702 (2007).
58. A.B. Djurisic, Y.H. Leung, K.H. Tam, L. Ding, W.K. Ge, H.Y. Chen and S. Gwo, *Appl. Phys. Lett.*, **88**, 103107 (2006).
59. S.A.M. Lima, F.A. Sigoli, M. Jafelicci and M.R. Davolos, *Int. J. Inorg. Mater.*, **3**, 749–754 (2001).
60. B. Lin, Z. Fu and Y. Jia, *Appl. Phys. Lett.*, **79**, 943 (2001).

61. V. Nikitenko, *Optical and Spectroscopy of Point Defects in Zinc Oxide*, (Springer: Dordrecht, The Netherland, 2005; p. 69).
62. C.G. van de Walle, *Phys. Rev. Lett.*, **85**, 1012 (2000).
63. O.F. Schirmer and D. Zwingel, *Sol. Stat. Commun.*, **8**, 1559 (1970).
64. A. L. Allenic, *"Structural, Electrical and Optical properties of p-type ZnO Epitaxial films"*, PhD Thesis, The University of Michigan, 2008.
65. D. Hull and D. J. Bacon, *Introduction to dislocations, fourth edition*, (Butterworth Heinemann, 2001).
66. C. Stampfl and C. G. Van de Walle, *Phys. Rev. B*, **57**, R15052 (1998).
67. T. Gruber, C. Kirchner, R. Kling, F. Reuss, and A. Waag, *Appl. Phys. Lett.*, **84**, 5359 (2004).
68. T. Makino, C. H. Chia, Nguen T. Tuan, Y. Segawa, M. Kawasaki, A. Ohtomo, K. Tamura, and H. Koinuma, *Appl. Phys. Lett.*, **77**, 1632 (2000).
69. D. W. Ma, Z. Z. Ye, and L. L. Chen, *Phys. Stat. Sol. (a)*, **201**, 2929 (2004).
70. T. Gruber, C. Kirchner, R. Kling, F. Reuss, A. Waag, F. Bertram, D. Forster, J. Christen, and M. Schreck, *Appl. Phys. Lett.*, **83**, 3290 (2003).
71. J. A. Van Vechten and T. K. Bergstresser, *Phys. Rev. B*, **1**, 3351 (1970).
72. E. R. Segnit and A. E. Holland, *J. Am. Ceram. Soc.*, **48**, 412 (1965).
73. Y. R. Ryu, T. S. Lee, and H. W. White, *J. Cryst. Growth*, **261**, 502 (2004).
74. R.D. Shannon, *Acta Cryst.*, **32**, 751 (1976).
75. J.J. Brown and F.A. Hummel, *J. Electro. Soc.*, **111**, 1052 (1964).
76. .A. Bashkirov and N.V. Kornilova, *Inorg. Mater.*, **18**, 1587 (1982).
77. A. Whitaker and A.D. Channell, *J. Mater. Sci.*, **28**, 2489 (1993).
78. J. Ishihara, A. Nakamura, S. Shigemori, T. Aoki, and J. Temmyo, *Appl. Phys. Lett.*, **89**, 091914 (2006)
79. J.-J. Chen, F. Ren, Y. Li, D.P. Norton, S.J. Pearton, A. Osinsky, J.W. Dong, P.P. Chow, J.F. Weaver, *Appl. Phys. Lett.*, **87**, 192106 (2005)
80. A. Janotti and C.G. Van de Walle, *Rep. Prog. Phys.*, **72**, 126501 (2009).
81. E.V. Monakhov, A. Yu. Kuznetsov and B.G. Svensson, *J. Phys. D: Appl. Phys.*, **42**, 153001 (2009).
82. S.J. Pearton, W.T. Lim, J.S. Wright, L.C.Tien, H.S.Kim, D.P. Norton, H.T. Wang, B.S. Kang, F. Ren, J. Jun, J. Lin and O. Osinsky, *J. Electronic Mater.*, **37**, 1426 (2008).
83. H. Manasevit, *J. Cryst. Growth*, **55**, 1 (1981).

84. S. Hersee and J. Duchemin, *Ann. Rev. Mater. Sci.,* **12**, 65 (1982).
85. G. B. Stringfellow, *Organometallic Vapor-Phase Epitaxy*, (New York: Academic, 1989).
86. H. Manasevit and K. Hess, *J. Electrochem. Soc.*, **126**, 2031 (1979).
87. C.K. Lau, S.K. Tiku, K.M. Lakin, *J. Electrochem. Soc.*, **127**, 1843 (1980).
88. M. Ohring, *Materials Science of Thin Films, Deposition and Structure*, (San Diego, Academic, 2002).
89. H. A. Wriedt, *Bull. Alloy Phase Diagrams*, **8** ,166 (1987).
90. Y. Mori and N. Watanabe, *J. Appl. Phys.,* **52**, 2792 (1981).
91. C. Mitchell, E. Michael, and J. Han, *J. Cryst. Growth*, **222**, 144 (2001).
92. A. McGinnis, D. Thomson, R. Davis, E. Chen, A. Michel, and H. Lamb, *Surface Science*, **494**, 28 (2001).
93. S. Agouram, J. Zuniga perez, and V. Munoz-sanjose, *Appl. Phys. A,* **88**, 83 (2007).
94. A.P. Roth and D.F. Williams, *J. Appl. Phys.,* **52**, 6685 (1981).
95. W. Kern and R.C. Heim, *J. Electrochem. Soc.,* **117**, 562 (1970).
96. C.K. Lau, S.K. Tiku and K.M.Lakin, *J. Electrochem. Soc.,* **127**, 1843 (1980).
97. F.T.J. Smith, *Appl. Phys. Lett.,* **43**, 1108 (1983).
98. C.R. Gorla, N.W. Emanetoglu, S. Liang, W.E. Mayo and Y.J. Lu, *J. Appl. Phys.,* **85**, 2595 (1999).
99. Y. Kashiwaba, K. Haga, H. Watanabe, B.P. Zhang, Y. Segawa and K. Wakatsuki, *Phys. Status Solidi b*, **229**, 921 (2002).
100. T. Yasuda and Y. Segawa, *Phys. Status Solidi b*, **241** 676 (2004)
101. T. Gruber, C. Kirchner and A. Waag, *Phys. Status Solidi b*, **229**, 841 (2002).
102. T. Gruber, C. Kirchner, K. Thonke, R. Sauer and A. Waag, *Phys. Status Solidi a,* **192**, 166 (2002).
103. V. Sallet, J.F. Rommeluere, A. Lusson, A. Riviere, S. Fusil, O. Gorochov and R. Triboulet, *Phys. Status Solidi b*, **229**, 903 (2002).
104. C. Kirchner, T. Gruber, F. Reuss, K. Thonke, A. Waag, C. Giessen and M. Heuken, *J. Cryst. Growth*, **248**, 20 (2003)
105. K. Ogata, T. Kawanishi, K. Sakurai, S-W. Kim, K. Maejima, S. Fujita and S. Fujita, *Phys. Status Solidi b*, **229**, 915 (2002)
106. T.P. Smith, H. McLean, D.J. Smith and R.F. Davis, *J. Cryst. Growth*, **265**, 390 (2004).

107. S. Perkowitz, *Optical characterization of semiconductors; infrared, Raman and photoluminescence spectroscopy*, (Academic Press, 1991).
108. P. T. Landsberg, *Recombination in semiconductors*, (Cambridge University Press, 1991).
109. G. H. Wannier, *Phys. Rev.*, **52**, 191 (1937).
110. B. K. Meyer, H. Alves, D. M. Hoffman, W. Kriegseis, D. Forster, F. Bertram, J. Christen, A. Hoffman, M. Strassburg, M. Dworzak, U. Haboeck and A. V. Rodina, *Phys. Status Solidi B*, **241**, 231 (2004).
111. H. Barry Bebb and E. W. Williams, *Photoluminescence I: Theory, in: Semiconductors and Semimetals*, (Volume 8, Academic Press, 1972).
112. C. F. Klingshirn, *Semiconductor optics*, (Springer, Berlin, 1995).
113. Y. P. Varshni, *Physica*, **34**, 149 (1967).
114. T. Schmidt, *Phys. Rev. B*, **45**, 8989 (1992).
115. A. Vehanen (ed.), *Slow Positrons in Surface Science, Proceedings of the International Workshop, Pajulathi, Finland*, (Helsinki University of Technology Report No. 135, 1984).
116. P.J. Schultz and K.G. Lynn, *Rev. Mod. Phys.*, **60**, 701 (1988).
117. W. Trifthauser and G. Kogel, *Phys. Rev. Lett.*, **48**, 1741 (1982).
118. P.J. Schultz, G.R. Massoumi, and P.J. Simpson, *Positron Beams for Solids and Surfaces, Proceedings of the Fourth International Workshop on Slow- Positron Beam Techniques for Solids and Surfaces*, (American Institute of Physics, New York, 1990).
119. W K Chu, J W Mayer and M A Nicolet, *Backscattering Spectrometry*, (Academic Press. New York, 1978).
120. J.H. Hoh, R. Lal, S.A. John, J.P. Revel, and M.F. Arnsdorf, *Science*, **253**, 1405 (1991).
121. P.K. Hansma, J.P. Cleveland, M. Radmacher, D.A. Walters, P.E. Hillner, M. Bezanilla, M. Fritz, D. Vie, H.G. Hansma, C.B. Prater, J. Massie, L. Fukunaga, J. Gurley, and V. Elings, *Appl. Phys. Lett.*, **64**, 1738 (1994).
122. C. Thiandoume, V. Sallet, R. Triboulet, and O. Gorochov, *J. Cryst. Growth*, **311**, 1411 (2009).
123. A. Tiwari, M. Park, C. Jin, and H. Wang, *J. Mater. Res.*, **17**, 2480 (2002).
124. A. Janotti and C.G. Van de Walle, *Appl. Phys. Lett.*, **87**, 122102 (2005).
125. D.C. Look and B. Claflin, *Phys. Stat. Sol. (b)*, **241**, 624 (2004).

126. Y. Dong, F. Tuomisto, B.G. Svensson, A. Yu. Kuznetsov, and L. J. Brillson, *Phy. Rev. B*, **81**, 081201 (2010).
127. A. Zubiaga, F. Tuomisto, V. A. Coleman, H. H. Tan, C. Jagadish, K. Koike, S. Sasa, M. Inoue, and M. Yano, *Phys. Rev. B*, **78**, 035125 (2008).
128. T. M. Borseth, F. Tuomisto, J. S. Christensen, W. Skorupa, E. V. Monakhov, B. G. Svensson, and A. Yu. Kuznetsov, *Phys. Rev. B*, **74**, 161202(R) (2006).
129. Y.Z. Zhu, G.D. Chen, H. Ye, A. Walsh, C.Y. Moon and S-H Wei, *Phys. Rev. B,* **77**, 245209 (2008).
130. L.P. Snedeker, A.S. Risbud, O. Masala, J.P. Zhang, R. Seshadri, *Solid State Sci.*, **7**, 1500 (2005)
131. Y. Sakamoto, *J. Chem. Phys.*, **28**, 164 (1958).
132. P. Lawaetz, *Phys. Rev. B*, **5**, 4039 (1972).
133. S. Takeuchi, K. Suzuki and K. Maeda, *Philos. Mag. A,* **50**, 171 (1984).

ZnO growth by vector flow epitaxy

V. Venkatachalapathy, A. Galeckas and A. Yu. Kuznetsov

To be submitted to Journal of Crystal Growth

I

Engineering of nearly strain-free ZnO films on Si(111) by tuning AlN buffer thickness

V. Venkatachalapathy, A. Galeckas, I-H Lee and A. Yu. Kuznetsov

Submitted to Thin Solid Films

II

Engineering of nearly strain-free ZnO films on Si(111) by tuning AlN buffer thickness

Vishnukanthan Venkatachalapathy[a,*], Augustinas Galeckas[a], In-Hwan Lee[b] and Andrej Yu. Kuznetsov[a]

[a]*Department of Physics / Centre for Materials Science and Nanotechnology, University of Oslo, P.O. Box 1048 Blindern, N-0316 Oslo, Norway*

[b]*School of Advanced Materials Engineering, Research Centre for Advanced Materials Development (RCAMD), Chonbuk National University, Jeonju 561-756, Korea*

ZnO properties were investigated as a function of AlN buffer layer thickness (0 -100 nm) in ZnO/AlN/Si(111) structures grown by metal organic vapor phase epitaxy. A significant improvement of ZnO film crystallinity by tuning AlN buffer thickness was confirmed by x-ray diffraction, topography and photoluminescence measurements. An optimal AlN buffer layer thickness of 50 nm is defined, which allows for growth of nearly strain-free ZnO films. The presence of free excitons at 10K suggests high crystal quality for all ZnO samples grown on AlN/Si(111) templates. The intensities of neutral and ionized donor bound exciton lines are found to correlate with the in-plane and out-of-plane strain in the films, respectively.

Keywords: ZnO, Metal organic vapor phase epitaxy, strain relaxation, Photoluminescence, AlN buffer.

1. Introduction

Zinc oxide (ZnO) attracts significant attention because of its unique physical properties, offering a variety of multi-functional applications in optoelectronics, transparent electrodes, solar cells, sensors, etc. [**1-3**] Sapphire is widely used in form of substrates when fabricating high quality ZnO epilayers for fundamental studies and device applications. However, sapphire is a hard, electrically insulating and relatively low thermal conducting material, which would introduce a great deal of complexity and lift the cost of fabrication process. Using silicon as a substrate for ZnO overgrowth with its good electrical/thermal conductivity, low cost, availability of bigger size substrates, etc. may be a good option in order to decrease ZnO film production/device costs. However, because of an oxidation of the silicon substrate by an oxygen source, as well as significant thermal expansion coefficient (56 %) and lattice (15%) mismatches between ZnO and Si(111), a direct epitaxy of ZnO on Si is challenging and often results in amorphous or polycrystalline films. Fortunately, the use of homo- or hetero- buffer layers was suggested to resolve this issue. In the last few years, various buffer layers have been investigated, including elemental metal films (e.g. Zn, Al, Ti, etc.) [**4-6**] as well as different compounds like zinc sulphide (ZnS), aluminium nitride (AlN), gallium nitride (GaN), silicon carbide (3C-SiC), aluminium oxide (γ-Al_2O_3), magnesium oxide / titanium nitride (MgO/TiN), etc. [**7-12**]. Among these materials, AlN has a hexagonal wurtzite (w-) structure with lattice parameters of a = 3.11 Å and c = 4.98 Å, similar to that of ZnO (a = 3.25 Å and c = 5.20 Å). Moreover, the thermal expansion coefficient of AlN (4.2 x 10^{-6} K^{-1}) is in between of those for ZnO (4.75 x 10^{-6} K^{-1}) and Si (2.6 x 10^{-6} K^{-1}) [**8**]. The overgrowth of AlN on Si(111) occurs by means of domain matching epitaxy [**13**], in which integral multiples of the film and the substrate lattice blocks may match at the interface. In its turn, ZnO can be grown on AlN by means of lattice-matching epitaxy on behalf of comparably lower lattice mismatch and Tiwari *et al.* [**14**] were probably the first to report on

the application of AlN buffers. However, the properties of ZnO films need to be optimized with respect to the AlN buffer layer thickness as it was done in other film/buffer systems [**15**]. Indeed, the lattice mismatch between the ZnO films and the AlN buffer can be readily modulated by varying the buffer thickness accounting for different degrees of strain relaxation in the basal plane of the buffer. Specifically for the domain matching epitaxy, the film undergoes complete strain relaxation only after reaching a critical thickness.

In this work, we have investigated the effect of the AlN buffer layer thickness on the properties of ZnO films fabricated on Si(111).

2. Experimental

AlN buffer layers were grown on Si(111) substrates by a low-pressure metal organic vapor phase epitaxy (MOVPE). Trimethylaluminium (TMAl) and ammonia (NH_3) carried by H_2 gas were employed as precursors for Al and N and detail on the AlN growth conditions may be found elsewhere [**16**]. The variation of the AlN thickness was reached by changing deposition time leaving all other parameters constant resulting in 20, 50, 70 and 100 nm thick AlN films. AlN surface exhibited variations of root mean square (RMS) roughness of 6 to 7 nm. Next, ZnO films were fabricated on these four AlN / Si(111) templates by atmospheric pressure MOVPE. A control ZnO sample was also fabricated on bare Si(111) substrate without AlN buffer layer for comparison. The templates were cleaned using acetone and ethanol in an ultrasonic bath, while the bare Si(111) was additionally etched in HF based solution in order to remove the native oxide layer. Prior to loading into the chamber, the substrates were rinsed with deionized water and dried in N_2 gas. The chamber was pumped down to 600 Torr and a preheating stage at 700 ^{o}C for several minutes was employed.

Afterwards, diethylzinc (DEZn) and tertiary-butanol (t-BuOH) were used as precursors supplying Zn and O, respectively. Both DEZn and t-BuOH were carried by N_2 and introduced into the chamber through separated injectors as described in details elsewhere [**17**]. Specifically, the flow rate of DEZn and t-BuOH was set at 90 and 400 sccm, respectively, DEZn bubbler was kept in a coolant bath at 10°C, while t-BuOH was maintained at 30^{o}C. The susceptor temperature and chamber pressure was maintained at 370 ^{o}C and 600 Torr, respectively. The samples were labeled as xAlN, where x denotes the AlN buffer layer thickness in nm (0, 20, 50, 70 and 100). The ZnO growth duration was 30 min in all processes resulting in ~ 250 nm-thick ZnO films as measured with a surface profilometer (Dektak8, Veeco Instruments Ltd). The crystallinity of ZnO is known to gradually improve itself with increasing film thickness [**18**], hence the samples were grown maintaining similar thicknesses in order to discriminate the role of AlN buffer in crystal quality.

The structure of the samples was characterized by x-ray diffraction (XRD) 2θ and ω scans using CuK_a ($\lambda = 0.1542$ nm) radiation source. A single Bragg reflection detected from the film suggests its epitaxial relationship with the substrate, whereas full width at half maximum (FWHM) of such peaks can be considered as a measure of crystalline quality of the film. Two types of XRD configurations were used to analyze the samples to extract the lattice parameters. Normal 2θ/θ configuration was employed to determine the out-of-plane *c* lattice parameter from (002) ZnO Bragg plane. The *a* lattice parameter is extracted from (103) ZnO reflection by modified Bragg-Brentano gracing incidence 2θ measurements. The strain ε accommodated in the film was estimated from the relationship $\varepsilon = (d_f - d_0)/ d_0 * 100\%$, where d_f and d_0 are the lattice parameters in the film and strain-free bulk ZnO, respectively. The surface morphology was monitored by atomic force microscope (AFM, Nanoscope IIIa SPM, Veeco Digital Instruments Ltd) in a tapping mode with a scan range from 2 × 2 μm^2 to 10 × 10 μm^2 at several random locations. Optical properties of the films were investigated by

photoluminescence (PL) at 10 K and 300 K temperatures using 325 nm He-Cd laser as an excitation source. The emission was collected by a microscope and directed to imaging spectrometer (HORIBA Jobin Yvon, iHR320) equipped with EMCCD camera (Andor DL658M) and also to fiber optic spectrometers (Ocean Optics, HR4000 and USB4000) with 0.2nm and 2nm spectral resolutions, respectively. Low temperature measurements were performed using closed-cycle He-refrigerator (Janis, Inc., CCS450).

3. Results and Discussion

Figure 1 shows typical XRD 2θ scans taken from as-grown ZnO films synthesized on AlN/Si(111) templates employing a variation of the AlN buffer layer thickness (0-100 nm). The data are labeled in accordance with notations introduced in previous section. As can be seen from Figs.1(a-d), all samples containing AlN buffers demonstrate a preferential orientation exhibiting (002) and (004) reflections characteristic for w-ZnO. Note that 0AlN sample features no characteristic (004) w-ZnO reflection (see Fig.1e), what is indicative of its inferior crystalline quality. Moreover, the intensity of (002) w-ZnO reflection increases for thicker AlN buffer layers (see Fig.1) implying gradual improvement of the crystalline quality. The 2θ scans also show the characteristic (002) and (004) Bragg peaks of AlN as well as (222) Si reflections.

Figure 2 shows variation of (002) ZnO and AlN peak width as a function of the AlN buffer thickness extracted from 2θ scans presented in Fig.1. For samples containing AlN buffers, the FWHM is found to be around 0.19^{o} compared to 0.23^{o} for ZnO grown on bare Si(111) substrate. FWHM data of ω scans around (002) ZnO and AlN peaks are also included in Fig.2 for extended analysis of the films. Interestingly, the FWHM values from ZnO ω–scan

are found to gradually decrease toward ~2.27^{o} for 70AlN sample and then slightly increases for the 100AlN sample. Note that the corresponding ω–scan FWHM value in the case of 0AlN sample appears too large to be determined accurately, hence proving its poor crystalline quality. It is a well-known fact that hetero-epitaxial layers grown on lattice-mismatched substrates usually exhibit high density of dislocations, which is a major cause of the ω–scan broadening [**19**]. For wurtzite lattices, e.g. ZnO/GaN, screw dislocations have a Burger's vector along the c-direction, and the dislocation density variations can be deduced from the FWHM data of symmetric XRD scans, specifically following the ZnO ω–scan evolution in Fig.2 [**20**]. Note rather large ZnO ω–scan FWHM values in Fig.2 account for relative thinness of the films [**18**] and the misorientation inherited from the buffer layer [**21**]. The ω-scan FWHM values of AlN buffer layer varies monotonically from 0.84^{o} to 0.75^{o} with increasing thickness from 20 to 100 nm. Rahmane *et al.* [**21**] have shown that the ZnO thin film deposited on AlN substrate exhibits an epitaxial growth which is strongly dependent on the crystalline quality of AlN film and also demonstrated a quasi-linear relationship between the (002) ω-curves of ZnO and AlN. The latter is also observed in our measurements maintaining linear relationship excluding sample 70AlN (see open squares in Fig. 2).

Figure 3 summarizes the values of accumulated strain in ZnO films extracted from XRD scans as a function of AlN buffer layer thicknesses. Here, $\varepsilon_{\perp}$ denotes strain in direction perpendicular to (002) basal plane and is estimated from the changes in *c* lattice parameter. Accordingly, $\varepsilon_{\parallel}$ represents strain component parallel to basal plane and is calculated from changes in *a* lattice parameter. One can readily observe that the relative strain along c-axis monotonously increases with increasing AlN buffer thickness and is of tensile character. On the other hand, the compressive in-plane strain $\varepsilon_{\parallel}$ initially decreases with AlN layer thickness, then abruptly peaks for 70AlN sample and decreases again for 100AlN. The 50AlN sample is

found to contain nearly $\varepsilon_{||}$ strain-free ZnO film with a residual $\varepsilon_{\perp}$ strain of ~ 0.34 %. In general, the origin of strain in a thin-film structure can be attributed to (i) lattice mismatch between the film and substrate (or buffer layer); (ii) difference in the thermal expansion coefficient (TEC) of the film and substrate (or buffer layer); (iii) microstructure/defect related internal stresses. The lattice mismatch arises from the differences in lattice constants between the film and the substrate under epitaxial growth conditions. If lattice constant of a film, d_f, is smaller than that of a substrate, d_s, then a tensile stress builds up in the film; and conversely, a compressive strain occurs in the case of $d_f > d_s$. In view of the fact that the in-plane lattice parameter of ZnO is larger than that of AlN, the lattice-mismatch related strain is expected to be compressive for the ZnO/AlN/Si(111) heterostructure [**14**]. Furthermore, it is well known that as soon as the critical thickness is reached, the lattice-mismatch strain may be dissipated by generating dislocations. However, thermal strain can develop as the film cools down due to different TEC of the substrate (α_s) and film (α_f), exhibiting a tensile nature in the case $\alpha_f > \alpha_s$ and compressive one, if $\alpha_f < \alpha_s$. Consequently, the larger TEC in ZnO compared to that in AlN and Si implies a tensile character of thermal strain in ZnO films. The last potential cause of the strain, namely, the microstructure/defect related internal stress, originates from the trapped point/line defects, such as vacancies, interstitials, dislocations, etc. In case the vacancies have lower specific volume compared to the host lattice, then a net tensile stress prevails in the film, e.g., oxygen vacancies in ZnO films are considered to cause tensile strain [**22**]. A simplified model illustrating the abovementioned lattice parameter variations with AlN buffer thickness is presented in the upper part of Fig. 3.

Figure 4 shows the AFM (2×2 μm^2) images of ZnO films grown on AlN/Si(111) templates as a function of AlN buffer layer thickness. ZnO films on bare Si(111) substrate (0AlN) exhibit grainy surface morphology with RMS roughness of ~16nm (Fig.4(a)). On the other hand, Figs.4(b)-(e) clearly shows that the films are formed by stacking of multiple grains that

have not entirely coalesced, as numerous voids can be observed in between grains (marked by arrows in panel(c)). The samples 20AlN and 50AlN (Figs.4(b) and (c)) demonstrate relatively rough surface with spherical grain morphology, while 70AlN and 100AlN (Figs.4(d) and (e)) exhibit somewhat elongated grains. Fig.4(f) summarizes AFM data scanned over a larger $10 \times 10\ \mu m^2$ area exhibiting RMS roughness in the range from ~ 9 to 22 nm. Note that 0AlN film grown on bare Si(111) substrate exhibit similar surface roughness values to those of AlN on Si(111). The roughness of the ZnO films grown on AlN/Si(111) templates could be inherited from the AlN buffer layer. Raghavan *et al.* [**23**] has shown that tensile stress is generated during the growth of AlN on Si(111) due to grain coalescence and also proved that the tensile stress varies both with growth temperature and along thickness of the AlN film. By comparing Figs.3 and 4(f), one can observe that the surface roughness is increasing upon decrease of the in-plane strain $\varepsilon_{\|}$ and vice versa.

The crystallinity assessment of the ZnO films on AlN/Si(111) templates has been also carried out by PL measurements. Room temperature (300K) luminescence spectra are presented in Fig. 5(a), for all samples demonstrating dominant near-band-edge (NBE) emission centered at around 3.29 eV and originating primarily from the free-exciton (FX) annihilation. A broad deep-level emission (DLE) band of considerably lower intensity can be also observed in the visible region of the spectra. The origin of the luminescent deep-levels is usually attributed to native point defects in ZnO [**24, 25**]. Figure 5(b) shows the high-energy part of the PL spectra measured at 10K. The dominating NBE lines are identified as excitons bound to ionized ($D^+X - I_3 = 3.365$ eV) and neutral donors ($D^0X - I_8 = 3.359$ eV) subsequently followed by corresponding longitudinal optical (LO) phonon replicas with an energy separation of **72** meV [**1, 26**]. However, most important feature is a prominent free-exciton peak (FX_A – 3.376 eV) observable in NBE spectra of all samples except for the 0AlN. Indeed, the presence of free-excitons at cryogenic temperatures is usually considered as indication of high crystalline

quality, since excitons tend to bound to all kinds of impurities and imperfections. In this respect, the apparent absence of FX line only in the emission from ZnO grown on Si(111) without AlN layer serves as yet another proof that AlN buffer ensures superior crystallinity of the films. In what follows we exploit this feature further and use the intensity ratio of free-exciton to neutral donor-bound-exciton lines (FX/D^0X) as a measure of crystalline quality of the films. As a particular case, similar intensity ratio involving ionized donor-bound excitons (FX/D^+X) is assumed to shed light on electrically active extended defects, allowing to characterize to some extent the density of dislocations [**27, 28, 29**].

Figure 6 summarizes variations of optical parameters as a function of AlN buffer layer thickness, namely NBE peak position at 300K and intensity ratios of defect-related DLE, neutral and ionized donor-bound excitons with respect to free-exciton emission. At room temperature, the NBE peak is dominated by free-exciton FX recombination and shows certain correlation with the variation of compressive $\varepsilon_{||}$ strain in the films established by XRD. Assuming that 50AlN sample represents nearly strain-free film and considering its FX position as a reference, all other samples exert blue-shifted peaks, suggesting an increase of the bandgap due to accumulated compressive strain. Still, taking into account the complexity of strain assessment by optical means [**30, 31, 32**] and also the smallness of the observed shifts, the compressive nature of stress concluded above should be rather considered as an indication than proof. The intensity ratio of the NBE and DLE spectral components is commonly used as a measure of ZnO crystalline quality. The variation of the NBE/DLE ratio as a function of AlN buffer thickness is presented in Fig.6(b). Note obvious superiority of the 50AlN sample which is in good agreement with the aforementioned similar conclusion derived from the XRD measurements. The intensity ratio of the free-exciton to bound-exciton emission can provide information on the quality of the ZnO films, i.e. the increasing FX_A/D^oX ratio would suggest relative decrease of the donor-like intrinsic defect concentration

and hence signify superior crystalline quality of the film. From Figs.3 and 6(c) one can readily observe that FX_A/D^oX ratio is highest for 50AlN sample, which was also found to exhibit minimal in-plane $\varepsilon_{||}$ strain. Moreover, the variation of FX_A/D^oX ratio as a function of AlN buffer thickness apparently correlates with that of the strain accumulated along the basal-plane, i.e. the increasing $\varepsilon_{||}$ strain corresponds to decreasing FX_A/D^oX ratio. Similar trend can be observed in the correlation of FX_A/D^+X ratio and tensile $\varepsilon_{\perp}$ strain (see Figs.3 and 6(d)), where reduction of strain is followed by mounting free-exciton contribution. As mentioned earlier, the interrelation between D^+X and tensile $\varepsilon_{\perp}$ strain could be attributed to the dislocation density along the c-axis and requires a more detailed study.

4. Conclusion

In summary, high quality ZnO films have been successfully grown by MOVPE on Si(111) substrates employing AlN as a buffer layer. The influence of AlN buffer layer thickness on the structural and optical properties has been studied. Based on the optical and structural characterization results, the optimal AlN buffer layer thickness is found to be ~ 50 nm resulting in minimal in-plane strain in the films. The obtained results also show that: (i) the structural quality of the ZnO film is strongly influenced by the quality and the thickness of the AlN buffer layer; (ii) the film grown using AlN buffer layer shows stronger free exciton emission compared to ZnO grown on bare Si(111); (iii) certain correlation between the strain and the optical band gap E_g variation was established, (iv) free-to-bound exciton emission ratios (FX_A/D^oX and FX_A/D^+X) are found to be correlate with the in-plane $\varepsilon_{||}$ and out-of-plane $\varepsilon_{\perp}$ strain, respectively.

Acknowledgement

Financial support from the Research council of Norway via FRINAT project is gratefully acknowledged.

Reference

[1] U. Ozgur, Y. I. Alivov, C. Liu, A. Teke, M. A. Reshchikov, S. Dogan, V. Avrutin, S.-J. Cho, H. Morkoc, J. Appl. Phys. 98 (2005) 041301.

[2] E.V. Monakhov, A. Yu Kuznetsov, B.G. Svensson, J. Phys. D: Appl. Phys. 42 (2009) 153001.

[3] S.J. Pearton, W.T. Lim, J.S. Wright, L.C.Tien, H.S.Kim, D.P. Norton, H.T. Wang, B.S. Kang, F. Ren, J. Jun, J. Lin, A. Osinsky, J. Electronic Mater. 37 (2008) 1426.

[4] N. Kawamoto, M. Fujita, T. Tatsumi, Y. Horikoshi, Jpn. J. Appl. Phys. 42 (2003) 7209.

[5] Y. Chen, F. Jiang, L. Wang, C. Zheng, J. Dai, Y. Pu, W. Fang, J. Cryst. Growth 275 (2005) 486.

[6] F. Li, D. Li, J. Dai, H. Su, L. Wang, Y. Pu, W. Fang, F. Jiang, Superlattices and Microstructures 40 (2006) 56.

[7] A.B.M.A Ashrafi, A. Ueta, A. Avramescu, H. Kumano, I. Suemune, Appl. Phys. Lett. 76 (2000) 550.

[8] L. Wang, Y. Pu, Y.F. Chen, C.L. Mo, W.Q. Fang, C.B. Xiong, J.N. Dai, F.Y. Jiang, J. Cryst. Growth 284 (2005) 459.

[9] A. Nahhas, H.K. Kim, J. Blachere, Appl. Phys. Lett. 78 (2001) 1511.

[10] J. Zhu, B. Lin, X. Sun, R. Yao, C. Shi, Z. Fu, Thin Solid Films 478 (2005) 218.

[11] M. Kumar, R. M. Mehra, A. Wakahara, M. Ishida, A. Yoshida, J. Appl. Phys. 93 (2003) 3837.

[12] C. Jin, R. Narayan, A. Tiwari, H. Zhou, A. Kvit, J. Narayan, Mater. Sci. Eng. B 117 (2005) 348.

[13] R.D. Vispute, J. Narayana, H. Wu, K. Jagannadham, J. Appl. Phys. 77 (1995) 4724.

[14] A. Tiwari, M. Park, C. Jin, H. Wang, J. Mater. Res. 17 (2002) 2480.

[15] A.A. Ashrafi, A. Ueta, H. Kumano, I. Suemune, J. Cryst. Growth 221 (2000) 435.

[16] I-H. Lee, S.J. Lim, Y. Park, J. Cryst. Growth 235 (2002) 73.

[17] A.J. Clayton, A.A. Khandekar, T.F. Kuech, N.J. Mason, M.F. Robinson, S. Watkins, Y. Guo, J. Crystal Growth 298 (2007) 328.

[18] E.S. Shim, H.S. Kang, J.S. Kang, J.H. Kim, S.Y. Lee, Appl. Surf. Sci. 186 (2002) 474.

[19] Y.J. Sun, O. Brandt, T.Y. Liu, A. Trampert, K.H. Ploog, J. Blasing, A. Krost, Appl. Phys. Lett. 81 (2002) 4928.

[20] B. Heying, X.H. Wu, S. Keller, Y. Li, D. Kapolnek, B.P. Keller, S.P. Denbaars, J.S. Speck, Appl. Phys. Lett. 68 (1996) 643.

[21] S. Rahmane, B. Abdallah, A. Soussou, E. Gautron, P.-Y. Jouan, L.L. Brizoual, N. Barreau, A. Soltani, M.A. Djouadi, Phys. Stat. Sol. (a) 207 (2010) 1604.

[22] A. Janotti, C.G. Van de Walle, Appl. Phys. Lett. 87 (2005) 122102.

[23] S. Raghavan, J. M. Redwing, J. Appl. Phys. 96 (2004) 2995.

[24] V. Venkatachalapathy, A. Galeckas, A. Zubiaga, F. Tuomisto, A. Yu. Kuznetsov, J. Appl. Phys. 108 (2010) 046101.

[25] K.T. Roro, J.K. Dangbegnon, S. Sivaraya, A.W.R. Leitch, J.R. Botha, J. Appl. Phys. 103 (2008) 053516.

[26] B.K. Meyer, H. Alves, D.M. Hofmann, W. Kriegseis, D. Forster, F. Bertram, J. Christen, A. Hoffmann, M. Strasburg, M. Dworzak, U. Haboeck, A.V. Rodina, Phys. Stat. Sol. (b) 241 (2004) 231.

[27] E. Muller, D. Gerthsen, P. Bruckner, F. Scholz, Th. Gruber, A. Waag, Phys. Rev. B 73 (2006) 245316.

[28] Y. Ohno, T. Taishi, I. Yonenaga, Phys. Stat. Sol. (a) 206 (2009) 1904.

[29] Y. Ohno, H. Koizumi, T. Taishi, I. Yonenaga, K. Fujji, H. Goto, T. Yao, J. Appl. Phys. 104 (2008) 073515.

[30] T.P. Rao, M.C.S Kumar, S.A. Angayarkanni, M. Ashok, J. Alloys and Compounds 485 (2009) 413.

[31] R. Ghosh, D. Basak, S. Fujihara, J. Appl. Phys. 96 (2004) 2689.

[32] Y.Q. Gai, B. Yao, Y.M. Lu, D.Z. Shen, J.Y. Zhang, D.X. Zhao, X.W. Fan, Phys. Lett. A 372 (2007) 72.

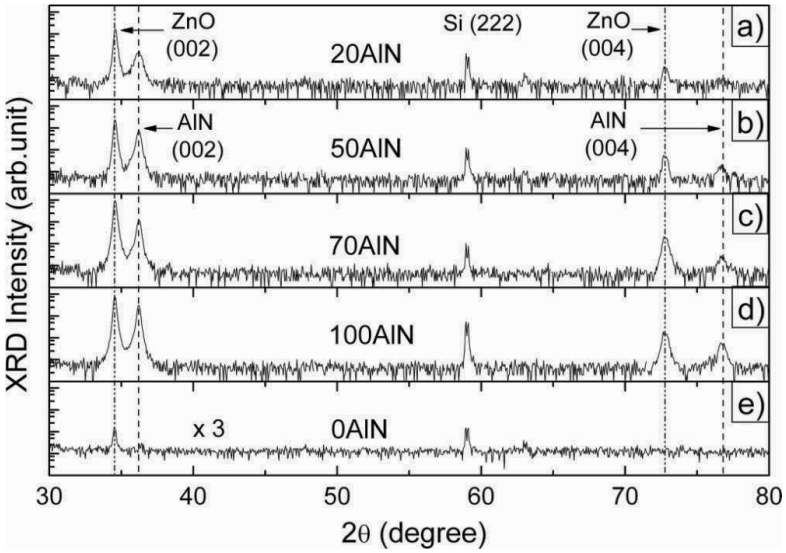

Fig. 1. XRD spectra (semi-log scale) of as-grown ZnO films as a function of the AlN buffer layer thickness. Dashed and dash-dotted lines mark positions of the characteristic Bragg peaks corresponding to AlN and ZnO, respectively.

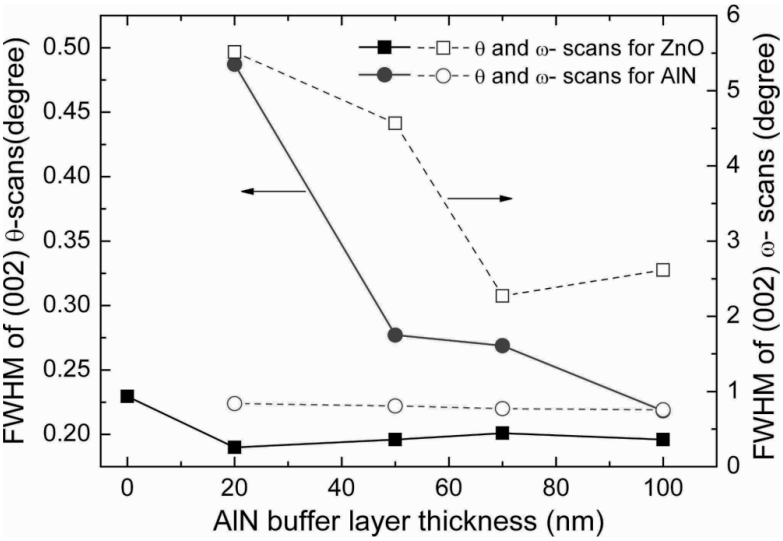

Fig. 2. XRD (002) peak width as a function AlN buffer layer thickness. FWHM parameters are extracted from the Bragg reflection and rocking curve for ZnO and AlN, respectively.

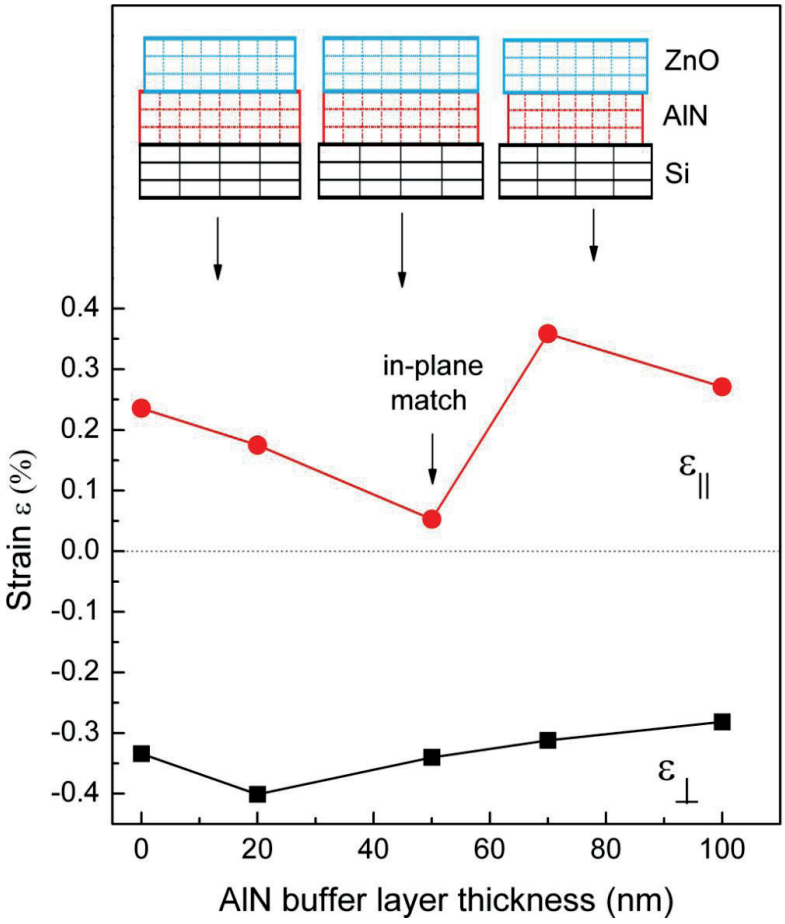

Fig. 3. Strain ε (%) accumulated in ZnO films as a function of AlN buffer layer thickness estimated from XRD 2θ scans. Here, $\varepsilon_{\perp}$ denotes strain in the direction perpendicular to (002) basal plane and is estimated from the changes in *c* lattice parameter; $\varepsilon_{||}$ represents strain component parallel to basal plane and is calculated from the changes in *a* lattice parameter. Inset shows a simplified model illustrating the variation of lattice parameters with AlN buffer thickness.

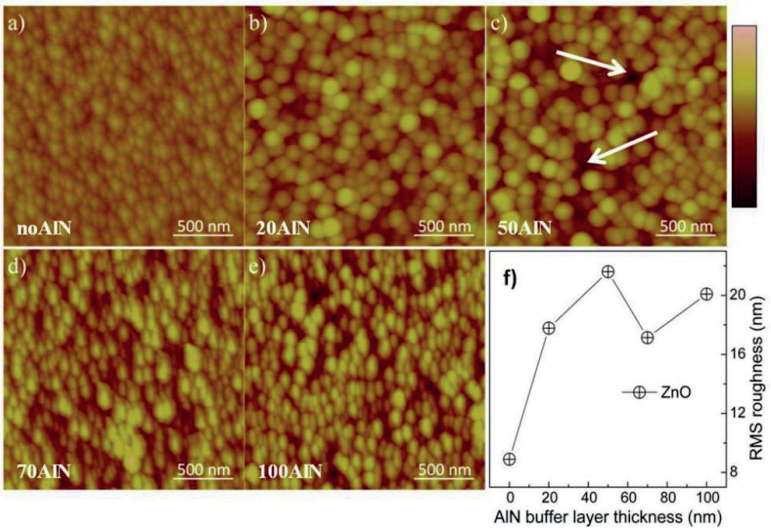

Fig.4. AFM surface morphology images (2×2 μm^2) of ZnO/AlN/Si(111) structures and corresponding RMS roughness as a function of AlN buffer thickness. The arrows in panel (c) mark the voids between the grains. The colour bar represents height scale from 0 to 200 nm.

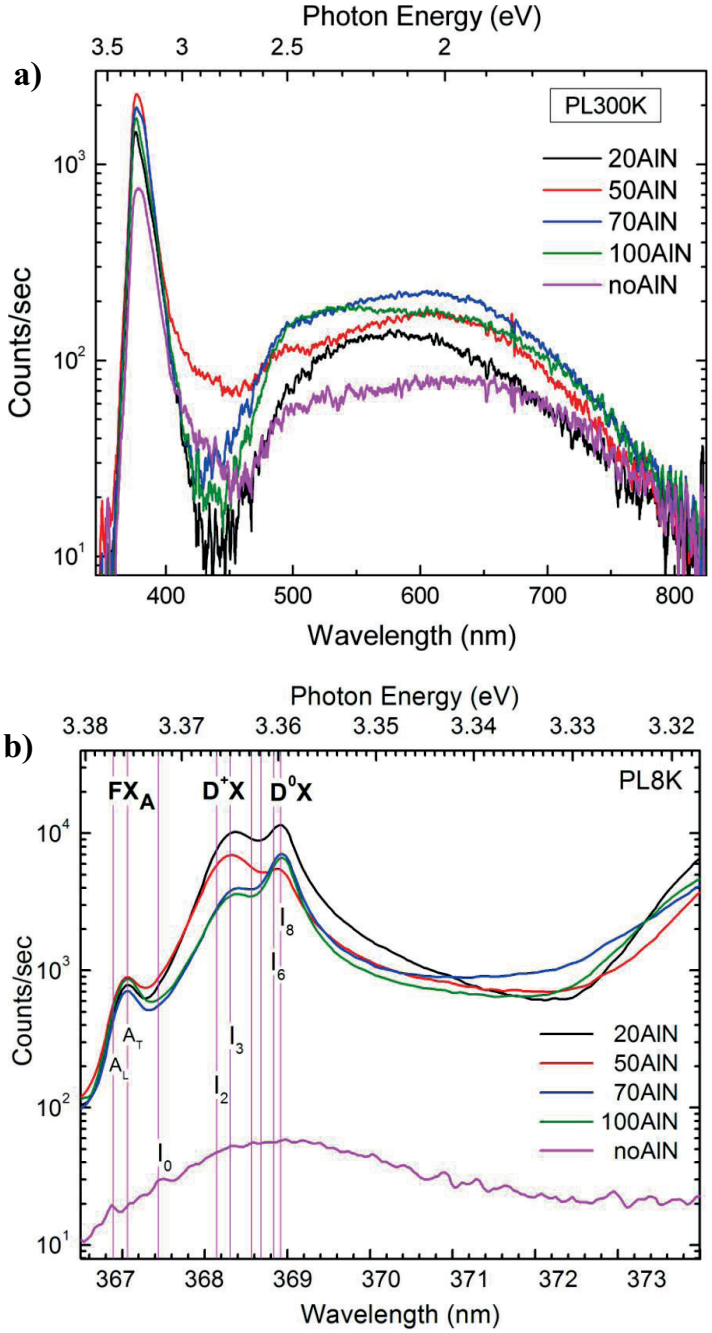

Fig.5. PL spectra of ZnO films on AlN/Si(111) templates as a function of AlN buffer layer thickness measured at 300K (a) and 10K (b) temperatures.

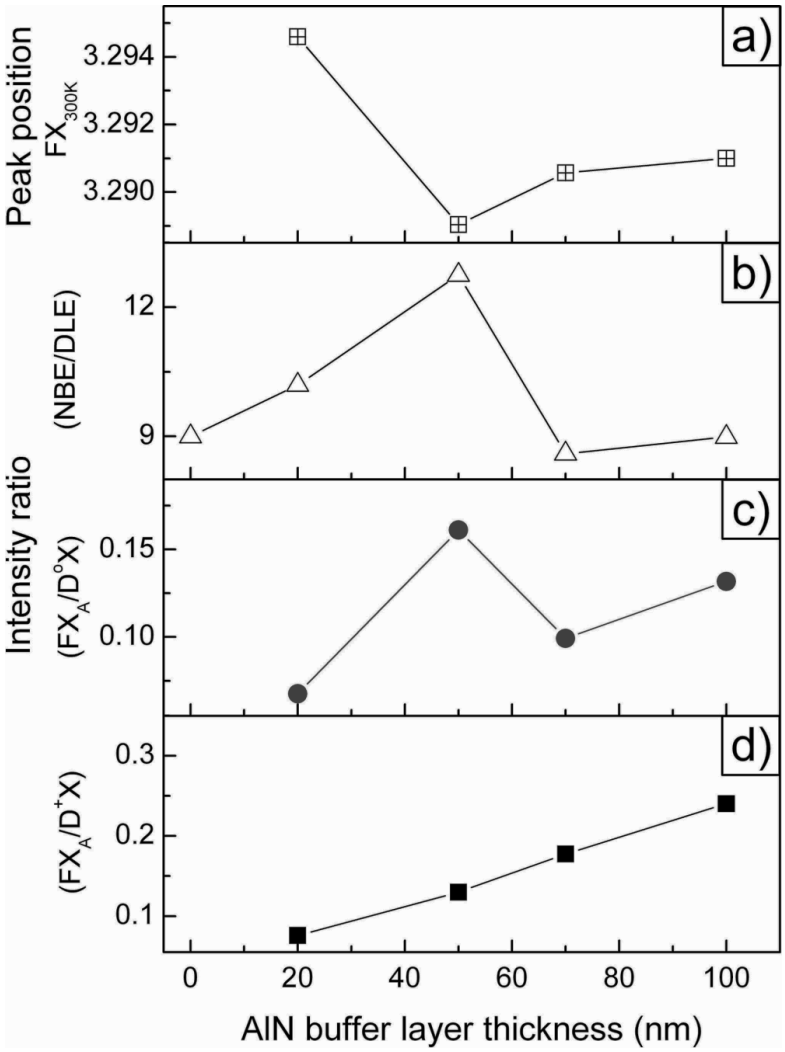

Fig.6. Variation of optical parameters as a function of AlN buffer layer thickness for ZnO films on AlN/Si(111) templates: (a) FX_{300K} peak position, (b) NBE/DLE, (c) FX_A/D^oX and (d) FX_A/D^+X.

Changing vacancy balance in ZnO by tuning synthesis between zinc/oxygen lean conditions

V. Venkatachalapathy, A. Galeckas, A. Zubiaga, F. Tuomisto and A.Yu.Kuznetsov

Journal of Applied Physics, **108**, 046101 (2010).

III

Changing vacancy balance in ZnO by tuning synthesis between zinc/oxygen lean conditions

Vishnukanthan Venkatachalapathy,[1,a)] Augustinas Galeckas,[1] Asier Zubiaga,[2] Filip Tuomisto,[2] and Andrej Yu. Kuznetsov[1]
[1]*Department of Physics, Centre for Materials Science and Nanotechnology, University of Oslo, P.O. Box 1126 Blindern, N-0318 Oslo, Norway*
[2]*Department of Applied Physics, Aalto University, P.O. Box 11100, 00076 Aalto, Espoo, Finland*

(Received 17 March 2010; accepted 8 June 2010; published online 25 August 2010)

The nature of intrinsic defects in ZnO films grown by metal organic vapor phase epitaxy was studied by positron annihilation and photoluminescence spectroscopy techniques. The supply of Zn and O during the film synthesis was varied by applying different growth temperatures (325–485 °C), affecting decomposition of the metal organic precursors. The microscopic identification of vacancy complexes was derived from a systematic variation in the defect balance in accordance with Zn/O supply trends. © *2010 American Institute of Physics*. [doi:10.1063/1.3462394]

Zinc oxide (ZnO) attracts considerable attention on behalf of its unique physical properties, offering a variety of multifunctional applications in optoelectronics, transparent electrodes, and sensors.[1–3] Several methods to fabricate ZnO thin films have been demonstrated so far,[4] among which metal organic vapor phase epitaxy (MOVPE) has been studied as a function of reactor type, growth conditions, and substrate variations for the attainment of high quality material.[5] Note, the microscopic understanding of the intrinsic defects in ZnO is important because of its potential to resolve the p-type doping problem in ZnO.[6] A method providing direct means of vacancy-type defect identification in semiconductors and ZnO in particular is positron annihilation spectroscopy (PAS).[7] To date PAS studies have mostly addressed defect formation in bulk ZnO with only a few reports on MOVPE-ZnO films,[8,9] partly because of a lack of high quality material until recently and also more complicated interpretation of the annihilation data in thin films. On the other hand, vacancy-type defects in ZnO thin films have been extensively studied using photoluminescence (PL),[10] although the exact correlation of deep-level emission (DLE) peaks with specific intrinsic defects still remains a matter of ongoing discussions.[1,5,11] In this respect, a combination of PAS/PL measurements might be capable to reveal the nature of the dominating intrinsic defects in MOVPE-ZnO films. To make such identification conclusive, it is essential to provide samples exhibiting systematic variations in the intrinsic defect balance. In the present work, we have prepared such samples by varying MOVPE-synthesis temperature (325–485 °C), which resulted in different amounts of Zn and O supplied to the reaction zone in the process of the precursor decomposition.[12] Thus, the defect concentration balance in the films was influenced in a controlled way, allowing for direct correlation of characteristic PAS/PL signatures as well as their microscopic assignment.

ZnO films used in this study were grown on r-axis oriented sapphire (r-Al_2O_3) substrates by MOVPE. Diethylzinc (DEZn) and tertiarybutanol (t-BuOH) were used as precursors for Zn and O reagents, respectively. Both DEZn and t-BuOH were carried by N_2 and introduced into the chamber through separated injectors over a rotating platen holding the substrates.[13] Effectively, the substrates are alternately "dosed" with certain amounts of Zn/O reagents attached to the surface as a function of the growth temperature. The DEZn/t-BuOH flow rate ratio (1/1) and growth time (90 min) were kept constant resulting in 400–600 nm thick ZnO films. In addition, we have conducted tests employing flow rate variations in order to alter DEZn and t-BuOH delivery to the chamber in a more "direct" way. However, changing the flow rates will affect the partial pressures influencing precursor decomposition rates and a combination of these factors with temperature variation may result in a complicated trend. Importantly, the same II/VI molar ratio will in practice provide completely different amounts of Zn/O reagents depending on the growth temperature because of different degrees of precursor decomposition as a function of temperature.[12] Based on a set of preliminary experiments we understood that employing the temperature variation only we will cover a wide variation in the Zn/O reagent supply and decided to keep the flow rate constant for the rest of the experiment. All samples demonstrated similarly high crystalline quality as confirmed by ~0.15° full width at half maximum broadness of the (002) x-ray diffraction peak.

PL properties of the samples were investigated at 10 K temperature by employing 325 nm wavelength of cw He–Cd laser as an excitation source. In this work, we focus primarily on the spectral region of DLE and employ deconvolution techniques to analyze intensities and positions of the characteristic bands referring to data reported in literature[5,11] as well as to the trends resolved in our PAS measurements. The essence of the vacancy identification with PAS is in positron trapping at neutral and negative vacancy defects, which modifies the annihilation characteristics. The Doppler broadening of the 511 keV annihilation line was measured at room temperature using a variable energy positron beam in the 0–30 keV range. We characterized the Doppler spectra by

a)Electronic mail: vishnukv@smn.uio.no.

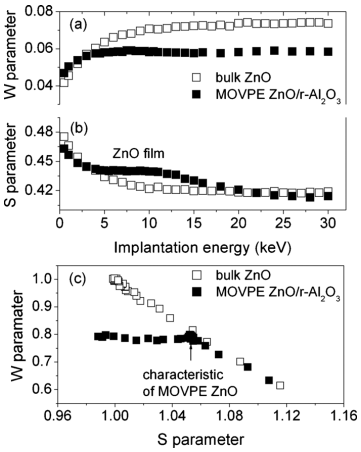

FIG. 1. Typical PAS data for the bulk ZnO reference sample and MOVPE-ZnO/r-Al_2O_3 structure grown at 385 °C. W and S parameters vs energy profiles are shown in panels (a) and (b), respectively, while panel (c) is the normalized to the bulk (S, W) plot.

conventional line shape parameters representing the fractions of annihilations with low-momentum (S) and high-momentum (W) electrons.[8]

Figure 1 shows a typical example of the PAS results in MOVPE-ZnO, while the data obtained in the bulk ZnO reference are shown for comparison. The reference sample contains only two annihilation states—surface and lattice [see open squares following a linear trend in Fig. 1(c)]. In contrast, the MOVPE sample contains more annihilation states (in part because of the different natures of the film and the substrate). As seen from Fig. 1(a) low energy positrons (0–3 keV) annihilate at surface states in the MOVPE structure similar to those in the reference sample, while 4–11 keV positrons annihilate in the ZnO film. At higher implantation energies, positrons start to annihilate in the substrate and are not considered in the further analysis. The characteristic values for S and W parameters detected in ZnO films [e.g., S = 1.05 and W = 0.79 in Fig. 1(c), representing the constant region at 4–11 keV in Figs. 1(a) and 1(b)] are used in further analysis.[8]

Figure 2 is a W-S plot containing characteristic (S, W) values of the MOVPE-ZnO films grown at different temperatures. In addition, reference parameters corresponding to the ZnO lattice and V_{Zn} (Ref. 14) are included in Fig. 2. First, we see that positron annihilation at open volume defects dominates in the films based on the high S-values in Fig. 2. Second, the position of the (S, W) values of the samples grown at 350 and 385 °C in the plot resembles saturation trapping of positrons and subsequent annihilation predominantly at defects related to the V_{Zn}. Reducing the growth temperature to 325 °C moves the data horizontally toward higher S-values in the plot, indicating formation of vacancy clusters, while increasing the synthesis temperature to ≥420 °C results in a clear trend for S(W) parameters to increase (decrease), indicating the formation of vacancy clusters of a different nature than those at the lowest growth

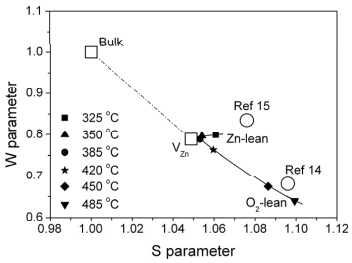

FIG. 2. W-S plot for MOVPE-ZnO synthesized at different temperatures. The reference annihilation states (bulk and V_{Zn}) are labeled by open squares. Open circles denote (S, W) trend points revealed in previous ion implantation experiments.

temperature. It should be noted that the positron diffusion length (L^+) (Ref. 8) decreases monotonically from about 20 nm to about 10 nm in the samples grown at ≥385 °C, indicating that no saturation trapping at V_{Zn} occurs in the samples grown at 350 and 385 °C. This means that in addition to V_{Zn} there are other annihilation states—vacancy clusters giving significant contributions to the positron data in these samples. Moreover, the reduction in L^+ implies that the positron trapping rate and hence the defect concentration (not only the size of the vacancy clusters) increases when the growth temperature is increased. Interestingly, the (S, W) parameters of the sample grown at 325 °C approach those of the vacancy clusters observed in Li-implanted and flash-annealed ZnO,[15] correlated with the characteristic 2 eV optical emission in Ref. 11.

PL results for the films synthesized at different temperatures are summarized in Fig. 3. Two distinct DLE components centered at around 2 and 2.5 eV can be readily observed, allowing for satisfactory deconvolution of all DLE spectra. The relative intensity of the green and red spectral signatures apparently correlates with the synthesis temperatures. Similar DLE components were observed by

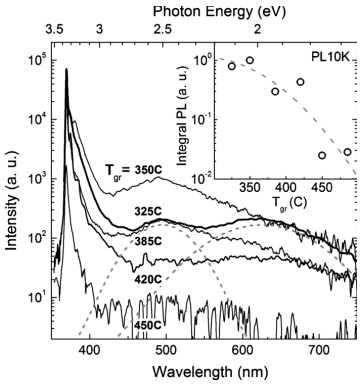

FIG. 3. PL spectra at 10 K for MOVPE-ZnO films grown at different temperatures (T_{gr}). Gaussian dotted curves are guides for eyes indicating two dominant deep-level emission components. The inset shows the evolution of the total PL yield integrated over entire emission spectrum as a function of growth temperature.

Dong *et al.*[11] in depth resolved cathodoluminescence (DRCL) experiments, with the 2 eV emission reportedly in a direct correlation with the vacancy cluster signals measured by PAS. Such association also appears consistent with the present PAS data, specifically considering clear dominance of the 2 eV emission in the films grown at 325 °C comparing to the rest of the samples in Fig. 3. It should also be noted that the overall luminescence yield, including both DLE and near-band-edge emission, notably decreases in the samples grown at elevated temperatures, as can be seen in the inset in Fig. 3, implying an increasing competition from the nonradiative recombination channels.

The trends presented in Figs. 2 and 3 can be explained in terms of changes in the Zn/O reagent supply due to variations in DEZn/t-BuOH thermal decomposition.[12] Indeed, the pyrolysis of DEZn starts at 300 °C and is not completed until the temperatures are well above 350 °C. Consequently, the 325 °C synthesis would result in Zn lean material which is consistent with detecting vacancy clusters formed of two or more missing Zn atoms in this sample in Fig. 2 as well as the 2 eV signature in Fig. 3. Please note that in spite the II/VI flow rate ratio was constantly maintained at ~1, the Zn/O reagent supply was effectively $\ll 1$ because insufficient decomposition of DEZn at "low" temperatures. Accounting that oxidizing properties of t-BuOH does not change in the range of 325–385 °C,[12] we can readily explain the transformation happening at 350 and 385 °C—more Zn is supplied in the reaction zone consistently with decreasing the S parameter (interpretable as a decrease in the cluster size) and changing annihilation parameters toward those of V_{Zn}. However, this initial trend breaks because of changing in oxidizing conditions at higher temperatures. Indeed, the presence of stable oxonium ion is responsible for Zn oxidation when using t-BuOH as an oxidizer.[16] However, the relative abundance of oxonium ion decreases drastically due to pyrolysis of t-BuOH which starts at elevated temperatures, likely >385 °C in our growth conditions.[12] Thus, the growth at temperatures > 385 °C results in insufficient oxidation and formation of another kind of vacancy cluster with the W parameter clearly lower comparing to that observed in the Zn-lean case. Interestingly, these points follow a trend similar to that observed in high-dose 2 MeV O^+ irradiated ZnO samples.[14] Taking into account the magnitude of the W parameters (which is determined by annihilations with high-momentum Zn 3*d* electrons) we conclude that there should be more Zn atoms present around annihilation states in samples grown at 325 °C. This can be readily interpreted as the vacancy clusters being of considerably smaller size in the Zn-lean sample.

The transformation happening when changing from Zn-lean to O-lean conditions is also confirmed by the evolution in PL data in Fig. 3. The 2 and 2.5 eV emissions coexist already in the sample grown at 325 °C and also the maximum of the DLE changes from 2 to 2.5 eV when increasing the growth temperature from 325 to 350 °C. This correlates with the PAS result that zinc vacancy related defects are the main positron traps strongly indicating involvement of zinc vacancies in the PL processes. Further, no (or only weak) DLE signals are observed for samples grown in O-lean conditions in Fig. 3 which is interpreted in terms of the formation of bigger clusters reducing radiative recombination in the DLE range. Assuming the defect evolution scenario discussed above and accounting that zinc lean conditions implies the formation energy of V_{Zn} to be lower that of V_o,[1] we may tentatively correlate 2.5 eV emission in Fig. 3 with V_{Zn}.[1,5]

In summary, an interpretation for the nature of vacancy-type defects in MOVPE-ZnO is suggested based on systematic variation in Zn/O lean conditions during synthesis in spite of generally complicated defect balance in the samples. The samples grown at 325 °C (most Zn-lean condition studied) are found to be enriched with vacancy clusters and the assignment of the 2 eV emission with V_{Zn}-clusters is confirmed. Samples synthesized at higher temperatures corresponding to O-lean conditions are found to contain bigger vacancy clusters responsible for damping of defect related radiative transitions in ZnO. In addition a characteristic 2.5 eV emission band is found to dominate at intermediate synthesis temperatures (350–385 °C) and is tentatively associated with radiative transition involving V_{Zn}.

Financial supports from the Research Council of Norway and mobility grants from NordForsk are gratefully acknowledged. This work was partially supported by the Academy of Finland.

[1] A. Janotti and C. G. Van de Walle, Rep. Prog. Phys. **72**, 126501 (2009).
[2] E. V. Monakhov, A. Yu. Kuznetsov, and B. G. Svensson, J. Phys. D: Appl. Phys. **42**, 153001 (2009).
[3] S. J. Pearton, W. T. Lim, J. S. Wright, L. C. Tien, H. S. Kim, D. P. Norton, H. T. Wang, B. S. Kang, F. Ren, J. Jun, J. Lin, and O. Osinsky, J. Electron. Mater. **37**, 1426 (2008).
[4] R. Triboulet and J. Perrière, Prog. Cryst. Growth Charact. Mater. **47**, 65 (2003).
[5] K. T. Roro, J. K. Dangbegnon, S. Sivaraya, A. W. R. Leitch, and J. R. Botha, J. Appl. Phys. **103**, 053516 (2008).
[6] D. C. Look and B. Claflin, Phys. Status Solidi B **241**, 624 (2004).
[7] F. Tuomisto, V. Ranki, K. Saarinen, and D. Look, Phys. Rev. Lett. **91**, 205502 (2003).
[8] A. Zubiaga, F. Tuomisto, F. Plazaola, K. Saarinen, J. A. Garcia, J. F. Rommeluere, J. Zuniga-Perez, and V. Munoz-Sanjose, Appl. Phys. Lett. **86**, 042103 (2005).
[9] Y. Hu, Y. Q. Chen, Y. C. Wu, M. J. Wang, G. J. Fang, C. Q. He, and S. J. Wang, Appl. Surf. Sci. **255**, 9279 (2009).
[10] Ü. Özgür, Y. I. Alivov, C. Liu, A. Teke, M. A. Reshchikov, S. Dogan, V. Avrutin, S.-J. Cho, and H. Morkoc, J. Appl. Phys. **98**, 041301 (2005).
[11] Y. Dong, F. Tuomisto, B. G. Svensson, A. Yu. Kuznetsov, and L. J. Brillson, Phys. Rev. B **81**, 081201 (2010).
[12] C. Thiandoume, V. Sallet, R. Triboulet, and O. Gorochov, J. Cryst. Growth **311**, 1411 (2009).
[13] A. J. Clayton, A. A. Khandekar, T. F. Kuech, N. J. Mason, M. F. Robinson, S. Watkins, and Y. Guo, J. Cryst. Growth **298**, 328 (2007).
[14] A. Zubiaga, F. Tuomisto, V. A. Coleman, H. H. Tan, C. Jagadish, K. Koike, S. Sasa, M. Inoue, and M. Yano, Phys. Rev. B **78**, 035125 (2008).
[15] T. M. Borseth, F. Tuomisto, J. S. Christensen, W. Skorupa, E. V. Monakhov, B. G. Svensson, and A. Yu. Kuznetsov, Phys. Rev. B **74**, 161202(R) (2006).
[16] D. A. Lamb and S. J. C. Irvine, J. Cryst. Growth **273**, 111 (2004).

Tuning light absorption by band gap engineering in ZnCdO as a function of MOVPE-synthesis conditions and annealing

V. Venkatachalapathy, A. Galeckas, R. Sellapan, D. Chakarov and A.Yu.Kuznetsov

Journal of Crystal Growth, **315**, 301 (2011)

IV

Understanding phase separation in ZnCdO by a combination of structural and optical analysis

V. Venkatachalapathy, A. Galeckas, M. Trunk, T. Zhang, A. Azarov and A. Yu. Kuznetsov

Physical Review B, **83,** 125315 (2011).

V

Understanding phase separation in ZnCdO by a combination of structural and optical analysis

Vishnukanthan Venkatachalapathy, Augustinas Galeckas, Mareike Trunk, Tianchong Zhang, Alexander Azarov, and Andrej Yu. Kuznetsov

Department of Physics/Centre for Materials Science and Nanotechnology, University of Oslo, P.O. Box 1048 Blindern, N-0316 Oslo, Norway

(Received 19 October 2010; published 23 March 2011)

A phenomenon of wurtzite (w), zincblende (zb), and rock-salt (rs) phase separation was investigated in ZnCdO films having Cd contents in the range of 0%–60% settling a discussion on the phase stability issues in ZnCdO. First, low-Cd-content ($\leqslant$17%) ZnCdO was realized preferentially in a w matrix determining optimal Zn-lean conditions by tuning the precursor decomposition rates during synthesis. However, more detailed analysis of x-ray diffraction and photoluminescence (PL) data revealed that the w single-phase stability range is likely to be as narrow as 0%–2% Cd, while samples containing 7%–17% of Cd exhibit a mixture of w and zb phases. Second, high-Cd-content (32%–60%) ZnCdO samples were realized, supplying more of the Cd precursor utilizing Zn-lean growth conditions, however, resulting in a mixture of w, zb, and rs phases. Characteristic PL signatures at 2.54 and 2.31 eV were attributed to zb-ZnCdO and rs-CdO, respectively, while the band gap variation in w-$Zn_{1-x}Cd_xO$ is given by (3.36–0.063x) as determined at 10 K. The phase separation is interpreted in terms of corresponding changes in the charge distribution and reduced stacking fault energy.

DOI: 10.1103/PhysRevB.83.125315 PACS number(s): 64.75.Qr, 81.05.Dz, 78.55.Cr

I. INTRODUCTION

Zinc oxide (ZnO) with a wide band gap (E_g) of $\sim$3.36 eV and a large exciton binding energy of $\sim$60 meV at room temperature is a promising material for optoelectronic application.[1] Moreover, ZnO can be mixed with CdO ($E_g \sim$ 2.3 eV) so that the alloy band gap can be potentially tuned in the range of 3.36–2.3 eV providing additional advantages in device performance. However, ZnO and CdO form in different stable crystal structures—wurtzite (w) and rock salt (rs), respectively—which complicates the fabrication of single-phase alloys in a broad compositional range. Up to now ZnCdO synthesis has been tested by a variety of methods, including metal organic vapor-phase epitaxy (MOVPE),[2,3] molecular beam epitaxy (MBE),[4] and pulsed-laser deposition (PLD),[5] confirming difficulties in maintaining its single phase.

Specific problems most commonly mentioned in literature—coexistence of several phases as well as spontaneous misorientation with increasing Cd content—still remain not fully understood.[3,6] In addition, different groups have reported inconsistent results for E_g and lattice parameters as a function of Cd content.[3–5,7–9]. Concurrently, the solubility of Cd in ZnO prepared by advanced thin-film synthesis was reported to vary in a wide range from 5%[3] to 69% Cd.[7] To the best of our knowledge there is no binary phase diagram for the ZnO-CdO system reported in literature, but several metallurgical experiments with complex oxides have proposed different ranges for solid solubility in the ZnO-CdO system.[10–12] Fundamentally, substituting Zn with Cd in a w-ZnO matrix might result in unfavorable electronic configuration for Cd ions in comparison to that in rs-CdO. However, there are only a few atomic arrangements feasible at a specific ZnCdO composition, limited to the forms of w-ZnO, rs-CdO, and zincblende (zb) matrixes (the latter is known to be metastable for both binary components) or their mixtures. It is also possible that different ZnCdO phases exhibit unexpected—for binary components—stability variations with Zn/Cd content. For example, zb phase, metastable under normal conditions,[13–16] may potentially emerge during a far-from-equilibrium synthesis of ZnCdO alloys, explaining the scattering in literature data. In the present work, we have investigated preferentially (002)-oriented ternary $Zn_{1-x}Cd_xO$ ($0 \leqslant x \leqslant 0.6$) films manufactured by an atmospheric pressure MOVPE and suggest a consistent phase evolution interpretation based on the correlation between x-ray diffraction (XRD) and photoluminescence (PL). The report is structured in the following way. Sec. II contains information on the sample synthesis and measurement details. Sec. III represents the body of the data and is split into subsections. Specifically, Sec. III A explains how the growth-temperature variation was used in order to determine optimal Zn-lean conditions promoting Cd incorporation into ZnCdO. Sec. III B is devoted to the exploration of high-Cd-content ZnCdO, employing various Cd flow rates. Sec. III C deals with the initial calibration of PL features observed in ZnCdO compared to optical signatures of pure w-ZnO and rs-CdO. Reasons and routes for the structural evolution in ZnCdO involving w, zb, and rs phases are discussed in the context of literature data in Sec. IV A. Possible mechanisms for the appearance of mixed w and zb phases are elaborated in Sec. III B accounting for XRD/PL data observed in our samples. Sec. V contains conclusions and is followed by acknowledgements.

II. EXPERIMENTAL

ZnCdO films used in this study were grown on *c*-axis-oriented sapphire (c-Al_2O_3) by an atmospheric pressure MOVPE. The substrates were cleaned using acetone and ethanol in an ultrasonic bath, followed by cleaning in an H_2SO_4:H_2O_2:H_2O (1:1:6) solution. Prior to inserting into the chamber, the substrates were rinsed with deionized water and dried in N_2 gas. Diethyl zinc (DEZn), dimethyl cadmium (DMCd), and tertiary butanol (*t*-BuOH) were used as zinc source, cadmium source and oxidizing agent, respectively. The flows of DEZn and *t*-BuOH were set at 100 and 150 sccm,

respectively. Both DEZn and DMCd bubblers were kept at 10 °C, while *t*-BuOH was maintained at 30 °C. Two methods were employed to vary Cd content in the films: (i) varying the growth temperature while keeping the DMCd flow constant at 20 sccm and (ii) varying the DMCd flow rate and keeping the growth temperature constant at 370 °C. Samples manufactured employing temperature variations were labeled as TX, so that X denotes the actual growth temperature in °C. Samples resulted from flow rate variations were labeled as FX, so that X denotes the actual DMCd flow rate applied in the synthesis in sccm units.

All precursors were carried by N_2 gas and introduced into the chamber through separated injectors, using the so-called "vectored-flow epitaxy" concept, introducing group II and VI precursors separately over a rotating susceptor platen. The rotation of the platen directs the gases across the substrates and out through separate exhausts, avoiding pre-reactions in the gas phase.[17] Effectively, the rotating substrates are alternately "dosed" with certain amounts of group II and VI reagents attached to the surface, and the II/VI precursor ratios in the reaction zone shall depend on the flow rates and decomposition conditions for DEZn/DMCd and *t*-BuOH. In its turn, the decomposition of precursors is governed by the substrate temperature. Thus, exploring the limits of Cd incorporation into w-ZnO, Zn-lean growth conditions[18] found in temperature-variation experiments were applied to maximize Cd content in w-ZnCdO. Further, flow-variation experiments were performed using this optimal Zn-lean condition. The deposition time for all samples was kept at 90 min, resulting in the film thickness in the range of 400–700 nm. Post-deposition anneals, if applied, were carried out in an O_2 atmosphere at 800 °C for 60 min. Pure rs-CdO/w-ZnO samples were also prepared with DMCd/DEZn flows of 150/100 sccm and a *t*-BuOH flow of 150 sccm at 370 °C in order to correlate structural and optical properties with stable binary phases. Note that rs-CdO was synthesized on *r*-axis-oriented sapphire (r-Al_2O_3) substrates because only high-index (025) reflections—not attainable by our XRD equipment—are visible in epitaxial rs-CdO/c-Al_2O_3 structures.[19]

The crystalline structure of the films was characterized by XRD with Cu K_α radiation (Siemens D5000), specifically revealing epitaxial relationships between the films and the substrates. Indeed, an appearance of a single Bragg reflection detected from the film suggests its epitaxial relationship with the substrate, and full width at half maximum (FWHM) of such a characteristic peak is one of the measures of crystalline quality of the film. For example, w-ZnO grown on c-Al_2O_3 is well characterized with its (002) reflection,[20] while (025) and (002) rs-CdO reflections are observed in CdO/c-Al_2O_3 and CdO/r-Al_2O_3 structures, respectively.[19] Note that XRD features of zb-ZnO appears to be close to those of rs-CdO, with characteristic (002) and (111) peaks at $2\theta = 39.50°$ and 34.00°, respectively.[15–21]

PL properties of the samples were investigated at 10 K and 300 K employing a 325-nm-wavelength cw He-Cd laser with an output power of 10 mW as an excitation source. The emission was collected with a microscope and directed to an imaging spectrometer (HORIBA Jobin Yvon, iHR320) equipped with an electron multiplying charge-coupled device (EMCCD) camera (Andor DL- 658M) and also to fiber-optic spectrometers (Ocean Optics, HR4000 and USB4000) with 0.2- and 2-nm spectral resolutions, respectively. Low-temperature measurements were performed using a closed-cycle He refrigerator (Janis, Inc., CCS450). Normalization of PL signals (if employed) was made to the maximum near-band-edge (NBE) intensity providing a better comparison for PL evolution trends with increasing Cd content.

The chemical composition in the samples was analyzed by Rutherford backscattering spectrometry (RBS) with 2-MeV $^4He^+$ ions backscattered into the detector at 170° relative to the incident beam direction. The stoichiometry of the films was determined from fitting the experimental spectra with simulated curves using the SIMNRA code.[22] Importantly, Cd profiles were found to be flat for all samples and an average content in the plateau was taken as a measure of Cd content in the film. It should be noted that the Cd signal from the higher-Cd-content samples is a non-trivial function of the RBS yield. The complication is due to the generation of a higher amount of secondary electrons from the heavier Cd atoms (comparing to Zn), which affects the dosimetry. Nevertheless, this issue has been taken into account when extracting Cd contents from the RBS spectra.

III. RESULTS

A. Determination of optimal Zn-lean conditions assisting Cd incorporation into ZnCdO

Figure 1 shows typical XRD 2θ scans taken from as-grown ZnCdO films synthesized at various temperatures in the range of 340 °C–430 °C. Note that samples T460, T490, and T520, i.e., grown at 460 °C, 490 °C, and 520 °C, respectively, exhibit XRD patterns identical to that of T430 and are omitted in Fig. 1 for clarity. The angular position of the Bragg peak observed in the T430 film coincides with that of a characteristic (002) reflection in pure w-ZnO within the accuracy of our measurements (see Fig. 1). For the samples grown at lower temperatures, there is a shift toward lower Bragg angles

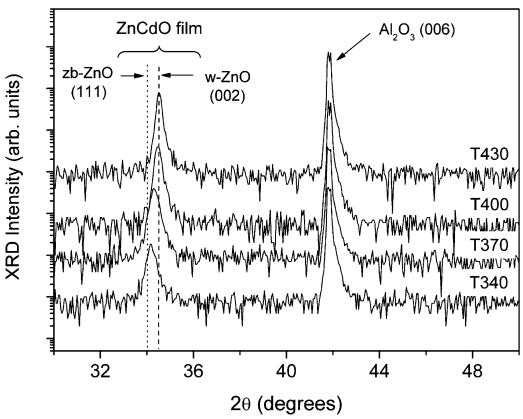

FIG. 1. Typical evolution of XRD intensities in as-grown ZnCdO/c-Al_2O_3 structures as a function of growth temperature. The dashed and the dotted lines label (002) and (111) Bragg peaks from pure w- and zb-ZnO, respectively.

(meaning higher interatomic spacing), as observed in Fig. 1, and may be expected from a substitution of smaller Zn atoms (0.74 Å) by larger Cd atoms (0.97 Å)[23] on equivalent crystallographic positions in the wurtzite lattice. Assuming the latter statement is true, there is a clear trend in Fig. 1 showing that the efficiency of Cd incorporation into w-ZnO increases with decreasing growth temperature. No distinct peaks related to reflections from rs-CdO were observed, indicating, in the first approximation, a single-phase wurtzite material in most of the films. However, we cannot exclude contributions coming from zb-ZnO (111) reflections, specifically for sample T340 (see Fig. 1). Indeed, assuming the w matrix is preserved in sample T340, the change in the lattice parameter is (Δc) $\sim$ 0.052 Å, as may be estimated from Fig. 1. However, the corresponding strain ($\sim$1%) is too big to preserve continuous material properties, and the shift in the peak position is likely due to the appearance of (111) zb-related phases. Concurrently, the diffraction pattern in T340 cannot be attributed to pure zb-ZnO only (or zb-ZnCdO) because of a considerable broadness of the peak.

The chemical composition in the films grown at different temperatures was independently analyzed by RBS. Figure 2 shows typical RBS spectra of ZnCdO samples grown at 340 °C, 400 °C, and 430 °C. Positions of O, Zn, and Cd atoms at the film surface are indicated in the figure by arrows. One can see that the fits to the Cd signals (see channels 420–460 in Fig. 2) are quite flat, indicating uniform Cd distribution throughout the film. Note that the RBS yield is proportional to the content of the species, which along with other relevant experimental parameters, were extracted in simulations. The actual Cd content in the samples is shown in the inset in Fig. 2 as a function of growth temperature. Clearly, the growth-temperature variation affects the film composition, showing that Cd content increases up to 17% with decreasing growth temperature from 520 °C to 340 °C.

Figure 3 summarizes the trends for the *c*-axis lattice parameter and the FWHM of the ZnCdO peak in Fig. 1 as

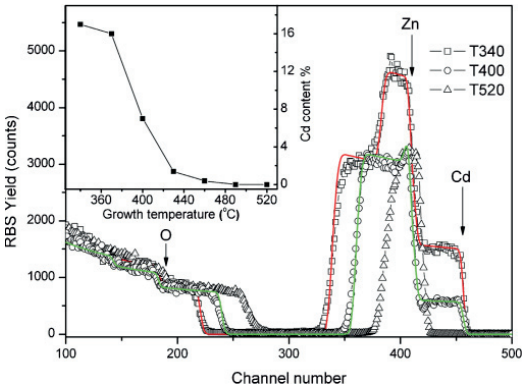

FIG. 2. (Color online) Typical RBS spectra of as-grown ZnCdO manufactured at 340 °C (□), 400 °C (○), and 520 °C (Δ) C, while lines represent the results of fitting. Corresponding Cd content is shown in the inset as a function of the growth temperature for all T-type samples.

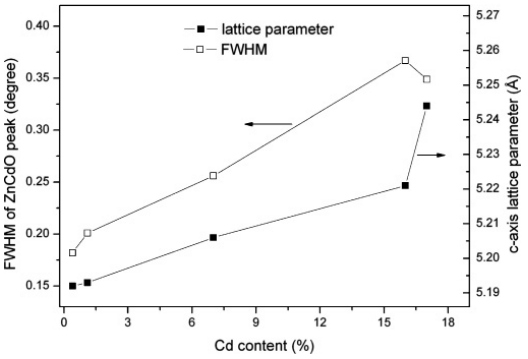

FIG. 3. *c*-axis lattice parameter and FWHM values extracted from Bragg reflections in ZnCdO films in Fig. 1 as a function of the Cd content.

a function of the Cd content as determined in Fig. 2. It is readily seen from Fig. 3 that the *c*-axis lattice parameter in ZnCdO films evolves linearly from that of pure w-ZnO (T520) to 5.22 Å (T370) and then increases abruptly for T340. Interestingly, the FWHM values of the (002) diffraction peak also evolve linearly in the same Cd content range (0.4%–16%) and then decreases for the highest Cd content. Considering the Zn-Cd size relationship and taking into account Figs. 1–3, we may assume that the substitution of Zn by Cd takes place on the equivalent crystallographic positions (Zn-sites) in w-ZnO matrix up to Cd content of 16% (T370). It is also likely that the mechanism changes in T340, as is discussed in more detail in Sec. IV, but note already now that the dominating Bragg reflection from T340 is closest to the zb-ZnO (111) position (Fig. 1).

Figure 4 shows the PL spectra obtained from as-grown ZnCdO films synthesized at different temperatures. A strong peak around 369 nm, characteristic of the NBE emission of pure w-ZnO,[1] is observed for samples T490 and T520, in agreement with the results of XRD and RBS analysis in Figs. 1 and 2. With increasing Cd content (see Fig. 2), the NBE emission peak in Fig. 4 shifts toward longer wavelengths and reaches $\sim$494 nm, suggesting $E_g \sim 2.5$ eV for the material grown at 340 °C. Interestingly, as shown in the inset in Fig. 4, already a minor Cd incorporation (0.4% in T460) causes significant shifts of the NBE position with respect to that in pure w-ZnO. Note that with increasing Cd content, the intensity of the NBE emission evolves non-monotonically, combined with a dramatic broadening of the peak (see samples T340–T400). Moreover, distinct shoulders appear at $\sim$450 and 487 nm in samples T340 and T400 on high- and low-energy sides, respectively.

It should be noted that high-Cd-content samples normally exhibit metastable behavior, changing properties dramatically upon post-fabrication annealing. Indeed, an apparent phase separation between w-ZnO and rs-CdO is detected upon annealing in samples T340–T400 by XRD in agreement with the PL observations, resulting in the NBE emission shifts toward $\sim$384 nm irrespective of the initial amount of Cd (indicated as a dashed line in Fig. 4). In its turn, the films

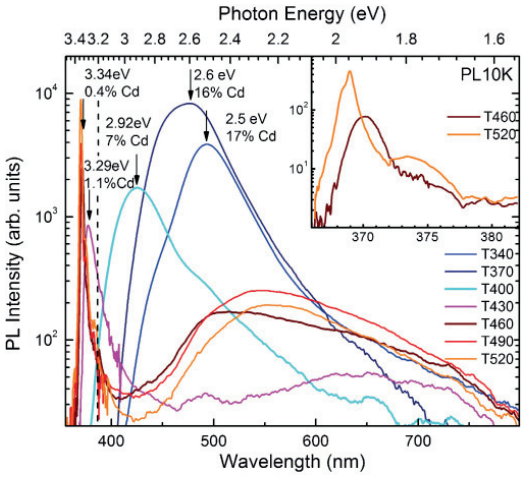

FIG. 4. (Color online) PL spectra taken at 10 K of the ZnCdO films grown at different temperatures. The inset shows the UV-blue part of the spectrum visualizing the manifestation of 0.4% Cd incorporation into ZnO. The dashed line shows a common NBE range where T340–T400 signals shift after annealing. Note that NBE positions in T520–T430 are not affected by post-fabrication anneals.

with low Cd content (e.g., T460 and T430) were found to be stable, i.e., not affected by post-fabrication annealing as confirmed by both XRD and optical measurements, more info in Ref. 24.

To summarize, in spite of the fact that the DMCd flow was maintained constant for the samples in Figs. 1–4, the incorporated amount of Cd is found to vary as a function of the growth temperature, which is also consistent with recent observations by T.Ohashi *et al.*[8] A possible interpretation of the Cd content increasing trend may be done in terms of the precursor decomposition variations as a function of temperature. Indeed, Zn/O lean/rich conditions during MOVPE ZnO synthesis may be readily provided by changing the efficiency of DEZn and *t*-BuOH decomposition solely by tuning the growth temperature.[18] Literally, the pyrolysis of DEZn starts at ∼300 °C and completes at temperatures ⩾385 °C. On the other hand, oxidizing capacity of *t*-BuOH lasts until ∼450 °C. Considering the arguments above, in the context of measurements illustrated in Figs. 1–4, it is likely we have used Zn lean conditions in the low-temperature recipes in our samples. Importantly, DMCd starts to decompose at much lower temperatures, ∼250 °C,[25] meaning that, for example, samples T340 and T370 have been fabricated under Zn-lean conditions, making it possible to incorporate higher Cd content into the films without enhancing DMCd flow rates. The increase in the growth temperature leads to an apparent retardation of Cd incorporation due to the lack of vacant sites, which are instead readily occupied by Zn. Note, however, that increasing of the temperature above 430 °C results in oxygen-lean conditions,[18] and the chemical electronegativity difference between Zn and Cd may limit the incorporation of Cd too. Also, at higher temperatures Cd may desorb from the surface as it is known to be a very volatile element.[26]

B. Exploration of high-content ZnCdO alloys

Optimal synthesis routes—in terms of a combination between Zn-lean conditions and single-line XRD/PL signatures—were determined in Sec. III A, and T370 synthesis was chosen to explore in terms of variation of DMCd flow rates. Figure 5 shows typical XRD 2θ scans taken from the as-grown ZnCdO films fabricated by employing different DMCd flows. The data are labeled in accordance with notations given in Sec. II (note that labels F20 in Fig. 5 and T370 in Fig. 1 represent the same recipe). Similarly to that for T370 in Fig. 1 a single-peak signature is observed for the F20 sample in Fig. 5, indicating within the first approximation a reasonable uniformity in the film. However, new diffraction peaks at $2\theta = 33.3°$ and 38.3° emerge in samples F30–F70 fitting with characteristic rs-CdO (002) and (111) positions, respectively, suggesting a separation between w and rs phases. Interestingly, the position of the wurtzite (002) peak evolves too (compare to a similar evolution in Fig. 1). Specifically, the initial increase in the DMCd flow (e.g., in F30) shifts the reflection (at 34.3° in F20) toward low angles, while the further increase in the flow (samples F40–F70) gradually shifts the peak back to the values characteristic for that in pure w-ZnO (illustrated by a dotted line in Fig. 5). The interpretation for the 2θ changing in the range between w-(002) and zb-(111) positions in Fig. 5 may be similar to that discussed in Sec. III A with respect to possible contributions from corresponding matrixes. Concurrently, the intensity of this peak (follow the dotted line) decreases significantly, along with the FWHM broadening, suggesting that the *c*-axis alignment and crystalline quality in general are strongly reduced with increasing DMCd flow. As a result, the FWHM and the *c*-axis lattice parameter values calculated from the peak positions traced with the dotted line in Fig. 5 evolve in a manner missing a reliable trend. Another prominent shift toward higher 2θ values is also observed for the peak in the range of ∼38.5° in Fig. 5. Again, the magnitude of the shift (see the corresponding dashed line in Fig. 5) is out of range to be explained in terms of a gradual decrease in the lattice parameter in a single phase. However, a combination of Zn incorporation into rs-CdO, Cd incorporation into zb-ZnO, and their intermixing in different magnitudes in different samples may explain this trend in Fig. 5.

The chemical compositions of F-type ZnCdO films were analyzed by RBS and Fig. 6 documents the results of the analysis. The inset in Fig. 6 shows a trend of increasing Cd content as a function of DMCd flow rate. Note that remarkably high Cd content up to ∼60% in F70 was incorporated in our samples, likely assisted by employing Zn-lean conditions. In order to visualize the competition between Cd and Zn atoms, we can replot Cd concentration data as a function of DMCd/DEZn flow ratios as well as to determine the Cd incorporation yield (Y_{Cd}) as a ratio between the actual Cd/Zn content in the film and the DMCd/DEZn ratio in the reactor[9] (see Fig. 7). Note, $Y_{Cd} = 1$ would mean that the stoichiometry of the film is directly proportional to the DMCd/DEZn ratio. For DMCd/DEZn molar ratio ⩾1, Y_{Cd} is only slightly below

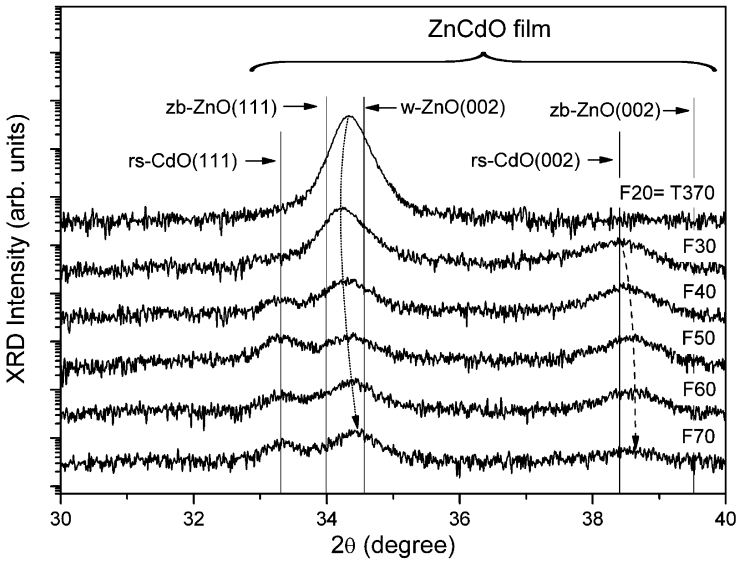

FIG. 5. Evolution of XRD intensities in as-grown ZnCdO films as a function of DMCd flow rate revealing the appearance of different phases. Continuous lines label angles corresponding to the characteristic Bragg reflections from pure w-/zb-ZnO and rs-CdO. Dotted and dashed lines indicate prominent shifts, which are discussed in the text in terms of intermixing of phases characterized by closely positioned peaks.

unity, indeed indicating a better Cd transfer from the gas phase into the films.

Normalized PL spectra taken at 10 K from F-type samples having different Cd contents are depicted in Fig. 8. The spectra are dominated by NBE emission of ZnCdO alloys and exhibit characteristic redshifts consistently with increasing the DMCd flow (meaning increasing Cd content in accordance with Fig. 6). Consistently with XRD (Fig. 5) PL peaks both broaden and decrease in intensity (before normalization—not shown), which implies the deterioration of crystallinity due to the formation of mixed phases. In addition to the dominating NBE emissions, spectral shoulders appear at either lower-energy (samples F30–F50) or higher-energy (samples F60 and F70) sides of the PL peaks in Fig. 8. The spectra were deconvoluted using Gaussian fits and three prominent peaks centered at 487 nm (2.54 eV), 536 nm (2.31 eV), and 590 nm (2.10 eV) were adopted to fit spectra of all F-type samples except for F20, which required an introduction of a higher energy-emission component. Figure 9 shows typical examples of the deconvolution analysis indicating that contributions provided by different components vary with Cd content. Nevertheless, an overall trend in the PL evolution in Fig. 8 is toward domination of the ∼536-nm component in the high-Cd-content ZnCdO. Interestingly, the ∼487-nm emission used as one of the fitting components in Fig. 9 correlates with the maxima of NBE emissions in samples T340 and T370 as well as with the lower energy shoulder in T400 (Fig. 4), altogether not revealing rs-related diffractions in accordance with Fig. 1. Importantly, the post-fabrication annealing affects F-type

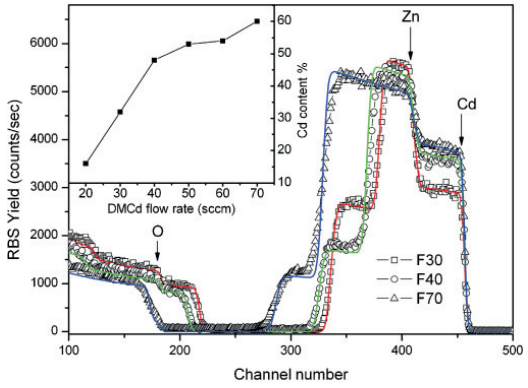

FIG. 6. (Color online) Typical RBS spectra of as-grown ZnCdO synthesized with the DMCd flow rate of 30 (□) , 40 (○), and 70 (Δ) sccm, while lines represent the results of fitting. Corresponding Cd contents are shown in the inset as a function of the DMCd flow rate for all F-type samples.

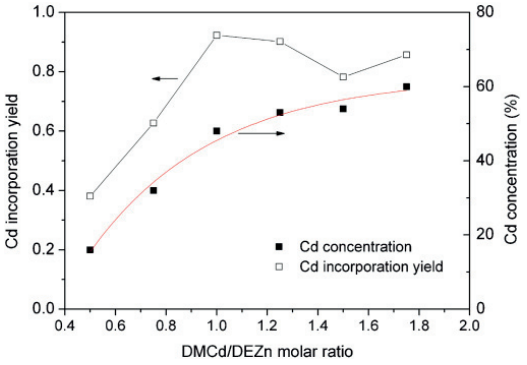

FIG. 7. (Color online) Cd concentration, as determined by RBS and Cd incorporation yield in ZnCdO films as a function of DMCd/DEZn flow ratio in the reactor.

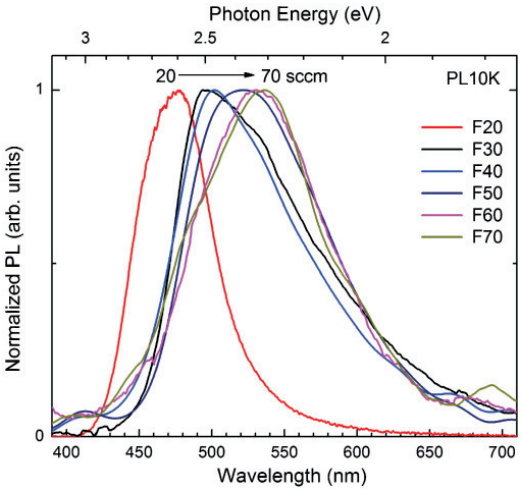

FIG. 8. (Color online) Normalized PL spectra taken at 10 K of samples grown with different DMCd flow rates.

samples in a similar way to that observed in high-Cd-content T-type samples, i.e., after annealing all NBE peaks shift toward ∼384 nm (∼3.21 eV).

C. Calibration of ZnCdO optical signatures with w-ZnO and rs-CdO

Optical properties of pure w-ZnO are relatively well known[1] and, without going into high-resolution measurement beyond our scope, the NBE emission is dominated by excitonic transitions at ∼3.36 eV at low temperature, in agreement with our measurement in samples T520–T490 in Fig. 4. In accordance with literature, rs-CdO exhibits both indirect and direct band gaps at ∼0.84 and ∼2.3 eV, respectively,[27] resulting in a very weak PL due to dominating nonradiative recombination. Nevertheless, Kuo and Huang[28] have observed a PL peak at ∼2.25 eV (550 nm) for CdO nanowires and Xiaochun *et al.*[29] have measured a PL peak at ∼2.33 eV (532 nm) from CdO nanocrystals both to be remarkably close to our 536-nm component in Fig. 9. In order to enhance the comparison, PL from rs-CdO films, manufactured under conditions similar to the rest of the samples, was measured and a typical spectrum is depicted in Fig. 10. In spite of a naturally weak PL signal, we have resolved a dominating peak centered at ∼575 nm in Fig. 10 (2.15 eV[30]), consistent with the literature. Considering Refs. 27–30 along with Fig. 10, we attribute the 536-nm component in Fig. 9 to the NBE signature characteristic of pure rs-CdO. Note that the difference in the peak position (536 nm versus 575 nm) may be explained accounting for Zn contaminating rs-CdO matrix in Fig. 9 as well as elaborated in terms of Burstein-Moss shift due to difference in the strain balance in the films grown on different planes of Al_2O_3.[31] Note that a minor ∼590-nm peak has been observed in both pure rs-CdO[29] and single-phase w-ZnCdO,[2] suggesting this component to involve deeper mid-gap states and/or phonon assisted processes. Importantly, the detection

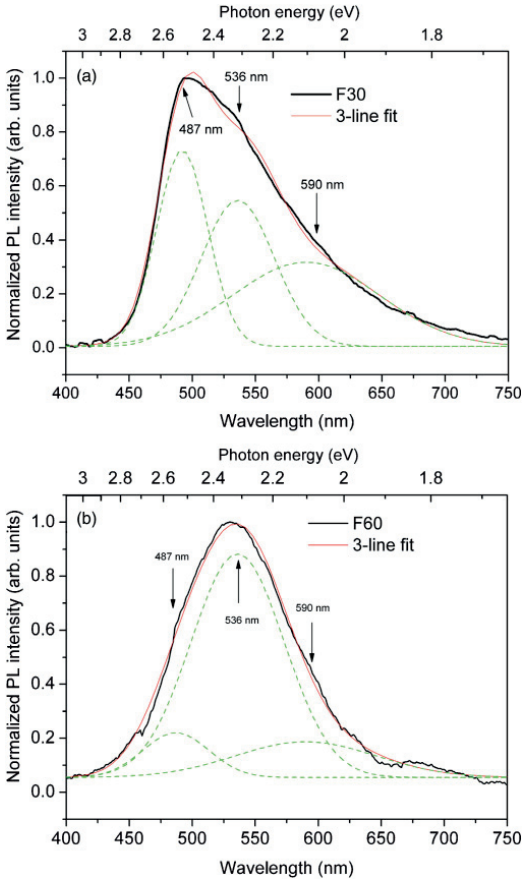

FIG. 9. (Color online) Deconvolution of the normalized PL spectra at 10 K (thick line) for (a) F30 and (b) F60 samples employing a three-line fit. The components used to fit (thin line) the spectra are labeled with arrows.

of the 536-nm component (Figs. 8 and 9) is accompanied with the appearance of rs-CdO-related diffraction signals in Fig. 5 anchoring the calibration. Comparing PL and XRD data implies that the phase separation in the ZnO-CdO system may be a complicated mixture of w and zb and rs phases stabilized at different Zn/Cd contents, which is a matter of a discussion below.

IV. DISCUSSION

A. Reasons and routes for phase separation in ZnCdO

As already mentioned in Sec. I, in spite of a similar elemental chemical character of Zn and Cd, their ternary oxide formation is greatly affected by the appearance of different crystalline structures apparently becoming stable in different compositional ranges. Remarkably, the solid solubility limit of Cd in w-ZnO (S^{Cd}_{ZnO}) is reported to vary between "pessimistic" $\leqslant 5\%$[3] and "optimistic" ∼69%.[7] For

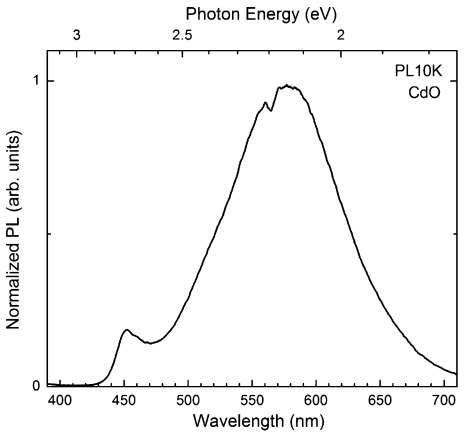

FIG. 10. Normalized PL spectrum of a pure rs-CdO sample grown on *r*-Al2O3 substrate.

example, estimations of low solid solubility of Cd in ZnO may be derived from an early work by Brown and Hummel, who have studied the ZnO-CdO-P_2O_5 system and reported the solubility to be <1% at 800 °C and ∼3% at 1000 °C.[10] Analyzing ZnO-CdO-Fe_2O_3 equilibrium, Bashkirov *et al.* have reported the solubility as high as 12%.[11] More recently, but using similar methodology, Whitaker and Channell studied the ZnO-CdO-B_2O_3 system and found the $S^{Cd}{}_{ZnO}$ value to be negligibly small.[12] The reason for this puzzling variety of solubilities is likely to be that, in spite of Zn/Cd isovalency, ZnO and CdO are not isostructural. Most commonly, Cd when oxidized, adopts octahedral coordination in the cubic B1 rock-salt structure, while ZnO favors tetrahedral coordination in the hexagonal B4 wurtzite structure. Nevertheless, other metastable structures were reported. Specifically, zb-ZnO lies only slightly higher in energy due to its reduced Madelung constant, but the local fourfold coordination is similar to that in the w matrix.[14,32] Interestingly, theoretical calculations by Jaffe *et al.*[33] suggest that a cohesive energy in rs-ZnO (–7.455 eV) is significantly lower than that in w-ZnO (–7.692 eV) while the zb-ZnO has the cohesive energy of –7.679 eV, i.e., very close to that in w-ZnO. Very recently, Zaoui *et al.* have predicted rs-ZnCdO to be more stable than its wurtzite phase for Cd contents >37.5% based on comparison of corresponding cohesive energies[34] (without considering zb structures). Zhu *et al.* have considered all three possible structures—w, zb, and rs—and predicted stabilization of zb-ZnCdO at moderate Cd contents as well as a transition to the rs matrix occurring for Cd content >62%.[13] Though under normal conditions ZnO is thermodynamically stable in terms of its wurtzite phase, zb-ZnO has been fabricated by heteroepitaxy on the zb-like substrates, for example, GaAs.[16] Further, theoretical studies have predicted a difference of ∼80 meV in E_g between w- and zb-ZnO,[35,36] consistent with observations resulting in ∼60-meV difference.[16] Moreover, it has been estimated that the direct band-gap range in zb-ZnCdO is limited to 1.6 eV before the transformation to the rs matrix.[13] Accounting for the similarity in characteristic XRD reflections, the intermixing of w-ZnCdO and zb-ZnCdO may possibly explain the discrepancy in the interpretation of phase equilibria and PL experiments in literature.

At this point, we may conclude that in heteroepitaxial ZnCdO films—metastable by the nature—the actual synthesis may result in different phases stabilized at different growth conditions allowing otherwise nonequilibrium compositions in w, rs, or zb structures to occur (and coexist). For example, considering MOVPE synthesis, the following results are documented in the literature. Ishihara *et al.* has claimed w-ZnCdO single-phase films were synthesized on *a*-Al_2O_3 substrates using remote plasma-enhanced MOVPE with Cd content as high as ∼69%.[7] In a follow-up work from the same group T. Ohashi *et al.* has studied the stability of w-ZnCdO as a function of the growth temperature and detected that critical Cd content for the phase separation decreases from 69% to 50% as the temperature increases from 250 °C to 450 °C.[8] Zúñiga-Pérez *et al.* have reported Cd content of 8.5% in w-ZnCdO fabricated without any phase separation on *r*-Al_2O_3 substrates and claimed 8.5% Cd to be a limit of Cd incorporation into the w-matrix.[9] Gruber *et al.* have reported single-phase w-ZnCdO containing 5% Cd and fabricated on *c*-Al_2O_3 substrates.[3] Interestingly, both Gruber *et al.*[3] and Bertram *et al.*,[6] possibly in the same samples, have observed domains exhibiting lower/high cathode-luminescence (CL) contrasts without deviations in chemical Zn/Cd contents, which may be readily explained by the coexistence of w- and zb-ZnCdO exhibiting a band-gap difference since rs-related reflections likely were not detected. Note that co-existence of the zb and w phases was observed in pure ZnO powder experiments and the phase ratio was found to vary with temperature,[15] which in its turn may explain scattering in $S^{Cd}{}_{ZnO}$ value in literature due to variations in growth conditions. In the next section, we suggest a consistent interpretation of the samples systematically doped with different amounts of Cd as documented in Sec. III.

B. Structural evolution and photoluminescence in the context of responsible mechanisms

Starting with T-type samples, in accordance with Fig. 1 all ZnCdO films are well characterized with reflections within a 34.10°–34.50° 2θ range, and for "zero"-Cd-content samples the peak coincides with that from w-ZnO (002). A gradual increase of Cd incorporation into the w matrix and the corresponding increase in the lattice parameter (see Fig. 3) results in an inevitable accumulation of excess energy (e.g., elastic, electrostatic) that dissipates via segregation in the form of zb-ZnCdO phase[37] minimizing the total energy of the system without macroscopic redistribution of Cd that correlates with a gradual broadening of the diffraction peak (Fig. 3) and dramatic changes in the PL emission in higher-Cd-content samples (Fig. 4). The observed PL peak broadening in T340 and T370 (see Fig. 4) could be due to coexistence of both w- and zb-ZnCdO accounting for, for example, for the zb-/w-band-gap difference of ∼80 meV as detected already in pure ZnO.[35,36] Note, that the PL broadening was observed already in sample T400 containing only 7% Cd, meaning that zb-ZnCdO may form at low Cd contents indistinguishable for XRD (but observed by CL in similar low-content Cd samples[6]). The metastability of T400 is also confirmed by post-fabrication

annealing resulting in the 384-nm NBE shift characteristic for high-Cd-content samples. Further, in accordance with Fig. 5, samples F30–F70 exhibit peaks characteristic for diffraction of w-ZnO and rs-CdO. The appearance of rs-CdO (002) and (111) peaks (not observable in rs-CdO/*c*-Al_2O_3 structures[19]) may happen due to new epitaxial relationships provided by the w-ZnCdO template in our samples. For example, c/a axes of w-ZnCdO and (002)/(111) directions of rs-CdO match much better compared to a corresponding situation in *c*-Al_2O_3.

As mentioned earlier, XRD features of zb-ZnO appear to be similar to rs-CdO, with characteristic (002) and (111) peaks but considering their relative contributions to the diffraction pattern in Fig. 5 we may distinguish a clear trend. First, in sample F20 no indication for the (002) zb peak is observed while the contribution of the (111) zb-related signal to the broadening trend in Fig. 5 is evident. The latter may be because zb-ZnO (111) has a better epitaxial relationship with (002) of w-ZnO.[38] With increasing Cd content the rs-CdO (002) signature emerges (F30), broadens, and shifts (F40–F70) toward higher 2θ values while the rs-CdO (111) peak position appearing in F40 remains constant. The shift (see the dashed line in Fig. 5) may be then explained in terms of the contribution from zb-ZnCdO (002). Indeed, with enhancing Cd content and rs-CdO segregation, it is likely that rs-CdO (002) provides a more favorable epitaxial template for zb-ZnCdO (002), explaining also the fact that the diffraction from (111) zb planes weakens (see the dotted line pointing to the w-ZnO peak position in Fig. 5). Importantly, the structural transformation above is consistent with observing different intensities from characteristic emission components, as determined when deconvoluting PL data. To start with, the 536-nm signature is attributed to rs-CdO and its intensity evolves consistently with that of the XRD pattern. The 487-nm feature was found to be dominant in T340, F30, and F40 exhibiting intermediate Cd contents, accompanied with significant contributions from the metastable zb matrix in accordance with XRD shift trends and is tentatively assigned to an excitonic transition in zb-ZnCdO of a certain stable composition. As mentioned above, contributions from the 487-nm feature are detected in all samples having 7% of Cd (see Figs. 4, 8, and 9), indicating that the same stoichiometric Zn/Cd composition in a zb matrix was reached in all these samples. Further, attributing the shifts in the dominating PL signatures in samples having $\leqslant$7% of Cd to the band gap variations in w-$Zn_{1-x}Cd_xO$, a line given by $3.36–0.0627x$ eV fits the data. Note that post-fabrication anneals of samples having 7% of Cd reveal a characteristic 384-nm (3.23 eV) NBE PL signal and a presence of (002) w-ZnCdO and rs-CdO diffractions only allowing to assign the 384-nm emission to a stable w-ZnCdO phase close to equilibrium having $\sim$2% of Cd employing the linear fit above. The latter estimate suggests a solid solubility limit of Cd in w-ZnO of the order of 2%. The interpretations above are illustrated by a schematic in Fig. 11 revealing three characteristic compositional regions.[39] First, alloying w-ZnO with $\leqslant$2% of Cd results in a single-phase w-ZnCdO. Second, for the range of 7%–17% of Cd, w- and zb-ZnCdO phases coexist. Further, samples having 17%–60% of Cd reveal a mixture of w, zb, and rs phases in different proportions. Finally, there could be a narrow concentration range available for the rs-CdZnO single phase stability at very low Zn contents.[40]

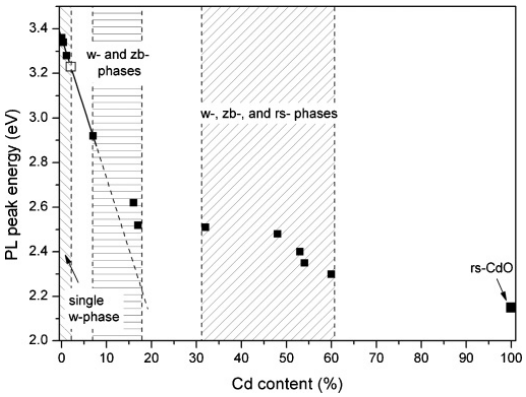

FIG. 11. Dominating NBE PL signatures as a function of Cd content depicted from Figs. 4, 8, and 9 (filled squares) in correlation with corresponding phase stability trends illustrated by dashed lines. The continuous line is a linear fit to the w-ZnCdO-related emissions. An open square represents a characteristic w-ZnCdO signal found after annealing in samples having >7% of Cd.

It should be noted that polytypism, or intermixing of the phases similar to that ascribed in Fig. 11, is also observed in group III–V nanowired zb and w structures, often exhibiting high density of twin planes and stacking faults (SFs).[41] In the bulk form, most of the group III–V materials adopt zb symmetry, while group III nitrides usually exhibit w structure. Nonetheless, there are also reports on GaAs and InP nanowires in the form of w structures,[42,43] as well as on significant w-phase segregation taking place in GaP.[44] Moreover, formation of zb-phase GaN nanowires has been observed, too.[38] Also, the metastable zb-ZnO structures have been stabilized on zb-GaAs(001) substrates by using ZnS buffer layers to minimize the lattice mismatch,[45] whereas w-ZnO has been successfully synthesized on a variety of zb substrates.[46] Several theoretical models address the origin of polytypism in nanowired structures, otherwise exhibiting solely zb or w phases in the bulk, all based on the classic supersaturation concept.[44,47,48] Bearing in mind the arguments above, it is reasonable to anticipate even more prominent and complex polytypism for ternary compounds, such as ZnCdO (see Fig. 11), because of the variety of possible "equilibrium" phases of the two binary constituents before the mixing.

The mechanisms for the structural evolution and PL presented in earlier sections will now be explained in terms of the ionicity of the crystals. Both w-ZnO (zb-) and rs-CdO crystals exhibit electrostatic interaction between the positively charged group II and negatively charged group VI ions. Depending on the Cd content in the ZnO matrix and thus the electronic configuration, different crystal structures become energetically preferable. The stability between sixfold (rs-) and fourfold (w-, zb-) can be predicted considering the ionicity of materials. According to the model proposed by Phillips,[49] the ionicity can be described as $f_i = C^2/(E_h^2 + C^2)$, where

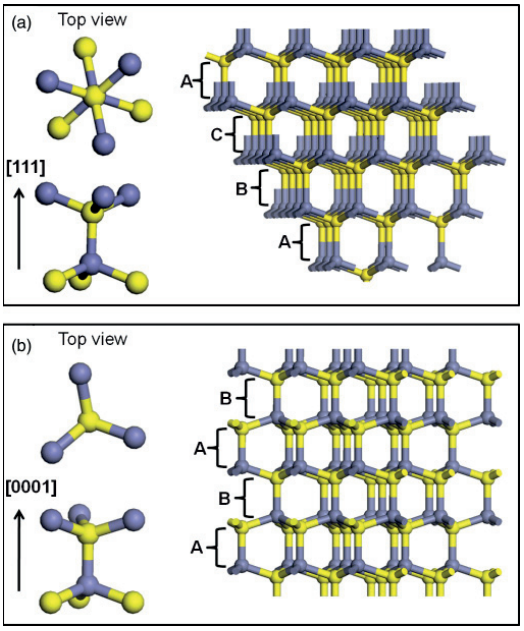

FIG. 12. (Color online) Stacking sequences and zoomed-in views of the bonding configuration in zincblende (a) and wurtzite (b) structures. Different colors denote two sorts of atoms (from group II and VI, respectively).

C and E_h are spectroscopically defined averages of ionic and covalent energy gaps of the pseudopotential in $A^N B^{8-N}$ systems (in our case, $N = 2$ for group II–VI). The competition between closed and open shells, i.e., ionic and covalent bonds, is responsible for the separation of $A^N B^{8-N}$ crystals into sixfold or fourfold coordinated structures. Specifically, group II–VI compounds exhibit a strong ionic behavior with a tendency toward closed-shell configurations, resulting in a sixfold coordinated rs structure. Theory suggests that materials with $f_i < 0.785$ will stabilize in either w or zb structure, while for $f_i \geqslant 0.785$ the rs configuration becomes dominant.[50] These predictions are consistent with the ionicity of 0.616/0.785 and w/rs equilibrium in ZnO/CdO, respectively.[51] In its turn, the instability between w and zb structures can be understood interpreting the increasing interatomic distances and corresponding Coulomb energy with Cd concentration in terms of changes in the stacking fault energy (SFE) and the charge redistribution.[52,53]

In the first approximation, the Madelung constant (α), a parameter describing electrostatic potential of a single ion in a crystal with the ions approximated by point charges, is considered to account for the charge redistribution affecting the w-/zb-phase equilibrium. An ideal w structure with an axial ratio $r = c/a = 1.633$ results in $\alpha_w = 1.6406$,[54] whereas $\alpha_{zb} = 1.6381$ for a zb structure.[55] The changes in axial ratio r will affect the parameter α_w in accordance with $\alpha_w = 1.6406–0.0207\ (r/1.633–1)$[56] (note that for w-ZnO, $r = 1.602$ and $\alpha_{ZnO} = 1.6410$). Assuming that the in-plane lattice parameter a is not affected, the contraction of the lattice in the c direction leads toward higher α_w values, which would stabilize w structure. In contrast, the incorporation of Cd into w-ZnO stretches the lattice in the c direction, hence moving α closer to α_{zb} values. This scenario seems consistent with the evolution of the c parameter shown in Fig. 3 and also with the appearance of the zb-phase signature in Figs. 1 and 4. However, the assumption of constant a may not hold if Cd is incorporated in the w-basal plane. One should also note that atomic units of the zb and w structures exhibit so-called staggered and eclipsed configurations, respectively (see Fig. 12). Indeed, the zb phase exhibits a repeated stacking sequence of three distinct layers of II–VI pairs A-B-C in Fig. 12(a). On the other hand the w-phase is described by a characteristic A-B stacking sequence Fig. 12(b). The energetic difference between these two crystal structures arises from the difference in the third-nearest-neighbor atom spacing, which is shorter for wz than for zb (Fig. 13). The relative energies of these configurations determine the SFE. The change of SFE may be separated into two terms: the bond distortion energy ΔE_b and the Coulomb energy ΔE_c, which correspondingly dominate in low- and high-ionicity crystals. Accounting for a high ionicity (meaning that Coulomb energy dominates), the w structure appears to be more favorable compared to the zb matrix in ZnO because of a shorter distance to the third-nearest(unlike)-neighbor ions in the eclipsed configuration.[56] Similarly to our earlier considerations with regard to α, contraction of the lattice causes ΔE_c to decrease because of the shorter interatomic distances, also meaning the stabilization of the w versus zb structure in ZnO accounting for eclipsed versus staggered stacking. In contrast, a positive strain applied along all crystallographic direction following random Cd incorporation in the Zn-sublattice might result in an increase of ΔE_c enhancing probability of the zb-phase segregation. Takeuchi *et al.*[53] has demonstrated a correlation between the reduced SFE and a process of a charge transfer accompanying the application of strain ε on the bond length, described by $e^* = e_o^*(1+\varepsilon)^s$, where e^* and e_o^* are the effective charges with and without applied strain, respectively, and s is a charge redistribution index ($s = -3.9$ in ZnO).[53] Thus, a positive strain would decrease the e^* values upon introduction of Cd in w-ZnO, thus contributing to decrease of α and stabilizing zb phase.[57] In w structure, the two-third neighbors

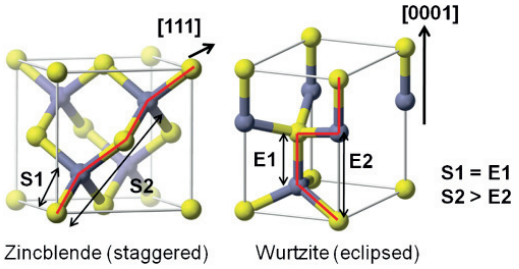

FIG. 13. (Color online) Schematic of (a) staggered and (b) eclipsed configurations, characteristic for zb- and w-structures, respectively, illustrating different distances toward the third-nearest-neighbors (compare S2 and E2).

along the *c* axis are much closer than any other similar pairs of neighbors in the w and zb structures,[56] and hence the charge redistribution accompanying the change of *r* may play a decisive role limiting the phase stability. As a result of the gradual strain accumulation in ZnCdO with 7%–17% Cd, the lattice relaxes locally by a mixture of w and zb phases (see Fig. 11). The exact Cd threshold for w toward zb transition is in the range of 2%–7% and remains to be determined via synthesis of new samples applying similar methodology.

V. CONCLUSIONS

The phenomenon of phase separation in ZnCdO was investigated by a combination of structural/optical measurements and the analysis reveals the presence of a new, not conventionally considered, zb-ZnCdO phase in our samples in addition to commonly discussed w and rs phases. First, low-Cd-content ($\leqslant$17%) ZnCdO was realized preferentially in the w matrix determining optimal Zn-lean conditions on behalf of tuning the precursor decomposition rates during synthesis. However, more detailed analysis of diffraction and PL data revealed that the w single-phase stability range is likely to be as narrow as 0%–2% Cd while samples containing 7%–17% of Cd exhibit a mixture of w and zb phases. Second, high-Cd-content (32%–60%) ZnCdO samples were realized supplying more of Cd precursor utilizing Zn-lean growth conditions, however, resulting in a mixture of w, zb, and rs phases. Characteristic PL signatures at 2.54 and 2.31 eV were attributed to zb-ZnCdO and rs-CdO while the band-gap variation in w-$Zn_{1-x}Cd_xO$ is given by (3.36–0.063*x*) as determined at 10 K. The phase separation is interpreted in terms of corresponding changes in charge distribution and reduced SFE. Interestingly, post-fabrication anneals resulted in stabilization of equilibrium w-ZnCdO phase containing 2% of Cd.

ACKNOWLEDGMENTS

Partial financial support provided by the Research Council of Norway via FRINAT "Understanding ZnO" project and the Nordic Energy Research Agency via N-INNER SolarH2 project are gratefully acknowledged.

[1] U. Ozgur, Y. I. Alivov, C. Liu, A. Teke, M. A. Reshchikov, S. Dogan, V. Avrutin, S.-J. Cho, and H. Morkoc, J. Appl. Phys. **98**, 041301 (2005).
[2] D. W. Ma, Z. Z. Ye, and L. L. Chen, Phys. Status Solidi A **201**, 2929 (2004).
[3] Th. Gruber, C. Kirchner, R. Kling, R. Reuss, A. Wagg, F. Bertram, D. Forster, J. Christen, and M. Schreck, Appl. Phys. Lett. **83**, 3290 (2003).
[4] K. Sakurai, T. Takagi, T. Kubo, D. Kajita, T. Tanabe, H. Takasu, S. Fujita, and S. Fujita, J. Cryst. Growth. **237-239**, 514 (2002).
[5] T. Makino, Y. Segawa, M. Kawasaki, A. Ohtomo, R. Shiroki, K. Tamura, T. Yasuda, and H. Koinuma, Appl. Phys. Lett. **78**, 1237 (2001).
[6] F. Bertram, S. Giemsch, D. Forster, J. Christen, R. Kling, C. Kirchner, and A. Waag, Appl. Phys. Lett. **88**, 061915 (2006).
[7] J. Ishihara, A. Nakamura, S. Shigemori, T. Aoki, and J. Temmyo, Appl. Phys. Lett. **89**, 091914 (2006).
[8] T. Ohashi, K. Yamamoto, A. Nakamura, T. Aoki, and J. Temmyo, Jpn. J. Appl. Phys. **46**, 2516 (2007).
[9] J. Zúñiga-Pérez, V. Muñoz-Sanjosé, M. Lorenz, G. Benndorf, S. Heitsch, D. Spemann, and M. Grundmann, J. Appl. Phys. **99**, 023514 (2006).
[10] J. J. Brown and F. A. Hummel, J. Electron. Soc. **111**, 1052 (1964).
[11] L. A. Bashkirov and N. V. Kornilova, Inorg. Mater. **18**, 1587 (1982).
[12] A. Whitaker and A. D. Channell, J. Mater. Sci. **28**, 2489 (1993).
[13] Y. Z. Zhu, G. D. Chen, H. Ye, A. Walsh, C. Y. Moon, and S-H Wei, Phys. Rev. B **77**, 245209 (2008).
[14] A. Ashrafi and C. Jagadish, J. Appl. Phys. **102**, 071101 (2007).
[15] L. P. Snedeker, A. S. Risbud, O. Masala, J. P. Zhang, and R. Seshadri, Solid State Sci. **7**, 1500 (2005).
[16] A. Ashrafi, Appl. Surf. Sci. **255**, 2342 (2008).
[17] A. J. Clayton, A. A. Khandekar, T. F. Kuech, N. J. Mason, M. F. Robinson, S. Watkins, and Y. Guo, J. Cryst. Growth **298**, 328 (2007).
[18] V. Venkatachalapathy, A. Galeckas, A. Zubiaga, F. Tuomisto, and A. Yu. Kuznetsov, J. Appl. Phys. **108**, 046101 (2010).
[19] J. Zúñiga-Pérez, C. Martínez-Tomás, and V. Muñoz-Sanjosé, Phys. Status Solidi C **2**, 1233 (2005).
[20] J. J. Zhu, T. Aaltonen, V. Venkatachalapathy, A. Galeckas, and A. Yu. Kuznetsov, J. Cryst. Growth **310**, 5020 (2008).
[21] J. Uddin and G. E. Scuseria, Phys. Rev. B **74**, 245115 (2006).
[22] The simulation of RBS spectra was done using SIMNRA code [http://www.rzg.mpg.de/∼mam/].
[23] R. D. Shannon, Acta Cryst. **32**, 751 (1976).
[24] V. Venkatachalapathy, A. Galeckas, R. Sellappan, D. Chakarov, and A. Yu. Kuznetsov, J. Cryst. Growth **315**, 301, (2011).
[25] S. Fujita, S. Matsumoto, and S. Fujita, J. Electron. Mater. **22**, 521 (1993).
[26] V. N. Volodin, V. E. Khrapunov, and R. A. Isakova, Russ. J. Phys. Chem. A **82**, 1075 (2008).
[27] F. P. Koffyberg, Phys. Rev. B **13**, 4470 (1976).
[28] T. J. Kuo and M. H. Huang, J. Phys. Chem. B **110**, 13717 (2006).
[29] W. Xiaochun, W. Rongyao, Z. Bingsuo, W. Li, L. Shaomei, X. Jiren, and H. Wei, J. Mater. Res. **13**, 604 (1998).
[30] Note that the near-band-edge PL emission energy is lower than the actual band-gap energy due to Stokes' shift and the exciton binding energy.
[31] D. Ma, Z. Ye, L. Wang, J. Huang, and B. Zhao, Mater. Lett. **58**, 128 (2003).
[32] C. H. Bates, W. B. White, and R. Roy, Science **137**, 993 (1962).
[33] J. E. Jaffe, J. A. Snyder, Z. Lin, and A. C. Hess, Phys. Rev. B **62**, 1660 (2000).
[34] A. Zaoui, M. Zaoui, S. Kacimi, A. Boukortt, and B. Bouhafs, Mater. Chem. Phys. **120**, 98 (2010).
[35] C. Y. Yeh, S. H. Wei, and A. Zunger, Phys. Rev. B **50**, 2715 (1994).
[36] S. Bloom and I. Ortenburger, Phys. Status Solidi B **58**, 561 (1973).

[37]C. W. Sun, P. Xin, C. Y. Ma, Z. W. Liu, Q. Y. Zhang, Y. Q. Wang, Z. J. Yin, S. Huang, and T. Chen, Appl. Phys. Lett. **89**, 181923 (2006).

[38]B. W. Jacobs, V. M. Ayres, M. A. Crimp, and K. McElroy, Nanotechnology **19**, 405706 (2008).

[39]Note that the windows for appearance of mixed phases in terms of w, zb, and rs structures could vary depending on the deposition techniques/substrates used but, specifically, the Cd solubility limit in w-ZnO should hold irrespective of kinetic routes used in sample manufacturing.

[40]T. C. Zhang, A. Azarov, A. Galeckas, and A. Yu. Kuznetsov (unpublished).

[41]J. Johansson, B. A. Wacaser, K. A. Dick, and W. Seifert, Nanotechnology **17**, S355 (2006).

[42]J. Johansson, L. S. Karlsson, K. A. Dick, J. Bolinsson, B. A. Wacaser, K. Deppert, and L. Samuelson, Cryst. Growth Des. **9**, 766 (2009).

[43]F. Glas, J. C. Harmand, and G. Patriarche, Phys. Rev. Lett. **99**, 146101 (2007).

[44]V. G. Dubrovskii and N. V Sibirev, Phys. Rev. B **77**, 035414 (2008).

[45]A. Ashrafi, A. Ueta, A. Avramescu, H. Kumano, I. Suemuneb, Y-W. Ok, and T-Y. Seong, Appl. Phys. Lett. **76**, 550 (2000).

[46]S. Agouram, J. Z. Perez, and V. Munoz-Sanjose, Appl. Phys. A **88**, 83 (2007).

[47]D. L. Dheeraj, G. Patriarche, H. Zhou, T. B. Hoang, A. F. Moses, S. Grønsberg, A. T. J. Helvoort, B-O. Fimland, and H. Weman, Nano Lett. **8**, 4459 (2008).

[48]M. Moewe, L. C. Chuang, V. G. Dubrovskii, and C. Chang-Hasnain, J. Appl. Phys. **104**, 044313 (2008).

[49]J. C. Phillips, Chem. Phys. Lett. **3**, 286 (1969).

[50]H. Blank, Solid State Commun. **15**, 907 (1974).

[51]C. R. A. Catlow and A. M. Stoneham, J. Phys. C: Solid State Phys. **16**, 4321 (1983).

[52]J. C. Phillips and J. A. Van Vechten, Phys. Rev. Lett. **23**, 1115 (1969).

[53]S. Takeuchi, K. Suzuki, and K. Maeda, Philos. Mag. A **50**, 171 (1984).

[54]F. Keffer and A. M. Portis, J. Chem. Phys. **27**, 675 (1957).

[55]Y. Sakamoto, J. Chem. Phys. **28**, 164 (1958).

[56]P. Lawaetz, Phys. Rev. B **5**, 4039 (1972).

[57]V. S. Urusov, J. Struct. Chem. **9**, 484 (1968).